Trinity College Dublin
Coláiste na Tríonóide, Baile Átha Cliath
The University of Dublin

School of Physics

Exfoliating Two-Dimensional Layered Materials: Solvent Interactions from First-Principles

Urvesh Patil
16341169

June 8, 2021

A thesis submitted in partial fulfilment
of the requirements for the degree of
doctor of philosophy (Physics)

Declaration

I hereby declare that this project is entirely my own work and that it has not been submitted as an exercise for a degree at this or any other university.

I have read and I understand the plagiarism provisions in the General Regulations of the University Calendar for the current year, found at `http://www.tcd.ie/calendar`.

I have also completed the Online Tutorial on avoiding plagiarism 'Ready Steady Write', located at `http://tcd-ie.libguides.com/plagiarism/ready-steady-write`.

Signed: _____ Date: _____

ABSTRACT

Two dimensional materials, such as graphene, MoS_2 and hexagonal boron nitride, show wide ranging electronic and mechanical properties which make applications such as transistors, pressure sensors and protective coatings possible. Solvents are an essential element in the production and processing of these two-dimensional (2D) materials. Liquid phase exfoliation (LPE) is one such solution-processing methods capable of industrial scale production. Here, layers are separated by the application of external force. The solvent molecules then prevent the resulting monolayers from reaggregation, stabilizing the layers in the solvent. It is generally assumed that these solvents do not interact strongly with the layer and so their effects can be neglected. Yet experimental evidence has suggested that explicit atomic-scale interactions between the solvent and layered material may play a crucial role in exfoliation and cause unintended electronic changes in the layer.

Here we use modern computational tools such as density functional theory (DFT), a powerful first-principles method, to study the role of solvent molecules in the process of liquid phase exfoliation. Molecular dynamics simulations are then used to calculate the dynamical properties of the system.

We show using DFT that the interaction between graphene or MoS_2 with individual solvent molecules is van der Waals (vdW) in nature, with negligible charge transferred in between them. We use MD calculations to show that, when graphene is immersed in a solvent, distinct solvation layers are formed irrespective of the type of solvent molecule (i.e., whether polar or non polar) due to these vdW interactions. We show that the formation free energies of these solvation shells is favorable for all the molecules considered. However, energetic considerations such as these cannot explain the experimental solvent-dependence. Instead, kinetic effects can dominate. We find that interfacial solvent molecules with high diffusion coefficients parallel to the

graphene layer result in the lowest experimental concentration of graphene in solution. This can be explained by the enhanced ease of reaggregation in the high diffusion regime. Solvents with smaller diffusion coefficients correspond to higher experimental graphene concentrations. In the low diffusion limit however, this relationship breaks down. We suggest that here the concentration of graphene in solution depends primarily on the separation efficiency of the initial LPE step.

On intercalating group-1 metal ions into the layers, we show that the spontaneous exfoliation and stabilization of separated layers is due to the enhanced solvation energy of charged layers of graphene. When the similar ion intercalation procedure for exfoliation of Group-VI transition metal dichalcogenides (TMDs, MX_2, where M=Mo, W and X = S, Se), they are known to undergo charge induced transitions from semi-conducting H phases to metallic T phases. However, it is difficult to experimentally decouple the effect of composition-dependent phase transition barriers from indirect effects related to the exfoliation process. Here, we study the energetics of transition between the different structural polytypes of four group-VI TMDs upon lithium adsorption. We find that both the activation barrier from the H phase to the metallic phase in charged monolayers and the reverse barrier in neutral monolayers are required to explain experimental results. The solution processing in the presence of the ions can result in co-intercalation, i.e. the intercalation of both the solvent molecule and the ions simultaneously. We develop workflows to determine the most stable configuration when both molecules and potassium ions interact with bilayer graphene. This work flow can be further used to filter molecules which enhance molecule—ion cointercalation in bilayer graphene.

The edges of 2D materials are highly reactive. We show that polar molecules align in a bistable orientation along a graphene edge, and their orientation can be switched using an external field. Experimental data shows that this effect can be used to tune and switch the graphene resistance, and depends on the type of molecule and the graphene termination. Using parameters extracted from DFT, we use an Ising-like model and Monte Carlo simulations to determine how intermolecular van der Waals interactions, dipolar interactions, molecule - graphene interactions and the coupling of the molecular dipole to the external field can be used to explain the experimental results.

ACKNOWLEDGEMENTS

First I would like to express my deep gratitude to my supervisors Prof. Nuala Mai Caffrey and Prof. Stefano Sanvito. I would like to thank Prof. Caffrey for giving me this opportunity and for all her guidance and encouragement specifically in perusing all my un-productive ideas. I would also like to thank her for all her patience in correcting my writing. I would also like to thank my co-supervisor Prof. Stefano Sanvito for giving me this opportunity and introducing me to the field of DFT and high-throughput computation. I could not have asked for better guidance during my graduate studies.

I would also like to thank all the past and present members of the computational spintronics groups. I would like to thank Dr. Thomas Archer for all the conversations about the cluster hardware and for teaching me about efficient running of parallelized codes. I would also like to thank Dr. Rajarshi Tiwari for all the conversations over coffee and helping me to adjust to a different country.

I would also like to thank all the PhD students, postdocs and professors from the second floor of the Lloyd building for all the conversations and entertainment over the years. I would specifically like to thank Nina, Meric, Shardul for the numerous zoom meeting conversations during quarantine.

I would also like to thank science foundation Ireland (SFI) for funding via the Science Foundation Ireland Starting Investigator Research Grant

(15/SIRG/3314). I would also like to thank Trinity Center for High Performance Computing (TCHPC) and at the Irish Center for High-End Computing (project tcphy091b, tcphy084c, tcphy115c and tcphy122c) for the supercomputer facilities without which none of the work presented here would have been possible. I would also like to thank Ujjwala, Somya, Kanika, Ramyani, Sanket, Prashant, Kaustubh, Vikrant and Shefali for creating a mini home away from home that kept me from becoming homesick. We really had some really wild times together. I would specially like to thank Ujjawala Ponduru for all the stimulating conversations and for being a constant dinner partner. I would also like to thank Dr. Priyanka Tiwari for all the awesome food that reminded me of all the home cooked meals, these helped me keep my sanity during the quarantine.

All my numerous friends from my undergraduate, especially my fellow “wingies" Prasanna, Ankit, Sundaram, Dharmendra, Kunal, Krishnakant, Vikas, Aditya and Vinay without whose support and company all this would not have been possible.

Finally, I would like to thank my sister, mother and father for all the support over the years.

PUBLICATIONS

- Patil, Urvesh, and Nuala M. Caffrey. "Adsorption of common solvent molecules on graphene and MoS2 from first-principles." The Journal of Chemical Physics 149.9 (2018): 094702.
- Patil, Urvesh, and Nuala M. Caffrey. "Composition dependence of the charge-driven phase transition in group-VI transition metal dichalcogenides." Physical Review B 100.7 (2019): 075424.
- Patil, Urvesh, and Nuala M. Caffrey. "Structural and orientational ordering of solvent molecules in graphene dispersions." (In preparation)

CONTENTS

CHAPTER

1

INTRODUCTION

1.1 Two-dimensional (2D) layered materials

Two-dimensional materials have attracted considerable interest in the past few years due to their unique geometry, mechanical and electronic properties, and improvements in production techniques that make their industrial use viable. These materials have a thickness of a single atom or a few atoms (typically 2-3). Many of them occur naturally as bulk layered materials, where individual monolayers are bound together via weak van der Waals forces. The most well-known example of such a bulk layered material is graphite. This is made up of atomically thin layers of carbon atoms, known as graphene. A STEM image of a graphene cross section is shown in Fig. 1.1 [1]. In addition to graphite, numerous other materials with two-dimensional or layered geometries have been identified. These materials show a wide variety of structural, electronic and magnetic properties. This makes them prime candidates for various applications.

Although the existence of such stacked materials has been known for a long time, interest in layered materials dramatically increased when individual layers of graphene were shown to be stable after mechanical exfoliation from graphite

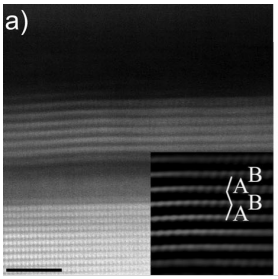

Figure 1.1: STEM of a cross section of graphite. Figure reproduced from [1]. Insert shows the AB stacking of layers in graphite.

[2]. High quality pristine layers of graphene isolated using this method have unique mechanical and electronic properties. This includes the highest tensile strength ever measured of over 130 GPa [3], as well as the lowest measured resistivity at room temperature of approximately $10^{-6}\Omega\text{cm}$ [4]. The isolation of monolayer graphene via the mechanical 'scotch tape' exfoliation method and the initial characterization experiments resulted in the awarding of the 2010 Nobel Prize to Andre Geim and Konstantin Novoselov "for groundbreaking experiments regarding the two-dimensional material graphene" [5].

Shortly thereafter, various other layered materials were identified and subsequently exfoliated. These materials demonstrate a wide variety of electronic and mechanical properties. As a result, these monolayers can be used for a variety of applications including transistors [6], transparent electrodes [7], electromagnetic interference shields [8], sensors [9], batteries [10], catalysts [11], enzyme sensors [12], solar cells [13], supercapacitors [14], battery electrodes [15] and photodetectors [16]. Further applications for these monolayers are continually being found. A recent application is in the field of superconductivity: Superconducting behavior is observed when two layers of graphene are rotated to specific angles (e.g. 1.1° - known as a magic angle) with respect to each other [17]. Furthermore, heterolayers, which are comprised of different layer types stacked on top of each other, can behave very differently to what one might expect based on the individual layers. For example, monolayer graphene/black phosphorus heterostructures demonstrate a large giant magneto-resistance [18] and $SnSe_2$ / WSe_2 heterostructures demonstrate an ultra high current on/off ratio of 10^6 [19].

1.2 Large-scale production of 2D materials

Before these materials can be incorporated into devices, fabrication on a cost-effective, industrial scale must be achievable. Although the scotch tape method is capable of producing high quality layers, it is slow as each individual layer is separated manually. As a result, large scale production is not achievable. Several other methods were developed to produce individual monolayers. These methods can generally be characterized as either 'top-down' or 'bottom-up'. Bottom-up methods comprise those which synthesize the layered material from atomic or molecular precursors, such as chemical vapor deposition (CVD). As this method assembles individual atoms or fragments into extended sheets, it provides an opportunity to produce layers with a predetermined size and shape such as in heterolayers [20] and nanoribbons [21]. Graphene layers as large as 300×30 cm^2 have been grown using CVD techniques [22]. While offering a high degree of atomic control, bottom-up methods require careful optimization for each material considered, can contain wrinkles and are not scalable [22, 23, 24].

Top-down methods involve the extraction of individual layers from a parent layered crystal. An example of this is the isolation of a graphene monolayer from graphite by micro-mechanical cleavage (the scotch tape method) [5]. This method relies on the fact that the intra–layer interaction energies between the constituent atoms is much larger than the inter–layer van der Waals interactions holding the layers together. While cleavage techniques have been optimized to yield high quality 2D layers, they have a relatively low yield [5]. Other methods of separation, including laser ablation [25] and spatial charge variation due to laser pulses [26], have also been demonstrated. These methods suffer from the same scaling problems as the micro-mechanical method because only one layer is produced at a time.

In contrast, the liquid-phase exfoliation (LPE) of layered materials is a scalable top-down method, capable of producing industrial quantities of layers at a low cost [27, 28]. Using this method, sheets with lateral sizes as large as 5 μm have been produced [29, 30, 31, 32]. Large shear forces, introduced in the presence of a solvent through either sonication, high-shear mixing or wet-ball milling, are used to overcome the van der Waals interactions binding the layers together [33]. The solvent then stabilizes the resulting nanosheets, preventing their aggregation or precipitation. The solvent plays a critical role, with the monolayer yield showing a strong dependence on the type of solvent used. For example, N-Methyl-2-pyrrolidone (NMP) is one of the best solvents for the exfoliation of graphite with

yields as high as 19 wt.% [34], whereas hexane is one of the worst solvents for graphite exfoliation with negligible yields. The optimal solvent also depends on the type of layers to be exfoliated. For example, cyclohexanone is the best solvent for the exfoliation of graphite, cyclohexyl-pyrrolidinone (CHP) is the best solvent for the exfoliation of hexagonal boron nitride and DMSO is the best solvent for the exfoliation of WS_2 [28, 32]. Determining the optimal solvent is the focus of much research.

The exfoliation process can be accelerated, and the yield enhanced, by introducing excess charge on the layers. This can be achieved by the addition of ions such as lithium or potassium to the solvent. The charge transferred from the ions to the layers accelerates the process of layer separation and enhances the stability of the layers suspended in the solution [35, 36, 37]. However, the addition of excess charges also has unintended consequences. For example, in the case of group-VI transition metal dichalcogenides (TMD) these excess charges can induce structural phase transitions from a semi-conducting H-phase to a metallic T-phase [11, 38, 39, 40, 41, 42]. These changes may not be desirable and maintaining control over the process is difficult.

1.3 Predicting an optimal solvent for LPE

Predicting the optimal solvent to maximize the yield of the exfoliation process is an active area of research. These attempts mostly rely on determining the optimal solvent–layer interactions that will result in the maximum yield. This interaction can be modeled quantitatively via quantities such as the surface tension/energy of the solvent or the Hildebrand and Hansen solubility parameters. These blunt methods, which model the solvent molecules as collective entities, have limited success and hint at the need to understand the exfoliation process in detail at the microscopic or atomic-level. Moreover, these methods assume that the process of exfoliation is thermodynamically driven, and kinetic effects such as sedimentation play a minor role.

Liquid phase exfoliation is a two step process. External forces are first used to separate the layers. The exfoliated layers are then stabilized in the solvent. Experimentally, developing an atomic level understanding of the process is difficult as both steps occur simultaneously in the solvent. The exact effect of the solvent on the both the exfoliation and stabilization steps is not well understood. Solvent exchange methods, where different solvents are used in the

exfoliation and stabilization steps, find that solvents which do not perform well in exfoliating monolayers from the bulk material may perform very well in maintaining a stable dispersion of already exfoliated monolayers. This clearly demonstrates the fact that the solvent plays a different role in the two steps [43, 44, 45].

Several open questions remain: The exact nature of the interface between the solute and the solvent is unknown. Likewise, it is not known if the interactions at the interface depend on bulk properties of the solvent such as its dipole moment. While it is generally assumed that energetic considerations, such as the solvation energy, dominate in stabilizing the exfoliated material, there is some indication that kinetic effects may also play a role. However, the kinetic behavior of the solvent at the interface is not well understood.

1.4 Computational modelling of optimal LPE solvents

It is here that computational modeling and simulations are advantageous, as they allow us to isolate and study the individual components of the system systematically. Another advantage is that the simulated systems need not be physically or experimentally realizable. For example, to determine the interaction between the solvent and solute, we can simulate an isolated molecule on a large sheet without defects and determine the nature of interaction between the two. This system is not easily experimentally realizable due to the difficulty in isolating an individual molecule and placing it precisely on a defect-free monolayer.

Once the nature of the interaction is well understood, it becomes possible to screen for optimal solvents to exfoliate a particular layered material. Traditionally, the discovery of new materials and their production relied on trial-and-error experimental work. Due to the development of accurate quantum mechanical calculation methods, computational screening has become possible. These methods have several advantages over the traditional experimental method as they can be automated and require minimal human input. These screening methods are trivially parallel and are only limited by the amount of computational resources available.

Identification of exfoliable materials is one such example where computational

screening was successfully used. Previously, suitable materials for exfoliation were identified from crystallographic data. Acquiring this data can be expensive and time consuming. To accelerate the discovery of promising layered materials for exfoliation, Mounet et al. developed a method using predetermined van der Waals radii and inter-atomic distances to automatically identify materials that can be exfoliated into layers [46]. This method relies on accurate quantum mechanical calculations using Density Functional Theory (DFT) to determine the geometry and other structural properties. Haastrup et al. extended this, by attempting to determine all stable two dimensional materials irrespective of the existence of their bulk counter-parts. These stable structures can then be synthesized chemically using 'bottom-up' methods such as CVD [47].

Finding optimal solvents for liquid phase exfoliation is a prime candidate for computational screening. The inability to identify an optimal solvent for the exfoliation of a particular material is the main limitation for the extensive use of this process. Currently, the experimental procedure to identify suitable solvents is slow and costly, requiring a large amount of human intervention. It typically requires that data is acquired for tens of different solvents and the best-performing solvents identified. Solvents with similar bulk properties, such as surface tension, are then tested. This procedure is then repeated until the optimal solvent for that particular layered material is found. Of course, there is no guarantee that the best solvent will be found in this way.

A major advantage of computational screening in this context is that the suitability of toxic solvents can be ascertained without having to test them in a laboratory. NMP and cyclopentanone are common solvents for the exfoliation of graphite and molybdenite, but are toxic for humans. Finding replacements for these solvents will be necessary before LPE can become an industrially viable production method of individual monolayers. Additionally, this method can be used to accelerate the search for solvents with particular properties such as those with low boiling points. Currently, many of the solvents used in the exfoliation of graphite have very high boiling points. For example, cyclopentanone has a boiling point of 131°C, NMP has a boiling point of 202°C and DMF has a boiling point of 153°C. As a result, it can be very difficult to remove the solvent from the exfoliated materials. This limits their use in several applications where pristine monolayers are required. The aim of computational screening methods is not to completely replace experiments, but to replace the trial-and-error experimental search.

1.5 Importance of exposed layer edges

Realistic 2D materials contain exposed edges. These are highly reactive and can play an important role in the exfoliation process. They can act as "wedging" sites, where the solvent can pry the layers apart, facilitating their separation [48, 49]. Their high reactivity can also play an important role in some applications and must be considered when designing, for example, gas sensors.

Typically, the edges are largely ignored in simulations. The layer is generally modeled as a infinite periodic structure or as having passivated edges so that the edge plays a minimal role in the simulation. In reality these idealized structures are impossible to realize and the effect of the edge cannot be neglected.

Caridad. et al. demonstrated that the interaction between small polar molecules and the edges of a graphene sheet has a measurable and switchable effect on the graphene resistance [50]. When molecules adsorb on its edge sites, graphene shows a bistable resistance behavior (hysteresis) that depends on the type of molecule and the type of edge passivation. This originates in the induced charge density on graphene due to the aligned dipole moment of the molecules. An external field, applied with a gate, can be used to switch the resistive behaviour. In order to optimize the performance of this device, a through understanding of the effect of the graphene edge on the molecule behavior and vice versa is necessary.

1.6 Thesis Organization

This thesis systematically investigates the nature of the interface between layered materials and solvents, and determines how these atomic-scale interactions play a role in the liquid phase exfoliation and subsequent stabilization of layered materials. To do this, we primarily use density functional theory and classical molecular dynamics.

Chapter 2 contains the underlying theory and simulation techniques used in this Thesis. We give a brief overview of the Hohenberg-Kohn theorems and the Kohn-Sham scheme. We discuss the practical implementation of the Kohn-Sham scheme in each of the VASP, QuantumEspresso and CP2K codes. We present the continuum solvent model, which is a hybrid model developed to simulate liquid solvents. The molecular dynamics technique is introduced together with the concepts of force fields, ensemble averages and thermostats. Finally, we discuss methods to calculate the free energies of interaction using alchemical analysis techniques, and to calculate diffusion coefficients using the Smoluchowski equation.

In Chapter 3, we study the liquid phase exfoliation of pristine graphite and MoS_2 in detail. We start by determining the nature of the interaction between individual solvent molecules and monolayers of graphene and MoS_2. We do this by calculating the potential energy surface (PES) of these molecules on the surface using high throughput density functional theory calculations. We then extend this investigation to consider how the bulk liquid solvent behaves in the vicinity of a graphene monolayer. We calculate the thermodynamic and the kinetic properties of the molecules using classical molecular dynamics. As we are particularly interested in the behavior of the solvent directly at the interface, we present the solvation structure, free energies of interaction and the diffusion of molecules on the surface of graphene.

In Chapter 4, we discuss the ion-assisted exfoliation of layers. We use the continuum solvation model to determine how the interlayer binding energies of intercalated graphite depends on the presence of a solvent. We show that the spontaneous disintegration of ion-intercalated layers is due to the enhancement of the solvation energy as a result of the residual charge from the ions. We then show that such an excess charge can induce a phase transition in group-VI transition metal dichalcogenides, and discuss how this depends on the chemical composition of the monolayer. Finally, we develop a method to determine the

relative orientation of two layers of graphene, a solvent molecule and a potassium ion. This method can be used to explore co-intercalation effects which can occur in the salt-assisted exfoliation of graphite.

In Chapter 5, we consider explicitly how small molecules such as H_2O and NO_2 interact with the edge of a graphene sheet. We are particularly interested in understanding the origin of a large and ambipolar charge bistability in graphene found experimentally. First, we determine the ground state structure of these molecules adsorbed on the graphene edge. We find that the ferroelectric-like behavior of the molecules can be simulated using an Ising-model for molecular dipoles, modified to account for hydrogen bonding and an interaction with an external field. We show how the required parameters for this model can be extracted from density functional theory calculations. From the Ising-model and Monte-Carlo simulations we determine the relative importance of these interaction terms to the experimental observation of hysteresis.

Finally, we conclude the thesis with a short summary of the work presented here and discuss some outstanding problems that would benefit from further investigation.

CHAPTER

2

COMPUTATIONAL METHODS

The electronic properties of an arrangement of M atoms each at positions $R_1, R_2, ..., R_{M-1}, R_M$ and N electrons with coordinates $r_1, r_2, ..., r_{N-1}, r_N$ is described by the Schrödinger equation [51] and is given as,

$$\widehat{H}\ \psi(r_1, ..., r_N, R_1, ..., R_M) = E\psi(r_1, ..., r_N, R_1, ..., R_M) \tag{1}$$

where $\widehat{H}$ is the Hamiltonian of the system, E is the energy and $\psi(r_1, ..., r_N, R_1, ..., R_N)$ is the wavefunction [52, 53]. Eq. 1 is an eigen problem where E and ψ are the eigen values and eigen vector of the Hamiltonian $\widehat{H}$ respectively. The Hamiltonian $\widehat{H}$ is the sum of the kinetic energy operator and the Coulomb interaction potential of all the electrons and nuclei. It is given as,

$$\widehat{H} = \hat{T}_e + \hat{T}_{nuc} + \hat{V}_{e-e} + \hat{V}_{nuc-nuc} + \hat{V}_{e-nuc} \tag{2}$$

where, in atomic units, $\hat{T}_e = -\frac{1}{2}\sum_i \nabla_i^2$ is the electron kinetic energy, $\hat{T}_{nuc} = -\sum_J \frac{1}{2M_J}\nabla_J^2$ is the nuclear kinetic energy, $\hat{V}_{e-e} = \frac{1}{2}\sum_{i,j;i\neq j}^{N} \frac{1}{|r_i - r_j|}$ is the electron-electron Coulomb interaction, $\hat{V}_{nuc-nuc} = \frac{1}{2}\sum_{I,J}^{M} \frac{Z_J Z_I}{|R_I - R_J|}$ is the

nuclear-nuclear Coulomb interaction and $\hat{V}_{e-nuc} = -\sum_{i,J}^{N,M} \frac{Z_J}{|r_i - R_J|}$ is the electron-nuclear Coulomb interaction.

The complete Schrödinger equation described in Eq. 1 with Hamiltonian described in Eq. 2 has 6M + 3N independent variables, where the factor of 6 (=3 × 2) takes into account 3 spatial and 2 spin degrees of freedom for the electrons. This equation can only be solved analytically for a one electron system [51] - for any realistic system the number of variables is very large, making a numerical solution intractable.

2.1 Born-Oppenheimer approximation

To make the numerical solution tractable a reduction in the number of variables (degrees of freedom) is desirable. The first approximation that can be made is the Born-Oppenheimer approximation [54]. In this, the mass ratio between nucleus and electrons, which is of the order of 10^5, is exploited to decouple the nuclear and electronic degrees of freedom.

The complete wavefunction ψ is written as a product of the nuclear and electronic wavefunction, [55]:

$$\psi(r_N; R_M) = \phi_{[R_M]}(r_N) u(R_M) \tag{3}$$

where $u(R_M)$ is the nuclear wavefunction and $\phi_{[R_M]}(r_N)$ is a function of electronic coordinates with the nuclear coordinates as a parameters. The electronic part of the wavefunction is the solution of the system where the lattice is static with the nuclei fixed at positions $\{R_J\}$. The Schrödinger equation for the static lattice system is given as,

$$\left[\hat{T}_e + \hat{V}_{ee} + \hat{V}_{e-nuc}\right] \phi_{[R_M]}(r_N) = E_e \phi_{[R_M]}(r_N) \tag{4}$$

Substituting approximations Eq. 3 and Eq. 4 in Eq. 1:

$$\begin{aligned}
\widehat{H}\psi &= \left[\hat{T}_e + \hat{T}_{nuc} + \hat{V}_{e-e} + \hat{V}_{nuc-nuc} + \hat{V}_{e-nuc}\right] \phi_{[R_M]}(r_N) u(R_M) \\
&= \left[\hat{T}_{nuc} + E_e + \hat{V}_{nuc-nuc}\right] \phi_{[R_M]}(r_N) u(R_M) \\
&= \phi_{[R_M]}(r_N) \left[\hat{T}_{nuc} + E_e + \hat{V}_{nuc-nuc}\right] u(R_M) \\
&- \sum_J \frac{1}{M_J} \left[2\nabla_J \phi_{[R_M]}(r_N) \nabla_J u(R_M) + u(R_M) \nabla_J^2 \phi_{[R_M]}(r_N)\right]
\end{aligned} \tag{5}$$

The final summed last therm is a result of the dependence of $\phi_{[R_M]}(r_N)$ on the nuclear coordinates $\{R_J\}$. The first order energy contribution of this term is:

$$\delta E = \int dr\ dR\ \phi^*_{[R_M]}(r_N)u^*(R_M)\sum_J \frac{\hbar^2}{2M_J}\left[2\nabla_J\phi_{[R_M]}(r_N)\nabla_J u(R_M)u(R_M)\nabla^2_J\phi_{[R_M]}(r_N)\right] \tag{6}$$

The first term in Eq. 6 vanishes for frozen nuclei as the integral results in terms of form:

$$\begin{aligned}\int dr\phi^*_{[R_M]}(r_N)\nabla_J\phi_{[R_M]}(r_N) &= \frac{1}{2}\nabla_J\int dr\left|\phi_{[R_M]}(r_N)\right|^2 \\ &= \frac{1}{2}\nabla_J n_e \\ &= 0\end{aligned} \tag{7}$$

In cases when the electrons are tightly bound to the nucleus, the second term in Eq. 6 contributes approximately $\frac{1}{M_J}E_{ke} \approx 10^{-5}E_{ke}$, where E_{ke} is the kinetic energy of electrons. This contribution is small and can be neglected.

Finally, we can neglect the first order term in Eq. 6 and decouple the nuclear degrees of freedom from the electronic degrees of freedom. If this term is neglected then the total energy can be obtained by solving the equation:

$$\left[\hat{T}_{nuc} + E_e + \hat{V}_{nuc-nuc}\right]u(R_M) = Eu(R_M). \tag{8}$$

The set of equations given in Eq. 4, Eq. 8 and Eq. 3 together completely define the wave function in the Born-Oppenheimer approximation.

2.2 Hohenberg – Kohn theorems

With the Born-Oppenheimer approximation the number of degrees for the electronic problem is reduced to 6N. The reduced degrees of freedom are still not numerically tractable and further approximations are necessary. One such approximation is to remap the wavefunction problem into a electron density problem. The electron density is defined as,

$$\begin{aligned}n(r) &= \int \phi^*(r_1, r_2, ..., r_{N-1}, r_N)\phi(r_1, r_2, ..., r_{N-1}, r_N)\ dr_2\ ...\ dr_{N-1}\ dr_N \\ &= \int \left|\phi(r_1, r_2, ..., r_{N-1}, r_N)\right|^2\ dr_2\ ...\ dr_{N-1}\ dr_N\end{aligned} \tag{9}$$

and indicates the probability that an electron is present at position r. Irrespective of the system size, only 3 independent spatial coordinate variables are required to describe the electron density. For this re-mapping of the problem we must first show that the Hamiltonian is a functional of electron density.

Clearly the wavefunction is a functional of the electron density and hence by extension all the quantities that depend only on the electron wavefunctions, namely the kinetic and electron-electron interaction energy terms in Eq. 4, are a functional of the density. This functional is defined as:

$$F\left[n(r)\right] = \left\langle \phi \left| \hat{T}_e + \hat{V}_{e-e} \right| \phi \right\rangle \tag{10}$$

The functional $F\left[n(r)\right]$ is universal irrespective of the remaining electron-nuclear term. The functional form of $F\left[n(r)\right]$ is unknown and is a major hurdle to the exact solution of Eq. 4.

The electron-nuclear interaction energy term depends on the nuclear positions and the uniqueness of this potential was established formally by Hohenberg and Kohn [56]. They showed that the external potential V_{en} is a unique functional of the ground state density, i.e., every electron density corresponds to a unique external potential. This can be shown by contradiction. Suppose a ground state electron density $n(r)$ corresponds to the wavefunction ϕ, energy E and external potential V_{en}. If the external potential is not unique then there exists a corresponding external potential $V_{en}^{'}$ and wavefunction $\phi^{'}$ which results in same ground state density $n(r)$. Clearly, $\phi^{'} \neq \phi$ if $V_{en} - V_{en}^{'} \neq constant$. The corresponding ground state energy is

$$\begin{aligned}
E^{'} &= \left\langle \phi^{'*} \left| \left[T_e + V_{en}^{'} + V_{ee} \right] \right| \phi^{'} \right\rangle \\
&= \left\langle \phi^{'*} \left| \left[T_e + V_{en} + V_{ee} + V_{en}^{'} - V_{en} \right] \right| \phi^{'} \right\rangle \\
&< \left\langle \phi^{*} \left| \left[T_e + V_{en} + V_{ee} + V_{en}^{'} - V_{en} \right] \right| \phi \right\rangle \\
&= \left\langle \phi^{*} \left| \left[T_e + V_{en} + V_{ee} \right] \right| \phi \right\rangle + \left\langle \phi^{*} \left| \left[V_{en}^{'} - V_{en} \right] \right| \phi \right\rangle \\
&= E + \left\langle \phi^{*} \left| \left[V_{en}^{'} - V_{en} \right] \right| \phi \right\rangle \\
&= E + \int d^3r \; n(r) \left[V_{en}^{'} - V_{en} \right]
\end{aligned} \tag{11}$$

Following the same arguments starting from non-primed quantities we can show

that,

$$E = E^{'} + \int d^3r \; n(r) \left[V_{en} - V_{en}^{'} \right] \tag{12}$$

Taking a sum of Eq. 11 and Eq. 12 gives,

$$E^{'} + E < E + E^{'} \tag{13}$$

which is a contradiction. Hence we can conclude that the external potential (V_{en}) is a unique functional of the electron density $(n(r))$.

Hohenberg and Kohn also show that, for an external potential (V_{en}) and its corresponding density $n(r)$, the energy functional

$$E_{V_{en}}[n(r)] = F[n(r)] + \int V_{en} n(r) \; d^3r \tag{14}$$

has a minima at the ground state density when the ground state is non-degenerate. The minimization is over all densities where the total number of electrons are conserved. i.e. $\int n(r) \; d^3r = N$. The non-degeneracy condition can be removed by using Levy's constraint search formalism [57]. This constraint minimization is equivalent to solving an Euler-Lagrange equation

$$\frac{\delta F[n]}{\delta n(r)} + V_{en}(r) = \mu \tag{15}$$

where μ is the chemical potential, which is the Lagrange multiplier introduced to satisfy the electron conservation and is given as $\frac{\delta E}{\delta N}$.

2.3 Kohn – Sham scheme

The Hohenberg and Kohn theorems show the existence of the universal functional and show that the remapped density problem can be solved using a variational minimization procedure over the density due to the presence of the energy minimum at the correct density [56]. The exact form of the functional is unknown and is an active area of research. The current widely used formalism of density functional theory is based on a scheme proposed by Kohn and Sham [58]. They re-mapped the interacting many electron problem into an effective non-interacting problem. This remapped system has an electron density and energy identical to the original system.

In the Kohn-Sham (KS) scheme the non interacting single electron wavefunction

satisfies:

$$\left[-\frac{\hbar^2}{2m_e}\nabla^2 + v^s_{eff}\right]\phi^s_i = \epsilon_i \phi^s_i \tag{16}$$

where ϵ_i is the i^{th} eigenvalue corresponding to the single electron wavefunction ϕ^s_i and v^s_{eff} is the effective potential. For a N-electron system the equivalent many-body electron density is recovered as

$$n(r) = \sum_{i=1}^{N} \int d^3r \; f_i \; |\phi^s_i|^2 \tag{17}$$

where f_i is the i^{th} orbital occupation function.

Note the absence of an electron-electron interaction potential in Eq. 16. This is because the system is non-interacting by definition. The electron-electron interaction term from Eq. 4 is absorbed in the effective potential (v^s_{eff}). In the Kohn-Sham scheme the non-interacting kinetic energy is defined as

$$T_s[n] = \left\{\Phi[n]\middle|\hat{T}\middle|\Phi[n]\right\} \tag{18}$$

where $\Phi[n]$ denotes the minimization over the Kohn-Sham wavefunctions such that Eq. 17 is satisfied and is different than the actual many-body kinetic energy. The universal functional in Eq. 10 is reformulated as

$$F[n] = T_s[n] + U[n] + E_{xc}[n] \tag{19}$$

where, $U[n] = \int d^3r \; \frac{n(r)n(r')}{|r-r'|}$ is the Hartree energy and the rest of the "unknown" parts of the functional are contained in the exchange-correlation energy $E_{xc}[n]$. The corresponding exchange-correlation potential is defined as $V_{xc}(r) = \frac{\delta E_{xc}}{\delta n(r)}$. Comparing Eq. 16, Eq. 4 and Eq. 19, the effective potential v^s_{eff} is given as,

$$v^s_{eff}[n] = V_{en}(r) + \int d^3r \; \frac{n(r)}{|r-r'|} + V_{xc}[n](r) \tag{20}$$

The exchange-correlation energies are further broken into separate exchange and correlation energies. The exact exchange energy is the difference between the many-body electron-electron interaction energy and the Hartree energy,

$$E_x[n] = \left\langle \Phi[n] \middle| \hat{V}_{ee} \middle| \Phi[n] \right\rangle - U[n] \tag{21}$$

where, the first term is similar to $T_s[n]$ and is minimized over the Kohn-Sham

wavefunctions such that Eq. 17 is satisfied and is not the same as the actual many-body electron-electron interaction energy. The exact correlation energy given as,

$$\begin{aligned} E_c[n] &= F[n] - T_s[n] - U[n] - E_x[n] \\ &= (T[n] - T_s[n]) + (V_{ee}[n] - U[n] - E_x[n]) \end{aligned} \tag{22}$$

The Kohn-Sham scheme described in Eq. 16 along with Eq. 20, Eq. 22 and Eq. 21 is exact and contain no approximations. The calculation of the exact exchange energy and the exact correlation energy using the equations Eq. 22 and Eq. 21 is not possible as the actual form of these terms as a functional of the electron density is unknown. In practice, approximate functionals based upon the electron density must be introduced to describe these terms.

2.4 Practical implementation of Density Functional Theory

2.4.1 Self Consistent Field

In the Kohn-Sham scheme described in Eq. 16, the effective Hamiltonian (Eq. 20) is dependent on the electronic density via the effective potential and is solved self consistently. A flow chart of the self-consistent scheme is shown in Fig. 2.1.

Another simplification is the use of pseudopotentials to represent the core electrons and reduce the number of electrons in the system. The pseudopotentials can be viewed as the combined effective potential of the nucleus and the core electrons experienced by the valence electrons. With this simplification the total many-body Hamiltonian in Eq. 2 can be written as

$$\widehat{H} = \hat{T}_e + \hat{T}_{core} + \hat{V}_{e-e} + \hat{V}_{core-core} + \hat{V}_{e-core} \tag{23}$$

where the nucleus is replaced by the effective core and the corresponding Kohn-Sham Hamiltonian is also modified. This modification is dependent on the basis set used and is discussed in Section 2.4.2.

2.4.2 Basis functions

For numerical simplification and ease of numerical implementation on computers, the single particle wavefunctions (ψ_i) are represented as a linear combination of

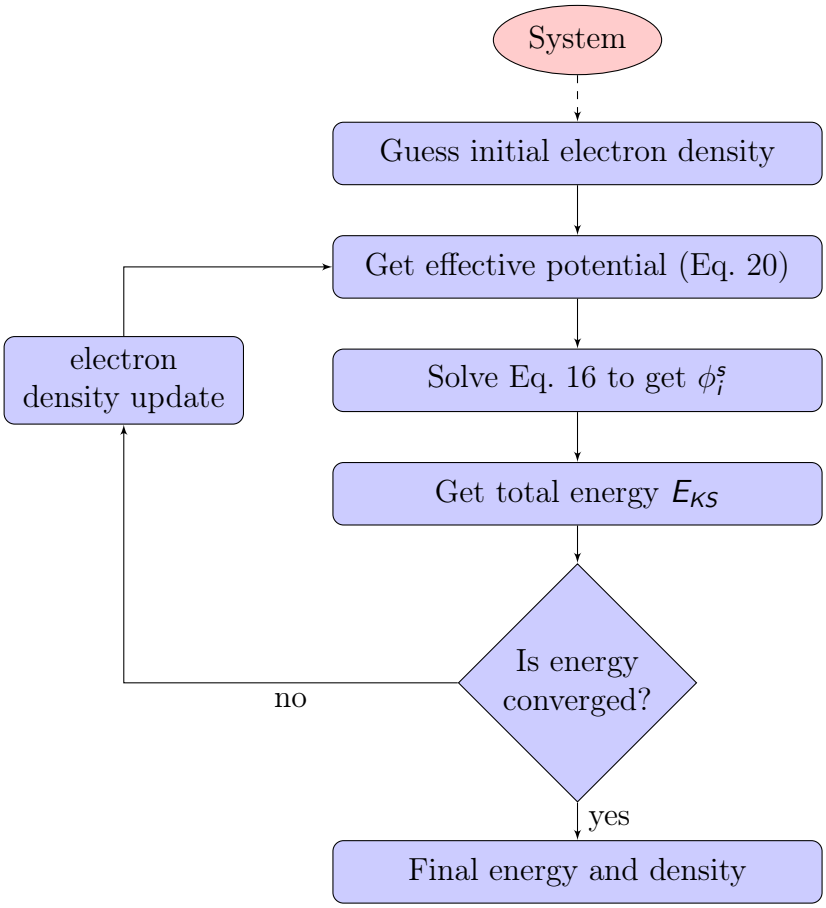

Figure 2.1: Flowchart describing the self consistent Kohn-Sham scheme.

basis functions.

$$\psi_i(r) = \sum c_j^i b_j(r) \tag{24}$$

where c_j^i are the expansion coefficients, b_j are the basis functions and the sum is over all basis functions in the basis set. Some of the popular basis functions used are plane waves (PW), projected augmented waves (PAW) [59], gaussian functions (GTO) [60], mixed gaussian–plane waves (GPW) [61] and numeric atomic orbitals (NAO) [62]. The accuracy of the calculated density and energy is dependent on the number of basis functions in the basis set and not on the type of basis function used for the expansion. Some basis functions can have some advantages for the system under consideration. For example, for non-periodic systems, finite basis sets such as gaussian functions (GTO) or numeric atomic orbitals (NAO), reduce the number of basis functions required compared to plane wave basis functions. This reduces the amount of computer memory required.

If PWs are used, the wave-function can be expanded as a Fourier expansion over

a set of plane-waves:

$$\psi_i(r) = \sum_{k}^{N} c_k^i e^{\iota k.r} \tag{25}$$

where k represents the wave number of the plane wave and N represents the number of plane waves. The number of basis functions (wave numbers k) required can be infinite, so a cutoff is defined in terms of the largest wave number k_{max} or kinetic energy E_{cut} of the plane wave used to represent the wavefunction. This wave number and the kinetic energy are related by $E_{cut} = \frac{\hbar^2}{2m_e} |k_{max}|^2$.

The advantage of plane waves is the $\mathcal{O}\{N \log(N)\}$ time required for the Fourier transform using the fast fourier transform (FFT) algorithm. The Fourier transforms also have several major advantages when calculating the various energy contributions. One such advantage is the ease of calculation of the Coulomb energy as it can be represented as a matrix multiplication in Fourier space. Another advantage is achieved during the calculation of the kinetic energy, as the derivative in real space becomes a multiplication by the wave number in Fourier space. In theory, plane wave basis sets can be made highly accurate by increasing the number of basis functions at the expense of increasing the computational cost.

Practically, the direct use of plane waves is computationally prohibitive because of the requirement to use a large energy cutoff E_{cut} to represent oscillations in higher energy single electron wavefunctions near the nucleus. To over-come this problem, while keeping the advantages related to plane waves, projector augmented wave (PAW) basis functions use a hybrid of real space and frequency dependent functions [59, 63]. The general idea is to represent the highly oscillating region near the nucleus using real space functions and the smooth part of the wavefunctions using the plane waves. This separation is not straightforward because abrupt switching from real space to Fourier space will not decrease the required plane waves appreciably. This is because the number of plane waves required to accurately describe the step-like function at the boundary is large.

The formulation of Blöchl [59] restricts the real space basis to an augmentation sphere of radius r_c^a around the nucleus. Outside this augmentation sphere the wavefunction is represented using a smooth wavefunction $\left(|\widetilde{\psi}_n\rangle\right)$ which can be represented using plane waves. This smooth wavefunction is non-zero inside the augmentation sphere, effectively decreasing the number of plane waves required. The augmentation spheres are non-intersecting and all the quantities related to

the augmentation spheres are represented on spherical coordinates in contrast to the (pseudo) smooth wavefunction $\left(|\widetilde{\psi}_n\rangle\right)$ which is represented on a regular 3D Cartesian grid determined by the plane wave energy cutoff. In this formulation the electron wavefunction can be written as

$$|\psi_n\rangle = |\widetilde{\psi}_n\rangle + \sum_a \sum_i \left(|\phi_i^a\rangle - |\widetilde{\phi}_i^a\rangle\right) \langle \widetilde{p}_i^a | \widetilde{\psi}_n\rangle \tag{26}$$

where, a is the atom index running over all the atoms, i, n corresponds to the quantum numbers l, m, $|\psi_n\rangle$ is the total wavefunction, $|\widetilde{\psi}_n\rangle$ is the (pseudo) smooth wavefunction, $|\phi_i\rangle$ are the all electron partial waves, $|\widetilde{\phi}_i\rangle$ are the (pseudo) smooth partial waves corresponding to each all electron partial wave $(|\phi_i\rangle)$ and $|\widetilde{p}_i\rangle$ are the smooth projector functions. Note that Eq. 26 can be re-written as a linear transform,

$$|\psi_n\rangle = \mathcal{T}|\widetilde{\psi}_n\rangle = \left(1 + \sum_a \mathcal{T}^a\right) |\widetilde{\psi}_n\rangle \tag{27}$$

where $\mathcal{T}$ is a transformation operator which can be written as a sum of local transformation operators $\mathcal{T}^a$ acting inside the augmentation spheres.

The total wavefunction can be expanded as a linear combination of the all-electron partial waves inside the augmentation sphere,

$$|\psi_n\rangle = \sum_i \langle \widetilde{p}_i^a | \widetilde{\psi}_n\rangle |\phi_i^a\rangle, \text{ for } r < r_c^a \tag{28}$$

The corresponding (pseudo) smooth wavefunction can be expanded as a linear combination of the (pseudo) smooth partial waves inside the augmentation sphere as

$$|\widetilde{\psi}_n\rangle = \sum_i \langle \widetilde{p}_i^a | \widetilde{\psi}_n\rangle |\widetilde{\phi}_i^a\rangle, \text{ for } r < r_c^a \tag{29}$$

and outside the augmentation sphere,

$$|\phi_i^a\rangle = |\widetilde{\phi}_i^a\rangle, \text{ for } r > r_c^a \tag{30}$$

The choice of the projector functions $(\widetilde{p}_i^a)$ and the partial waves $(\widetilde{\phi}_i^a, \phi_i^a)$ are

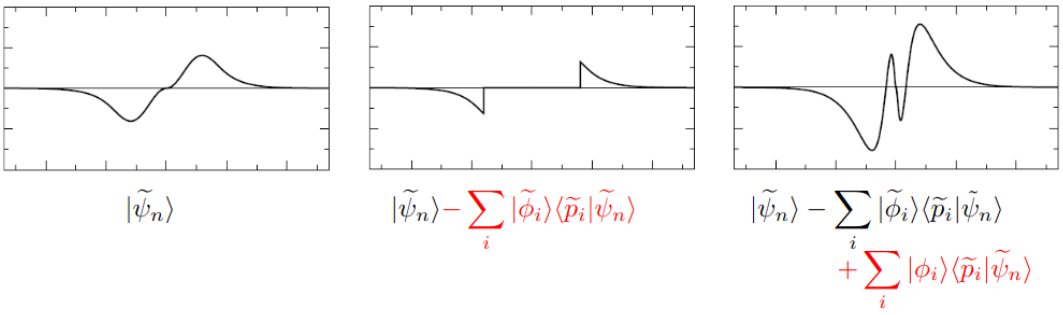

Figure 2.2: Schematic of the basis functions represented in Eq. 31. Figure reproduced from Ref. [65]

not unique and optimized data sets exist for each element of the periodic table [59, 63, 64].

To visualize the expansion we can rewrite the Eq. 26 as,

$$|\psi_n\rangle = \left[|\widetilde{\psi}_n\rangle - \sum_a \sum_i |\widetilde{\phi}_i^a\rangle\langle\widetilde{p}_i^a|\widetilde{\psi}_n\rangle\right] + \sum_a \sum_i |\phi_i^a\rangle\langle\widetilde{p}_i^a|\widetilde{\psi}_n\rangle \tag{31}$$

where the quantity in square brackets is zero inside the augmentation sphere due to the condition enforced in Eq. 29 and the last term adds the correct total wavefunction inside the augmentation sphere due to the condition enforced in Eq. 28. Outside the augmentation sphere the partial wave quantities cancel and the total wavefunction is recovered from the smooth wavefunction due to the condition enforced in Eq. 30. This expansion procedure can be visualized as shown in Fig. 2.2.

Gaussian functions are another popular basis set to expand the wave functions. With the use of Gaussian functions the advantages gained in calculating the Coulomb potential are lost. To overcome this problem, the Gaussian and plane wave (GPW) formalism uses an auxiliary plane wave expansion of the Gaussian functions. The terms of total energy such as kinetic energy and core interaction energies can be calculated analytically in this basis and are therefore computationally cheap. Terms such as the Hartree energy and the exchange correlation energy, which can be cheaply computed in Fourier space, are calculated using the Fourier transforms of the charge density. The use of a plane wave auxiliary basis again enforces the periodicity of the system which is not required when only real space Gaussian functions are used.

In contrast to the PAW formalism, where the charge density or wavefunction

is not available on the same grid without interpolation, in the GPW formalism the charge density is available in both real and Fourier spaces. This has some advantages in imposing boundary conditions while solving the Poisson equation as discussed in Section. 2.7.

The specific choice of basis function is not important provided the basic set is sufficiently large. In most cases, the choice of basis set affects only the computational cost without affecting the results.

2.4.3 Exchange and correlation approximations

The approximations for the exchange correlation functional can be categorized depending on the parameters used to arrive at the functional form. These approximations can be categorized into a hierarchical structure depending on the parameters used in the functional form, with each subsequent level adding new parameters [66]. For example, the local density approximation (LDA) is located on the first level. This level contains the set of all functionals that depend only on the electron density at a point. The generalized gradient approximation (GGA) is located on the next level. It contains the set of functionals that depend on both the density and the gradient of the density at a point [67].

It is expected that with the addition of new ingredients, the accuracy of the approximation increases and by some level chemical accuracy would be reached. In reality this does not occur. Extensive tests of functionals show that functionals higher in the hierarchy do not necessarily result in increased accuracy [68]. This is because within each level there is more than one functional form, each satisfying various physical constraints. Because of this the choice of functional is system dependent and a truly universal functional is not known.

LDA is a good choice for systems with slowly varying density. GGA is nonlocal in density, so includes non-homogeneity on top of LDA. Both these functionals fail to give reasonable results in systems with significant non-local contributions such as those with significant van der Waals interactions. In cases like graphite, when the interlayer binding is due to van der Waals attraction, the application of the GGA functional fails to produce any attraction [69] whereas LDA underestimates the attraction [70].

2.4.4 Van der Waals correction

Attempts to include the van der Waals (vdW) contribution to the correlation functional can be divided into two distinct categories. The first category is based on calculating the pairwise C_6^{AB} coefficient between atom A and atom B. The total vdW contribution is the sum of all such pairwise contributions and is added to the total Kohn-Sham DFT energy as:

$$E_{tot} = E_{KS-DFT} + E_{vdW} \tag{32}$$

The semi-emperical correction due to Grimme et al. (Grimme-D2) is based on pre-calculated static atomic polarizabilities to calculate the individual atomic C_6 coefficients and cutoff radii R^0 [71]. The total van der Waals contribution (E_{vdW}) is given as:

$$E_{vdW} = -\frac{1}{2}\sum_{A,B} f_{damp}(R_{AB}, R_A^0, R_B^0) C_{AB}^6 R_{AB}^{-6} \tag{33}$$

where R_{AB} is the distance between atom A and atom B. The damping term $f_{damp}(R_{AB}, R_A^0, R_B^0)$ is included to ensure that the potentials do not diverge at very short distances between two atoms. To obtain the pairwise interaction coefficient C_{AB}^6 and the equilibrium distance, R_{AB}^0, individual contributions are mixed using predefined rules. C_{AB}^6 is obtained as the geometric mean of the individual atom coefficients, i.e., $C_{AB}^6 = \sqrt{C_A^6 C_B^6}$. R_{AB}^0 is given as the sum of corresponding cutoff radii, i.e., $R_{AB}^0 = R_A^0 + R_B^0$.

This method was then extended in the Grimme-D3 scheme where the pairwise quantities are calculated from first principles to account for the local chemical environment and an additional C_8^{AB} term is added to increase accuracy [72]. The total van der Waals contributions (E_{vdW}) are given as,

$$E_{vdW} = -\frac{1}{2}\sum_{A,B} f_{damp}^6(R_{AB}, R_A^0, R_B^0) C_{AB}^6 R_{AB}^{-6} + \sum_{A,B} f_{damp}^8(R_{AB}, R_A^0, R_B^0) C_{AB}^8 R_{AB}^{-6} \tag{34}$$

where the damping functions $f_{damp}^{6/8}(R_{AB}, R_A^0, R_B^0)$ are again added to prevent divergences at small inter-atom distances. This damping function is further optimised resulting in better performance for non-bonded atoms [73].

The Tkatchenko-Scheffler (TS) approach uses a pairwise contribution similar to Eq. 33 to calculate the vdW energy contribution [74]. The calculation of pairwise

C^6_{AB} coefficients is based on the London formula,

$$C^6_{AB} = \frac{2C^6_{AA}C^6_{AA}}{\left[\frac{\alpha^0_B}{\alpha^0_A}C^6_{AA} + \frac{\alpha^0_A}{\alpha^0_B}C^6_{BB}\right]} \tag{35}$$

where $C^6_{AA/BB}$ is the pairwise coefficient of two atoms A or B and $\alpha^0_{A/B}$ is the static polarizability of atoms A or B. These homo-nuclear quantities are derived from tabulated reference data for free atoms. To account for local chemical environments, the effective coefficient $C^6_{AA,eff}$ is derived from the free coefficients (C^6_{AA}) as

$$C^6_{AA,eff} = \left(\frac{V^{eff}_A}{V^{free}_A}\right) C^6_{AA} \tag{36}$$

where V^{eff}_A is the effective volume of the atoms in the local environment which is derived from the converged electron density. V^{free}_A is the volume of the free atoms. The cutoff radius R^0 is also calculated from the free atom radius and the effective volume as

$$R^0_{AA,eff} = \left(\frac{V^{eff}_A}{V^{free}_A}\right)^{\frac{1}{3}} C^0_{AA} \tag{37}$$

Eqns. 35, Eq. 36 and Eq. 37 assume that the contributions are isotropic. This approximation was relaxed in the many-body dispersion energy method (TS-MBD) by introducing a polarizability tensor instead of atomic polarization [75]. This was calculated using the self-consistent screening equations of classical electrodynamics. This is further improved upon using a range-separated self-consistent screening of atomic polarizabilities. The range separation increases the accuracy as part of the short range correlations are already included in the traditional correlation functional [76].

The second category is based on deriving fully non-local functionals for correlations starting from the fluctuation-dissipation theorem. Unlike the pairwise functionals which are added after the self-consistent density is determined in the Kohn-Sham scheme, these functionals are used at each step of the self consistent iteration. The functional due to Dion et al. approximates the total exchange-correlation energy by splitting it into a local term and a long range non-local term [77]:

$$E_{xc} = E_x^{GGA} + E_c^{LDA} + E_c^{nl} \tag{38}$$

where E_x^{GGA} is the GGA exchange energy, E_c^{LDA} is the local correlation energy approximated using the LDA correlation functional and E_c^{nl} is the non-local correlation functional.

It is written in the form

$$E_c^{nl} = \frac{1}{2} \int d^3r d^3r' n(r) \phi(r, r') n(r'). \tag{39}$$

where $\phi(r, r')$ is the kernel function which can be pre-calculated for efficiency. The exact functional form of exchange and correlation functionals used in Eq. 38 is an active area of research with optimizations available for specific types of systems [78, 79, 80]. In the absence of a universal functional for non-local correlation, the choice of the functional is system dependent, with benchmarks indicating the appropriate functionals for a given system [81, 82].

2.4.5 Periodic boundary correction

Due to the periodic nature of plane waves, the periodicity of the wavefunction is enforced. To study lower dimensional structures such as slabs and molecules a work-around to this enforced periodicity is to include a vacuum region in between periodic images. The size of the vacuum region is chosen such that the potential due to the electron-nucleus system is constant in the region between periodic images, i.e. the periodic images are completely decoupled.

Obtaining a constant potential between periodic images is difficult when there is a net dipole across the structure or the structure is not charge neutral. This is because in these cases the potential is conditionally convergent depending on the shape of the system under consideration. In the first case, the potential decays at a slower rate requiring a larger amount of vacuum region. This increases the computational cost. Several methods exist to decrease the amount of vacuum required based on real space or Fourier space approaches. The general idea is to compensate for the leading terms in a Taylor series expansion of the Coulomb interaction. One of the simplest and more popular methods - inspired by the Makov-Payne correction scheme [83, 84] - is to apply a reverse dipole in the vacuum effectively canceling the effect of the dipole-dipole interaction between periodic images. The exact functional form of the correction depends on the

dimensionality of the system under consideration. This method is demonstrated for a 2D molecular sheet in Fig. 2.3, which shows the average Hartree potential perpendicular to the slab. The dashed line is the uncorrected potential showing a gradient in the Hartree potential v_H and the solid line shows the corrected Hartree potential with a jump at the position of the external dipole. The correction potential due to the applied external dipole, positioned in the red shaded area, is shown by the dotted line. Using this correction the vacuum region cannot be reduced arbitrarily as the correction accounts for only the leading terms in the Taylor expansion. For example, in the correction schemes for slabs shown in Fig. 2.3, up to quadrapole terms ($\frac{1}{R^4}$) are corrected. The vacuum needs be large enough that the next term ($\frac{1}{R^5}$) becomes negligible. Note that the functional form of the correction is dependent on the dimensionality of the system.

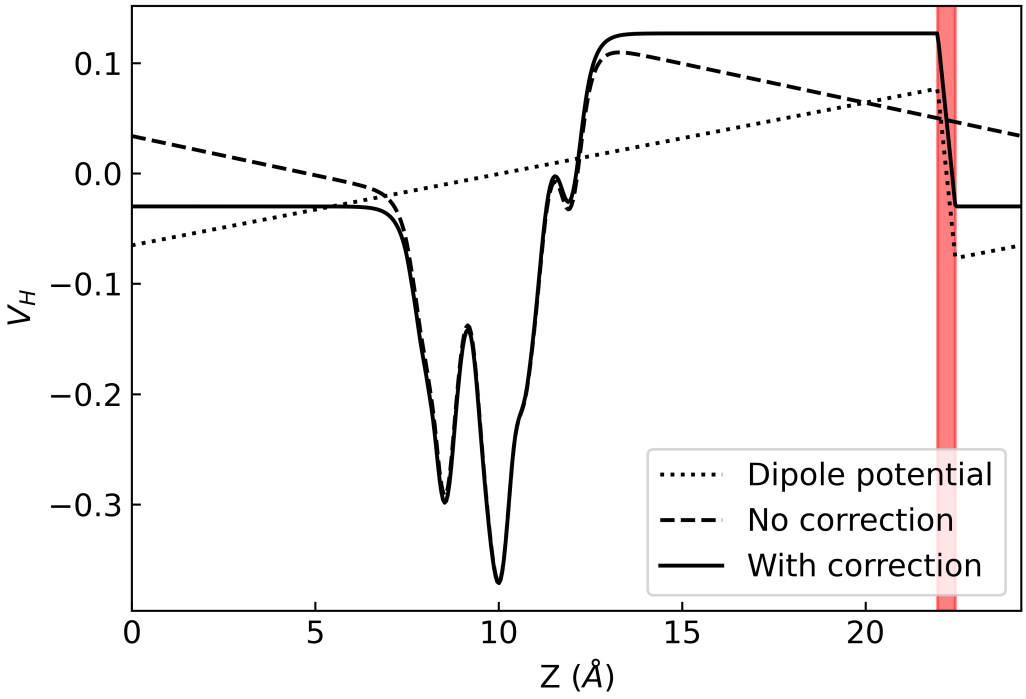

Figure 2.3: The average Hartree potential perpendicular to a 2-dimensional system of NMP molecular slab demonstrating the periodic correction using the Makov-Payne correction scheme [83, 84]. The dashed line is the uncorrected potential showing a gradient in the Hartree potential v_H, the dotted line indicates the dipole electric potential due to the applied external dipole which is indicated by the red shaded area and the solid line shows the corrected Hartree potential with the jump at position of the external dipole.

Another special case occurs when the structure is not charge neutral. This difficulty can be illustrated using the Fourier transform of Hartree potential which is given by $V(G) = \frac{\rho(G)}{G^2}$, where G is the wavenumber of the plane wave.

When the system is charge neutral $\rho(G = 0) = 0$, and the problems associated with division by zero are avoided. However, when the system is not charge neutral $\rho(G = 0) \neq 0$ and the Hartree energy approaches infinity due to division by zero at $G = 0$. One way around this problem is to add a uniform background charge making the unit cell charge neutral. This results in an ambiguous definition of the reference energy of vacuum and a comparison between different systems with different charges becomes difficult.

For some negatively charged systems we cannot have an arbitrarily large vacuum to simulate isolated charged systems. For example, in the case of a negatively charged slab a finite quantum well is formed and, for some particular value of excess charge, the electrons will prefer to occupy the energy levels in the vacuum formed as a result of this quantum well [85].

Similar to the dipole correction method, the necessary potential correction term to the self consistent DFT potential can be calculated using the point counter charge correction (PCC) method [86, 87]. In this scheme, with this background charge added, we can obtain a closed form expression for the correction term for a point-like charge in a cubic unit cell by solving Poisson's equation. This expression can be extended to a random distribution of charges by modeling them as a collection of point charges which preserve the multi-pole moment of the original charge distribution.

Other methods used for periodic corrections include the Martyna-Tuckerman (MT) method for molecules (where the correction is applied in the Fourier transform of the potential in contrast to the real space approaches discussed above [88]), wavelet based methods in which the potential is derived in terms of the charge density expanded in wavelet basis sets [89, 90], the effective screening method (ESM) for slabs where the appropriate Green's function for the Poisson equation is derived to account for non-periodicity [91], terminated Coulomb interaction methods where the Coulomb interaction potential is replaced by a range limited function [92] so that pre-calculated potential correction terms are not required, and real space Poisson solvers. In these cases the boundary conditions for the Poisson equation can be explicitly enforced.

2.5 Dielectric permittivity of layered structures

In the presence of an external electric field the electron density migrates in response to the applied field. For two dimensional systems, when the external field is perpendicular to the layer, the local dielectric constant can be obtained using density functional theory [93, 94]. The local permittivity is related to the change in the local electron density in response to an external applied field (E_{ext}). It is given as,

$$\epsilon(z) = 1 + \frac{\langle p_{ind}(z)\rangle}{\epsilon_0 \langle E_{eff}(z)\rangle} \tag{40}$$

where $\langle p_{ind}(z)\rangle$ is the planar averaged local polarizability and $\langle E_{eff}(z)\rangle$ is the effective electric field. This local permittivity profile ($\epsilon(z)$) can be interpreted as originating only from the local migration of electron density due to the applied external field, while artificially fixing the nuclear positions. This is different from the total permittivity where the movement of ions will also contribute. The local polarizability can be directly calculated from the electron density with and without external electric field. It is given as:

$$\frac{\partial \langle p_{ind}(z)\rangle}{\partial z} = -\langle \rho_{ind}(z)\rangle = \frac{-1}{A}\int_{plane} (\rho_E - \rho_0) dx\ dy \tag{41}$$

where $\langle \rho_{ind}(z)\rangle$ is the planar average of the induced density in response to the applied external electric field, A is the area of the periodic unit cell, ρ_E is the total electron density when an external electric field is applied and ρ_0 is the electron density with no external electric field. The effective electric field ($\langle E_{eff}(z)\rangle$) can be calculated from the Hartree potential with and without an external electric field. It is given as:

$$\langle E_{eff}(z)\rangle = \frac{\partial(\langle V_E^H(z)\rangle - \langle V_0^H(z)\rangle)}{\partial z} \tag{42}$$

where $\langle V_E^H(z)\rangle$ and $\langle V_0^H(z)\rangle$ are the planar averaged Hartree potential with and without external applied electric field, respectively. The procedure to derive the relative permitivity is only valid for isolated systems. This constraint is enforced in calculating the Hartree potential used in Eq. 42 by including the periodic boundary correction to the Hartree potential discussed in Section. 2.4.5.

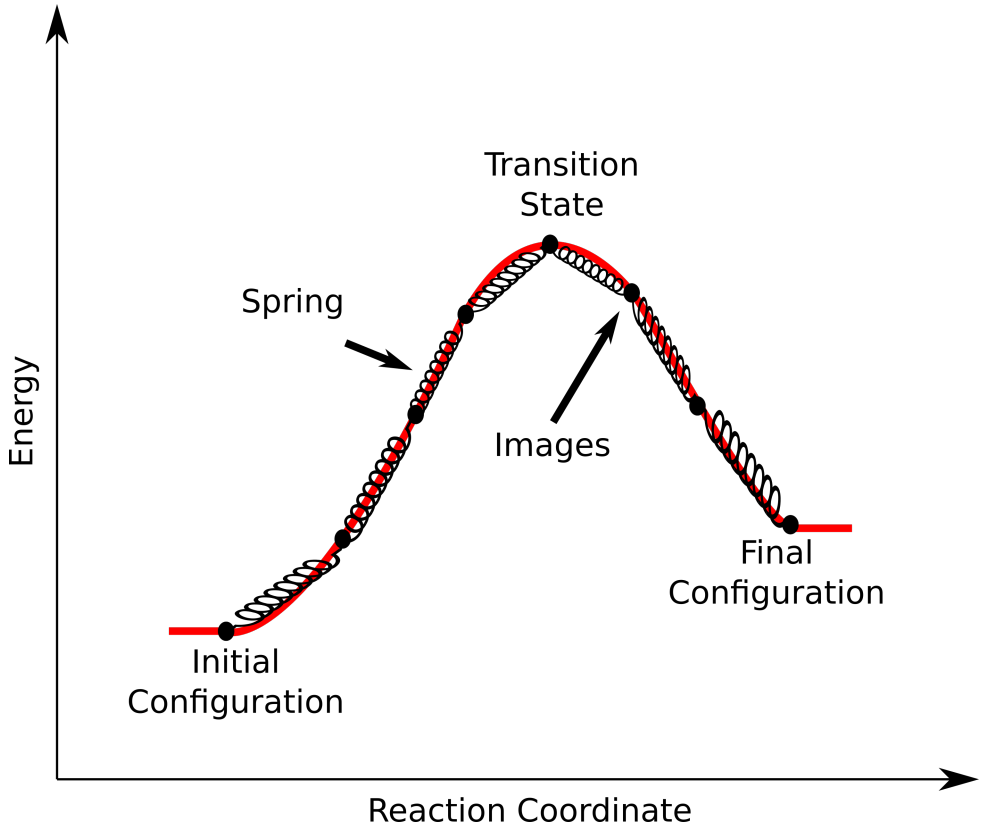

Figure 2.4: Pictorial representation of transition energy barrier and the nudged elastic band (NEB) method.

2.6 Transition path calculations

Of all the spatial arrangements for a set of atoms, the stable configurations present local energetic minima with respect to changes in the atomic coordinates. The most stable configuration (global minimum) is the configuration with the lowest energy. This global minimum can be manipulated via various external perturbations such as temperature, pressure or charge.

Transitions between stable configurations proceed via intermediate configurations which are not stable. The total instantaneous energy required for the transition is the difference between the energy of the intermediate configuration with maximum energy and the starting configuration. This is also known as the barrier energy E_b. The rate of transition between the configurations is given as,

$$R \propto e^{\frac{E_b}{k_b T}} \tag{43}$$

where k_b is the Boltzmann constant and T is the temperature. Because of the exponential dependence on the barrier, the path followed is the one with the lowest energy barrier which belongs to the saddle point with respect to the atomic coordinates. This saddle point can be calculated using the nudged elastic band method (NEB) [95], or the chain method. In the elastic band method the intermediate configurations are connected by springs which store the energy and constrain the configurations from collapsing to the nearest minimum. This ensures a uniform distribution of intermediates as shown in Fig. 2.4.

The maximum energy configuration can be obtained using geometry optimization to minimize the forces on each configuration, where the forces are modified to account for the added springs. The minimization over the usual KS-DFT forces (F_i) is replaced by a minimization over effective forces on configuration i. This is given by:

$$\min[F_i] \rightarrow \min[F_i^{s_\parallel} + F_i^{\perp}] \tag{44}$$

where $F_i^{s_\parallel}$ is the spring force parallel to the transition path and $F_i^{\perp}$ is the force of the configuration parallel to the transition path. The equally spaced configurations obtained using this minimization along the transition path can then be used to obtain the energy barrier for transition. One disadvantage of this method is that the presence of the maximum energy configuration is not guaranteed. One way to get around this is to fit a function to the points, the maxima of the function is then the energy barrier.

To guarantee the presence of a maximum in the energies of configurations the NEB procedure can be modified such that the minimization of the spring-dependent force on the maximum energy image given in Eq. 44 is replaced with

$$\begin{aligned} \min[F_{max}] &\rightarrow \min[F_{max} - 2F_{max}^{\parallel}] \\ &\rightarrow \min[-F_{max}^{\parallel} + (F_{max} - F_{max}^{\parallel})] \end{aligned} \tag{45}$$

Here, F_{max} is the total force on the maximum energy configuration and $F_{max}^{\parallel}$ is the force parallel to the transition path on the maximum energy configuration [96]. From the last line in Eq. 45 it can be concluded that the minimization of force will move the configuration up in the potential energy surface parallel to the transition path and down the potential energy surface perpendicular to the path. This method is also known as climbing image - nudged elastic band method

(CI-NEB).

2.7 Field effect transistor

The field effect transistor typically consists of a gate which controls the current–voltage characteristic of the device via the application of a voltage. This gate voltage results in an external field leading to movement of electrons. The accumulation/depletion of electrons can be measured as a change in the I-V characteristic curve of the device.

Typically the gate is separated from the device via an insulating layer which acts as a dielectric intermediate layer. The gate, the insulating layer and the device can be modelled as a capacitor where the gate is one terminal and the bulk device is another terminal. Within this picture the gate voltage and the induced charge are related via the capacitor equation given as,

$$Q_{eff} = C_{eff} V_g \tag{46}$$

where Q_{eff} is the effective charge that is rearranged, C_{eff} is the effective capacitance and V_g is the applied gate voltage. To simulate the gate-like behavior within DFT, two approaches have been introduced: the first relies on controlling the charge (Q_{eff}) [97] and the second relies on controlling the external gate voltage (V_g) [98].

Both these approaches enter via the Hartree potential, which is a function of the electron density in the unit cell. The Hartree potential satisfies the generalized Poisson equation given as

$$-\nabla \cdot (\epsilon(x)\nabla v_H(x)) = 4\pi n(x) \tag{47}$$

where x is the spatial variable, $\epsilon(x)$ is the spatially dependent dielectric constant, v_H is the Hartree potential and $n(x)$ is the electron density. The solution to the second order differential equation requires defining boundary conditions.

Within the first approach the charge is introduced as an extra electron density added to the unit cell. The effect of the gate is introduced as Dirichlet (constant potential) boundary conditions on one side of the device and von Neumann (no potential gradient) boundary conditions on the other side of the device to mimic vacuum. The insulator-like behavior is introduced via a dielectric region between

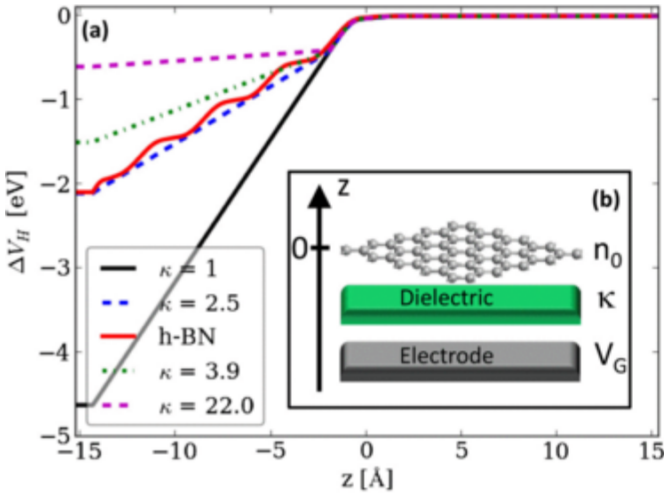

Figure 2.5: (a) Hartree potential for device shown in (b) for different dielectric regions in between the gate and the graphene layer. Figure reproduced from Ref. [97]

the device and the enforced boundary conditions. A device simulated using this approach is shown in Fig. 2.5. This device consists of a graphene layer and a dielectric region as shown in the insert.

Within the second approach the relative voltage is fixed by applying constraints to the Hartree potential in the unit cell during the solution of the Poisson equation given in Eq. 47. To decouple the periodic images, von Neumann boundary conditions are applied to the edge of the unit cell to mimic vacuum. A device simulated using this approach is shown in Fig. 2.6. This device consists of a graphene nanoribbon with edge-adsorbed water molecules sandwiched in between a dielectric region as shown in the insert. In this case a voltage of 10 V is applied to the bottom the dielectric region (blue) and a voltage of 0 V is applied to the top of the dielectric region. The applied gate region is shown by the red line.

2.8 Continuum solvation model

Solvation describes the interaction between solute and solvent in a solution. This interaction can be stabilizing (favorable solute-solvent interaction) or non-stabilizing (unfavorable solute-solvent interaction). In order to classify a particular solute-solvent interaction as favorable or unfavorable we need to calculate the free energy of solvation, ΔG^{sol}. It is defined as:

$$\Delta G^{sol} = G_{solvent} - G_{vacuum}$$

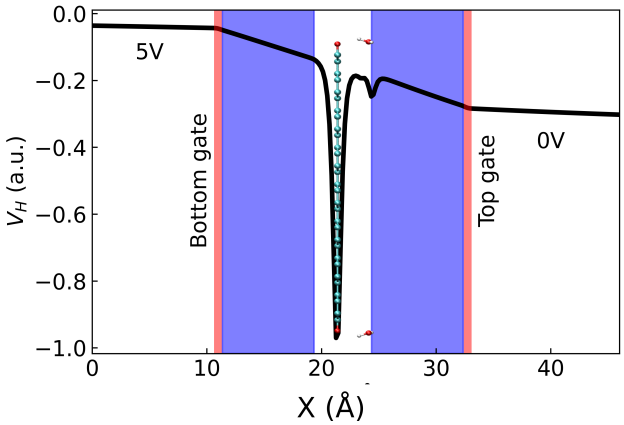

Figure 2.6: Hartree potential is for device where a graphene nanoribbon with edge-adsorbed water molecules sandwiched in between a dielectric region. A voltage of 10 V is applied to the bottom of the dielectric region (blue) and a voltage of 0 V is applied to the top of the dielectric region.

where $G_{solvent}$ is the free energy of the solute in solvent and G_{vacuum} is the free energy of the isolated solute in vacuum. This solvation free energy can be calculated by either an explicit solvation model where we explicitly include each solvent molecule along with the solute in the simulation or by an implicit solvent model where we treat the solvent molecules as a continuous dielectric which is dependent on the solute electron density.

Explicit ab-initio modeling of solute particles in solvent molecules is computationally prohibitive in some cases because of the large unit cell sizes needed and the requirement to sample a large number of different configurations. However, if the molecule interacts with the solute predominantly via Coulomb-like interaction, we can use an implicit solvation model. Here, we model the solvent semi-classically as a continuous polarizable medium in which the solute particles are present. This is the polarizable continuum model (PCM) originally proposed by Tomasi and co-workers [99].

In the self-consistent continuum solvation (SCCS) model described below [87], a key assumption is that the dielectric medium self-consistently depends on the electronic density of the solute:

$$\epsilon(\vec{r}) = \epsilon(\rho^{elec}(\vec{r}))$$

Far from the solute, the dielectric constant is equal to the bulk dielectric constant (ϵ) of the solvent - emulating free solvent - and there is no polarization charge.

Inside the solute, all the electrons are taken into account explicitly in the Kohn-Sham energy calculation. As a result, the dielectric constant is set equal to 1 and there is no polarization charge. However, at the boundary of the solute and the solvent, there is an ambiguous region where the solute and solvent electron densities have no independent identity, creating partially bound electrons. Here, we assume that the dielectric constant is dependent on the solute electron density. This dielectric constant will smoothly vary between 1 and the bulk dielectric constant (ϵ). Loosely speaking, the value of the dielectric constant in the region indicates how "solute-like" the electron density in that region is.

To summarize, the electron density dependent dielectric constant $\epsilon(\rho^{elec}(\vec{r}))$, of the solvent is defined as:

$$\epsilon(\rho^{elec}(\vec{r})) = \begin{cases} 1, & \text{if } \rho^{elec} > \rho_{max} \\ s(\rho^{elec}), & \text{if } \rho_{min} < \rho^{elec} < \rho_{max} \\ \epsilon, & \text{if } \rho^{elec} < \rho_{min} \end{cases}$$

where $s(\rho^{elec})$ is the shape function, which defines the smooth variation of the dielectric constant at the boundary between the solute and solvent. It is a function of the bulk dielectric constant (ϵ) of the solvent and the density parameters, ρ_{min} and ρ_{max}, which define the bulk "solute-like" and bulk "solvent-like" density values, respectively.

The solvation free energy (ΔG^{sol}) within the SCCS model is given by:

$$\Delta G^{sol} = \Delta G^{el} + \Delta G^{cav} + \Delta G^{rep} + \Delta G^{disp} + P\Delta V \tag{48}$$

The first term in Eq. 48 accounts for the electrostatic effects while the remaining terms account for non-electrostatic effects. Here:

- ΔG^{el} accounts for the electrostatic interaction between the solute and solvent.
- ΔG^{cav} accounts for the energy required to create a cavity in the solvent in which the solute is placed. This process is independent of the nature of solute and depends only on its geometry.
- ΔG^{rep} accounts for the short range repulsion due to the Pauli exclusion principle.
- ΔG^{disp} accounts for the van der Waals dispersion interaction between the

solute and the solvent.

- $P\Delta V$ accounts for the change in volume of solvated system.

Each of these terms will be discussed below.

2.8.1 Electrostatic contribution to solvation

For a solute embedded in an continuous dielectric, the total electrostatic potential ($\phi^{tot}(r)$) can be determined by the standard Maxwell equation:

$$\nabla.\vec{D}(\vec{r}) = \rho^{solute}(\vec{r}) \tag{49}$$

where $D(r)$ is the displacement field and ρ^{solute} is the solute charge density which is equal to the sum of the electron charge density (ρ^{elec}) and the ionic charge density (ρ^{ions}) of the solute. The displacement field $D(\vec{r})$ is defined as:

$$\vec{D}(\vec{r}) = \epsilon_0\vec{E}(\vec{r}) + \vec{P}(\vec{r}) = \epsilon(\vec{r})\vec{E}(\vec{r}) \tag{50}$$

where $\vec{E}(\vec{r})$ is the electric field and $\vec{P}(\vec{r})$ the polarization. The total electrostatic potential ($\phi^{tot}(\vec{r})$) is a solution of the Poission equation:

$$\nabla\epsilon(\rho^{elec}(\vec{r}))\nabla\phi^{tot}(\vec{r}) = -\rho^{solute}(\vec{r})$$

Using Eq. 50, this can be reformulated to a vacuum-like Poission equation:

$$\nabla^2\phi^{tot}(\vec{r}) = -(\rho^{solute}(\vec{r}) + \rho^{pol}(\vec{r}))$$

where the polarization charge density ($\rho^{pol}(\vec{r})$) is given by,

$$\rho^{pol}(\vec{r}) = -\nabla.\vec{P}(\vec{r}) = \nabla.\left((\epsilon(\rho^{elec}(\vec{r})) - 1)\nabla\phi^{tot}(\vec{r})\right)$$

Using this self-consistent electrostatic potential ($\phi^{tot}(\vec{r})$), the electrostatic energy due to this potential can be defined as:

$$E^{el} = \frac{1}{2}\int \vec{E}(\vec{r}).\vec{D}(\vec{r})\ d\vec{r}$$

which can be further simplified into an expression with known quantities, namely $\phi^{tot}(\vec{r})$ and $\epsilon(\rho^{elec}(\vec{r}))$:

$$E^{el} = \frac{1}{2}\int \epsilon(\rho^{elec}(\vec{r}))|\nabla\ \phi^{tot}|^2\ d\vec{r}$$

This can be decomposed into two components:

$$E^{el} = E^{solute} + E^{pol}$$

where the polarization electrostatic energy (E^{pol}) is the electrostatic interaction energy between the polarization charge and the electrostatic potential due to the solute charge density in vacuum. It is defined as:

$$E^{pol} = \frac{1}{2}\int \rho^{pol}(\vec{r})\phi^{solute}(\vec{r})d\vec{r}$$

The solvation terms [100] in the Kohn-Sham density functional theory formalism can be formally derived from the total thermodynamic free energy within the Born-Oppenheimer approximation using Levy's constrained search algorithm [101]. The Kohn-Sham energy expression is given as:

$$E^{tot}[\rho^{elec}, \rho^{ions}] = (E^{tot}[\rho^{elec}, \rho^{ions}])_{solute} + E^{pol}[\rho^{elec}, \rho^{ions}]$$

In practice, the polarization charge density need not be calculated explicitly. Instead, the total Kohn-Sham energy can be rewritten as:

$$E^{tot}[\rho^{elec}, \rho^{ions}] = E^{kin}[\rho^{elec}] + E^{el}[\rho^{elec}, \rho^{ions}] + E^{xc}[\rho^{elec}]$$

where $E^{kin}[\rho^{elec}]$ is the kinetic energy of the non-interacting solute electrons, $E^{xc}[\rho^{elec}]$ is the exchange-correlation energy of the solute electrons and E^{el} is the total electrostatic energy.

Using this total energy, the electrostatic solvation free energy $\Delta G^{el}(\epsilon_0, \rho_{min}, \rho_{max})$, (the first term in Eq. 48) can be calculated as the difference between the *ab-initio* energy in vacuum and solvent. The entropic change due to the change in geometry of the solute in gas and in solution is neglected as it is very small.

2.8.2 Non-electrostatic contributions to solvation

The non-electrostatic terms in Eq. 48 all depend on the nature of the cavity formed by the solute in the solvent, and in particular on ν, the 'quantum volume'

occupied by the solute charge density, and the surface area of this volume, S [102].

The cavitation energy is the free energy required to create a cavity around the solute in the bulk solvent. Uhlig initially proposed that the work required to produce the cavity could be expressed as a product between the surface tension of the solvent and the surface area of a cavity [99, 103]:

$$\Delta G^{cav} = \gamma S$$

The repulsion (ΔG^{rep}) and dispersion (ΔG^{disp}) terms are assumed to depend linearly on the surface area and quantum volume, respectively:

$$\Delta G^{rep} + \Delta G^{disp} = \alpha S + \beta \nu$$

where the parameters α and β are solvent specific fitting parameters.

The final expression for the free energy of solvation, ΔG^{sol}, given in Eq. 48 can be rewritten as:

$$\Delta G^{sol} = ((E^{tot})_{solution} - (E^{tot})_{vacuum}) + \gamma S + \alpha S + \beta \nu + P\Delta V$$

where $(E^{tot})_{solution/vacuum}$ is the DFT energy calculated in solution/vacuum.

The final term in Eq. 48, $P\Delta V$, is negligible for the systems under consideration here. As we always consider the difference in solvation energy between layered slabs of different thickness when calculating the binding energy, the volume-dependent terms cancel and so can be safely ignored. This is also true for the $\beta\nu$ term.

α and γ both depend linearly on the surface area of the cavity and, in practice, are combined into one adjustable parameter $(\gamma + \alpha)$. However, α is usually very small compared to γ, i.e., $\alpha << \gamma$, so this term is referred to only as the surface tension. ρ_{min} and ρ_{max} are also tunable parameters, here fixed to 0.0001 and 0.005, respectively.

An important thing to note is that the polarization charges also need to be included in the periodic boundary corrections described in Section. 2.4.5, especially for calculations involving anions [104].

2.9 Dynamics

Properties of a system such as diffusion and solvation depend of the collective motion of more than one nucleus at a given temperature (T). Within the Born-Oppenheimer approximation discussed in Section. 2.1 the motion of nuclei can be derived using the nuclear part of the total Hamiltonian given in Eq. 8. The nuclear part of the Hamiltonian can be rewritten in the form

$$H = \hat{T}_{nuc} + \left[E_e + \hat{V}_{nuc-nuc}\right] = \sum_I \frac{p_I^2}{2M_I} + V(\{R_I\}) \tag{51}$$

where p_I is the momentum of nucleus I and $V(\{R_I\})$ is the potential energy function dependent on all the nuclei. The equation of motion corresponding to the Hamiltonian in Eq. 51 for the nuclei is given as

$$\begin{aligned} \dot{\alpha_I} &= \frac{\partial H}{\partial p_I^\alpha} = \frac{p_I^\alpha}{M_I} = v_I^\alpha \\ \dot{p_I^\alpha} &= -\frac{\partial H}{\partial \alpha_I} = -\frac{\partial V(\{R_I\})}{\partial \alpha_I} = F_I^\alpha = M_I a_I^\alpha \end{aligned} \tag{52}$$

where $\alpha_I \in \{x_I, y_I, z_I\}$ is the position of nucleus I, p_I^α is the momentum of nucleus I in direction α, F_I^α is the force on nucleus I in direction α and a_I^α is the acceleration of nucleus I in direction α. Eq. 52 corresponds to Newton's equation of motion for the nuclei [105]. The flowchart showing an implementation of Eq. 52 is shown in Fig. 2.7.

The motion depends on the electrons of the system via the electronic energy (E_e) which can be obtained by solving the electronic equation in Eq. 4 using DFT approximations. In this scheme, the force F_I^α corresponds to the Hellmann-Feynman forces and is also known as Born-Oppenheimer ab-initio molecular dynamics (BO-AIMD).

In some cases the solution of the electronic equation in Eq. 4 is computationally prohibitive using any of the available methods. In such cases the potential $V(\{R_I\})$ is approximated using a combination of rules based on the relative orientations of nuclei. These rules are also known as force fields. This method of potential approximation without the exact solution of electronic Hamiltonian is known as classical molecular dynamics (MD).

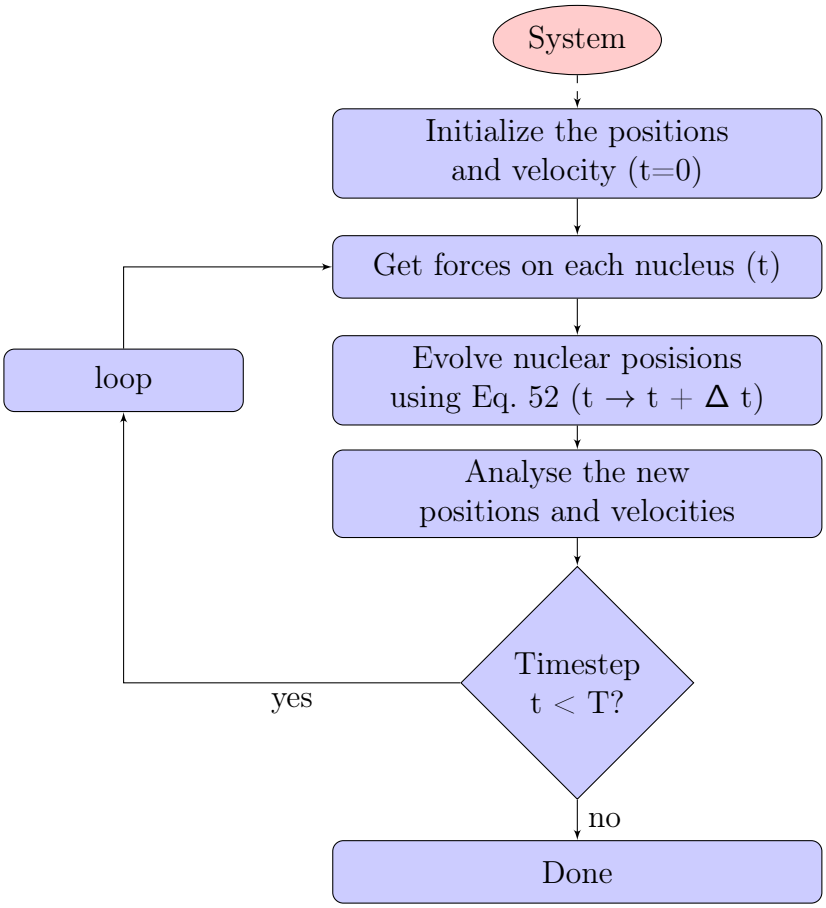

Figure 2.7: Typical flow chart of molecular dynamics calculations.

2.9.1 Integrating the equations of motion

The nuclear positions are evolved using a finite difference approximation of Eq. 52. The simplest form of this finite difference algorithm can be derived using the Taylor series expansion of position. For small timestep (δt) the Taylor series expansion of position around current time (t) is given as,

$$r(t+\delta t) = r(t) + v(t)\delta t + \frac{1}{2}a(t)\delta t^2 + \mathcal{O}(\delta t^3) \tag{53}$$

where $r(t+\delta t)$ is the position of particle at time $t+\delta t$, $v(t)$ is the velocity at time t and $a(t)$ is the acceleration at time t. Increasing the accuracy of Eq. 53 requires higher order derivatives which are not directly available. The accuracy of this expansion method can be trivially extended by considering both forward expansion given in Eq. 53 and reverse expansion given as,

$$r(t-\delta t) = r(t) - v(t)\delta t + \frac{1}{2}a(t)\delta t^2 + \mathcal{O}(\delta t^3) \tag{54}$$

Summing Eq. 53 and Eq. 54 we get the position at time $t + \delta t$ as,

$$r(t + \delta t) = 2r(t) - r(t - \delta t) + a(t)\delta t^2 + \mathcal{O}(\delta t^4) \tag{55}$$

which introduces an error of $\mathcal{O}(\delta t^4)$ in comparison to $\mathcal{O}(\delta t^3)$ by direct Taylor expansion [106]. Another advantage of using Eq. 55 is that the position is computed in terms of positions and acceleration which are directly available quantities. Note the velocity can also be obtained using a similar finite difference method and has no effect on the actual trajectory. The calculated velocity at time $t + \delta t$ can be obtained with an minimum error of $\mathcal{O}(\delta t^2)$ as,

$$v(t + \delta t) = \frac{r(t + \delta t) - r(t)}{\delta t} \tag{56}$$

which requires storage of two positions at times $t + \delta t$ and t. The precision can be improved ($\mathcal{O}(\delta t^3)$) for time t which is a time step behind the position as,

$$v(t) = \frac{r(t + \delta t) - r(t - \delta t)}{\delta t} \tag{57}$$

This requires the storage of three positions at times $t + \delta t$, t and $t - \delta t$. The storage problem can be improved using the velocity Verlet scheme which is equivalent to Eq. 53 terminated at the second order term for position and the velocity. It is calculated as

$$v(t + \delta t) = v(t) + \frac{1}{2}\left[a(t) + a(t + \delta t)\right]\delta t \tag{58}$$

A direct implementation of this equation requires the storage of acceleration at two different time steps which is avoided in the three step process [107]. The three steps velocity Verlet scheme is,

1. evolve velocity by half time step: $v(t + \frac{1}{2}\delta t) = v(t) + \frac{1}{2}a(t)\delta t$
2. evolve positions by complete time step: $r(t + \delta t) = r(t) + v(t + \frac{1}{2}\delta t)\delta t$
3. evolve velocity by half time step $v(t + \delta t) = v(t + \frac{1}{2}\delta t) + \frac{1}{2}a(t + \delta t)\delta t$

where the storage of quantities at only one time is necessary. The choice of time step δt is important and is dependent on the mass of the atoms in the simulation. Atoms with lower mass generally requires a lower time step as compared to heavy

atoms.

2.9.2 Force Field

The force fields are designed to reproduce properties such as density, bond energies, vibrational frequency, binding energies and volume. The design of force fields involves two steps: the first is to determine the functional form of the force field and second is to fit the parameters to produce experimental data. In some cases, in addition to the observable properties, various quantities derived from quantum mechanical calculations are also used as target quantities to fit.

The choice of force field is not unique and generally depends on the quantity that is calculated in the MD simulation. For example, if reproducing the density or the volume of organic molecular solvents is desired then OPLS-AA force fields can be used [108]. If determining properties depending on the polarizability of water is important then the TIP4P force field can be used [109]. If accurate bond dissociation is required then the reaxFF force field can be used [110]. In some cases, such as molecular solvent mixtures, more than one type of force field is needed to model the different types of molecules and inter-molecule interactions.

Recently, quantum mechanical force fields have been developed, in which the force field is fitted to reproduce quantum mechanical calculations. The inputs for such force fields are bi-spectrum components which represent the local environment of the atoms on a 4-dimensional sphere [111]. As these force fields replicate quantum mechanical calculations, typically DFT, the approximations used to calculate the target quantities are inherent in the force field. This could be a problem if there is significant van der Waals or hydrogen bonding contributions, as inaccurate descriptions of these quantities will result in incorrect volumes or densities.

In the case of organic liquids the 'Optimized Potentials for Liquid Simulations' (OPLS) force field reproduces the correct bulk properties and intermolecular interactions [108]. In the OPLS force field the atoms are modeled as point charges. The total energy as a function of nuclear positions is given as,

$$E\left(r^N\right) = E_{\text{bonds}} + E_{\text{angles}} + E_{\text{dihedrals}} + E_{\text{nonbonded}} \tag{59}$$

where r^N is the set of coordinates of all N atoms, E_{bonds} is the bonding energy

between two bonded atoms, E_{angles} is the three atom energy which is written as a function of angle, $E_{\text{dihedrals}}$ is the four atom energy which is written as function of dihedral angle and $E_{\text{nonbonded}}$ is the non covalent bonded energy term containing van der Waals, hydrogen bonding and Coulomb interactions. Here, the first three terms are intra-molecular terms and the last term is the intermolecular energy term. The functional form of each energy term is discussed below.

The bonding energy or stretching is modeled as a spring around the equilibrium bond distance. It is given as,

$$E_{\text{bonds}} = \sum_{\text{bonds}} K_r(r - r_0)^2 \tag{60}$$

where the sum is over all the bonds, K_r is the spring constant and r_0 is the equilibrium bond distance. The three atom energy term is modeled using a parabolic approximation around the equilibrium angle and represents the energy of bending two bonds around a center. It is given as,

$$E_{\text{angles}} = \sum_{\text{angles}} k_\theta(\theta - \theta_0)^2 \tag{61}$$

where the sum is over all the triplets such that two atoms of the triplets are bonded to a common atom, k_θ is the energy of bending around the equilibrium and θ_0 is the equilibrium angle. The four atom energy term or dihedral energy represents the torsional contributions. This energy is generally represented as a Fourier series expansion and is given as,

$$\begin{aligned} E_{\text{dihedrals}} = \sum_{\text{dihedrals}} & \frac{V_1}{2}\left[1 + \cos(\phi - \phi_1)\right] + \frac{V_2}{2}\left[1 - \cos(2\phi - \phi_2)\right] \\ & + \frac{V_3}{2}\left[1 + \cos(3\phi - \phi_3)\right] + \frac{V_4}{2}\left[1 - \cos(4\phi - \phi_4)\right] \end{aligned} \tag{62}$$

where the sum is over all the four atom sets such that the four atoms are connected continuously via bonds, ϕ is the dihedral angle, $\phi_{1,2,3,4}$ are the phase factors and $V_{1,2,3,4}$ are the Fourier series expansion coefficients. The non covalent bonding components is given as,

$$E_{\text{nonbonded}} = \sum_{i>j} f_{ij}\left(\frac{A_{ij}}{r_{ij}^{12}} - \frac{C_{ij}}{r_{ij}^{6}} + \frac{q_i q_j e^2}{4\pi\epsilon_0 r_{ij}}\right) \tag{63}$$

where the sum is over all the atom pairs such that the two atoms are at least 3 bonds apart (1-4 contribution), r_{ij} is the distance between atom i and atom j, A_{ij},C_{ij} are the usual 6-12 Lennard-Jones potential parameters, q_i is the charge on atom i and f_{ij} is the fudge factor. The fudge factor is taken as $f_{ij} = 0.5$ for atoms that are connected by three intermediate bonds and $f_{ij} = 1$ otherwise.

The 6-12 Lennard-Jones potential can be re-written in terms of the energy of interaction and the distance betweeen the atoms at equilibrium. The new recast form is given as,

$$\begin{aligned} E_{\mathsf{LJ}} &= \sum_{i>j} \frac{A_{ij}}{r_{ij}^{12}} - \frac{C_{ij}}{r_{ij}^{6}} \\ &= \sum_{i>j} \epsilon_{ij} \left(\frac{\sigma_{ij}}{r_{ij}^{12}} - \frac{\sigma_{ij}}{r_{ij}^{6}} \right) \end{aligned} \tag{64}$$

where ϵ_{ij} is the energy of interaction at equilibrium and σ_{ij} is the equilibrium distance. Another advantage of this new form is that the parameters can be tabulated for pairs of similar atoms. For two different atoms the parameters can be derived using mixing rules.

If the atoms are modeled as hard spheres then the Lorentz rules [112] are used to determine the equilibrium distance between two atoms of different type. The rule is given as,

$$\sigma_{ij} = \frac{\sigma_i + \sigma_j}{2} \tag{65}$$

where σ_i is the equilibrium distance between similar atoms of type i. In some cases the atoms are modeled as soft spheres – in this case the Good-Hope rule [113] is used to determine the equilibrium distance between two atoms of different type. The rule is given as,

$$\sigma_{ij} = \sqrt{\sigma_i \sigma_j} \tag{66}$$

Similarly, the energy of interaction between two atoms of different type can be derived from the interaction energy of atoms of same kind using the Berthelot rule [114] given as,

$$\epsilon_{ij} = \sqrt{\epsilon_i \epsilon_j} \tag{67}$$

where ϵ_i is the binding energy of similar atom of type type i.

In the case of OPLS-AA potentials, the Good-Hope rule given in Eq. 66 is used to determine the equilibrium distance and Berthelot rule in Eq. 67 is used to determine the interaction energy.

2.9.3 Ensembles and averages

In statistical mechanics a micro state of N particles is defined as the set of positions and momenta $\{r^N, p^N\}$ of all particles. The phase space is defined as all the possible micro states for a system of N particles. An ensemble is defined as a phase space with certain restrictions or constraints which are generally a set of conserved quantities. When the conserved quantities are the number of particles (N), volume (V) and energy (E) the ensemble is known as the micro-canonical ensemble (NVE). When the conserved quantities are the number of particles (N), volume (V) and temperature (T) the ensemble is known as the canonical ensemble (NVT) and when the conserved quantities are the number of particles (N), volume (V) and pressure (P) the ensemble is known as the isothermal-isobaric ensemble (NPT).

The ensemble average of an observable is the average of an observable in the phase space. For a observable $O(r^N, p^N)$ of a micro state $\{r^N, p^N\}$, the ensemble average of the observable (O) is given as,

$$\left\langle O(r^N, p^N)\right\rangle_{\text{ensemble}} = \int_{\text{phasespace}} dp^n dr^N O(r^N, p^N)\rho(r^N, p^N) \tag{68}$$

where $\rho(r^N, p^N)$ is the probability density. $\rho(r^N, p^N)\Delta r^N \Delta p^N$ indicates the probability of micro state $\{r^N, p^N\}$ and the integration is over all the phase space. Similarly a time average is defined as,

$$\begin{aligned}\left\langle O(r^N, p^N)\right\rangle_{\text{time}} &= \lim_{t\to\infty}\int_{\tau=0}^{t} d\tau O(r^N(\tau), p^N(\tau)) \\ &\approx \frac{1}{T}\sum_{i=0}^{T} O(r^N, p^N)\end{aligned} \tag{69}$$

where the discrete time average can be directly calculated from snapshots of a molecular dynamics simulation. In the limit of a large number of snapshots, according to the ergodic hypothesis

$$\left\langle O(r^N, p^N)\right\rangle_{\text{ensemble}} = \left\langle O(r^N, p^N)\right\rangle_{\text{time}} \tag{70}$$

This is the approximation that is used to calculate ensemble averages in molecular dynamics simulations.

2.9.4 Thermostats and Barostats

The equation of motion in Eq. 52 corresponds to a Hamiltonian, so the conserved quantities are the energy, volume and number of particles (NVE). In some cases it is desirable to control the temperature or pressure of the simulation – in such a case we use a thermostat to control the temperature or a barostat to control the pressure.

The temperature of N particles can be calculated as,

$$T = \frac{2\left\langle K\right\rangle}{3\mathrm{N}k_B} = \frac{1}{M}\sum_i T_i \tag{71}$$

where $\langle K\rangle$ is the ensemble average of the total kinetic energy, k_B is the Boltzmann's constant, M is the total number of time steps and $T_i = \frac{2K_i}{\mathrm{N_f}k_B}$ is the temperature of snapshot i. The job of the thermostat is to maintain a constant average temperature (T) and not fix T_i for individual snapshot. Fixing T_i for individual snapshot corresponds to fixing the total kinetic energy of the system which is not desirable.

The pressure of a three dimensional system of N particles can be calculated using the virial formula as

$$\begin{aligned} P &= \frac{Nk_B T}{V} + \frac{1}{3V}\left\langle \sum_{i<j}^{N} r_{ij}\cdot f_{ij}\right\rangle \\ &= \frac{1}{3V}\left\langle K + \sum_{j}^{N'} r_j \cdot f_j\right\rangle \\ &= \frac{1}{3V}\frac{1}{M}\sum_i^M\left[K_i + \sum_j^{N'} r_j^i \cdot f_j^i\right] \quad = \frac{1}{3V}\frac{1}{M}\sum_i^M P_i \end{aligned} \tag{72}$$

where V is the volume, r_j is the position vector, f_j is the force vector, N' indicates the number of interacting atoms in the periodic system and the dot $(\cdot)$ indicates

a dot product. The sum over dot products includes pairwise the two-atom, three-atom, four-atom, many-atom and long-range interactions. As for the thermostat, the aim of the barostat is not to fix the individual snapshot pressure P_i but the average pressure P for a simulation window.

Developing thermostats or barostats is a active area of research with several different strategies. Each of the available thermostats or barostats have some advantages with the choice dependent on the target of the simulation.

2.10 Free energy calculation

For a system of N particles with volume V and temperature T in the canonical ensemble, the partition function (Q) is given as

$$Q(N, V, T) = \frac{1}{N!h^{3N}} \int e^{-\beta H(r^N, p^N)} dr^N dp^N \tag{73}$$

where N is the number of particles, $\beta = k_B T$, h is Planck's constant, $H(r^N, p^N)$ is the Hamiltonian given in Eq. 51 and the integration is over all the phase space. The Helmholtz free energy (A) of the system is given as

$$A = -\frac{1}{\beta} \ln Q = \frac{1}{\beta} \ln \frac{1}{Q} \tag{74}$$

substituting Eq. 73 in Eq. 74

$$A = \frac{1}{\beta} \ln \frac{1}{\frac{1}{N!h^{3N}} \int e^{-\beta H(r^N, p^N)} dr^N dp^N} \tag{75}$$

Using the identity $e^{\beta H} e^{-\beta H} = 1$ in the numerator,

$$\begin{aligned} A &= \frac{1}{\beta} \ln \frac{\int e^{\beta H(r^N, p^N)} e^{-\beta H(r^N, p^N)} dr^N dp^N}{\int e^{-\beta H(r^N, p^N)} dr^N dp^N} \\ &= \frac{1}{\beta} \ln \int e^{\beta H(r^N, p^N)} \rho(r^N, p^N) dr^N dp^N \end{aligned} \tag{76}$$

where $\rho(r^N, p^N)$ probability density of micro state $\{r^N, p^N\}$. In the second line the quantity inside the natural logarithm is of the from of an ensemble average shown in Eq. 68. The ensemble average expression is

$$A = \frac{1}{\beta} \ln \left\langle e^{\beta H(r^N, p^N)} \right\rangle \tag{77}$$

where the ensemble average can be done using MD simulations. However, due to the presence of the exponential in energy, the averaging is generally unstable as the higher energy configurations will be poorly sampled but will contribute exponentially. As a result, the direct computation of free energies using this method is avoided.

In most cases we are interested in the free energy change of transition from state 0 to state 1 as it indicates the spontaneity of transition. The free energy change between state 0 with Hamiltonian H_0 to state 1 with Hamiltonian H_1 can be obtained using Eq. 73 as,

$$\Delta A = -\frac{1}{\beta} \ln \left(\frac{Q_1}{Q_0} \right) \tag{78}$$

where Q_i is the partition function of the corresponding state i. This can be further simplified by multiplying the identity $e^{\beta H_0} e^{-\beta H_0} = 1$ in the numerator giving the final expression as

$$\Delta A = -\frac{1}{\beta} \ln \left\langle e^{-\beta(H_1 - H_0)} \right\rangle_0 \tag{79}$$

where the subscript indicating the ensemble average is in the phase space of state 0. Again this leads to under sampling in the phase space of state 1 as they are generally inaccessible for a system in state 0. To solve this problem, a strategy of stratification is used, where a fictitious Hamiltonian is introduced with a continuous variable λ which slowly switches the Hamiltonian of the system from state 0 to state 1. Using this fictitious Hamiltonian we can generate intermediate states in between the two end points which are close in phase space. The total free energy change is then the sum of free energy changes for each small step in λ. Various formulations of this strategy are available such as free energy perturbation (FEP)[115], finite difference thermodynamic integration (FDTI) [116] and thermodynamic integration (TI)[117, 118].

In the thermodynamic integration method, the free energy change can be written as

$$\Delta A = A(\lambda = 1) - A(\lambda = 0) = \int_0^1 \left(\frac{dA}{d\lambda}\right) d\lambda \tag{80}$$

The derivative term can be written as an ensemble average by substituting the partition function (Q_λ) corresponding to the λ dependent Hamiltonian ($H(r^N, p^N; \lambda)$) and is given as,

$$\begin{aligned}
\frac{dA}{d\lambda} &= -\frac{1}{\beta}\frac{d}{d\lambda}\ln Q_\lambda = -\frac{1}{\beta}\frac{1}{Q_\lambda}\frac{dQ_\lambda}{d\lambda} \\
&= -\frac{1}{\beta}\left[\frac{1}{\frac{1}{N!h^{3N}}\int e^{-\beta H(r^N,p^N;\ \lambda)} dr^N dp^N}\right]\left[\frac{d}{d\lambda}\frac{1}{N!h^{3N}}\int e^{-\beta H(r^N,p^N;\ \lambda)} dr^N dp^N\right] \\
&= \frac{\int \left(\frac{\partial H(r^N,p^N;\ \lambda)}{\partial\lambda}\right) e^{-\beta H(r^N,p^N;\ \lambda)} dr^N dp^N}{\int e^{-\beta H(r^N,p^N;\ \lambda)} dr^N dp^N} \\
&= \left\langle \frac{\partial H(r^N, p^N; \lambda)}{\partial\lambda} \right\rangle_\lambda
\end{aligned} \tag{81}$$

where the ensemble average is over the phase space of a fixed λ. Substituting the expression for the derivative derived in Eq. 81 into Eq. 80 the free energy change is given as,

$$\Delta A_0^1 = \int_0^1 \left\langle \frac{\partial H(r^N, p^N; \lambda)}{\partial\lambda} \right\rangle_\lambda d\lambda \tag{82}$$

Usually for a constant mass system, where the mass of the atoms remain constant, the kinetic energy is independent of λ. In this case the free energy change is only a function of the λ – dependent potential energy. This free energy change is given as,

$$\Delta A_0^1 = \int_0^1 \left\langle \frac{\partial V(r^N; \lambda)}{\partial\lambda} \right\rangle_\lambda d\lambda \tag{83}$$

where $V(r^N; \lambda)$ is the λ- and position- dependent potential energy function. The derivative can be expanded using a finite difference scheme:

$$\begin{aligned}\Delta A_0^1 &= \int_0^1 \left\langle \frac{\partial V(r^N;\,\lambda)}{\partial \lambda} \right\rangle_\lambda d\lambda \\ &= \sum_{i=0}^{n-1} w_i \left\langle \frac{\partial V(r^N;\,\lambda)}{\partial \lambda} \right\rangle_{\lambda_i} \\ &= \sum_{i=0}^{n-1} w_i \left\langle \frac{V(r^N;\,\lambda_i+\delta) - V(r^N;\,\lambda_i)}{\delta} \right\rangle_{\lambda_i}\end{aligned} \tag{84}$$

where λ is discretized to n intermediate points $\lambda_i \epsilon [0, \lambda_1, \ldots, \lambda_{n-2}, 1]$ in the range $(0, 1)$ and δ is the small step used to compute the derivative. Note that the free energy to go from state 1 to state 0 is related to the reverse process as

$$\Delta A_0^1 = -\Delta A_1^0 \tag{85}$$

where ΔA_1^0 can be calculated as,

$$\Delta A_1^0 = \sum_{i=0}^{n-1} w_i \left\langle \frac{V(r^N;\,\lambda_i-\delta) - V(r^N;\,\lambda_i)}{\delta} \right\rangle_{\lambda_i} \tag{86}$$

where the discretized points $\lambda_i \,\epsilon\, [1, \lambda_1, \ldots, \lambda_{n-2}, 0]$.

The λ dependence of the potential can be achieved using a direct interpolation in the case of Coulomb and van der Waals interactions. In practice, a slight modification to the potential is required to avoid charged particles approaching arbitrarily close which will result in infinite energy [118, 119, 120].

The modified Lennard-Jones potentials for the van der Waals interaction as a function of λ is given as,

$$U(\lambda) = \frac{\lambda^2 4\epsilon_{lj}}{\left[\alpha_{LJ}(1-\lambda)^2 + \left(\frac{r}{\sigma}\right)^6\right]^2} - \frac{\lambda^2 4\epsilon_{lj}}{\alpha_{LJ}(1-\lambda)^2 + \left(\frac{r}{\sigma}\right)^6} \tag{87}$$

where ϵ_{lj} is the depth of the interaction well, σ is the van der Waals radius and α_{LJ} is the soft core parameter which prevents the Coulomb interaction from diverging at small distances. This potential is shown in Fig. 2.8(a) with varying λ. Ultimately when $\lambda = 1$ the usual Lennard-Jones potential is recovered.

The effect of varying λ on a system of graphene interacting with cyclopentanone molecules is shown in Fig. 2.8(b–e). When $\lambda = 0$ the atoms near in the graphene

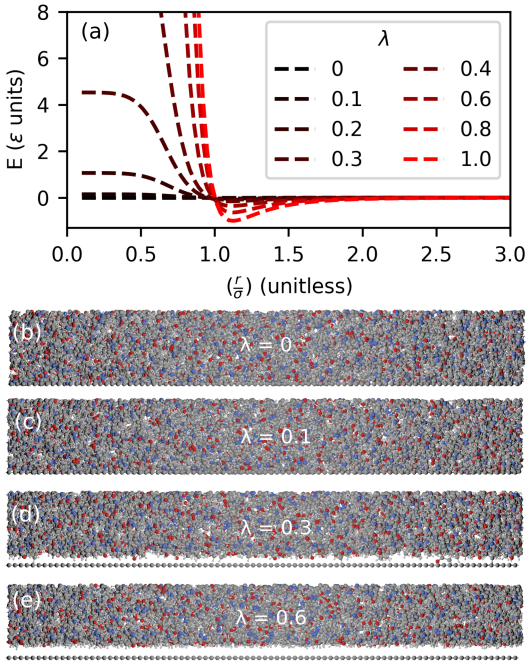

Figure 2.8: (a) Soft core potential as a function of the parameter λ which controls the strength of interaction between the atoms of graphene layers and atoms in the molecules with the soft core radius of 0.5. The effect of potential is shown in (b – e). When the parameter $\lambda = 0$ the atoms in graphene and molecules do not interact and the can be arbitrarily close to each other as seen in (b). On increasing the parameter λ to 0.3 the exclusion region near the graphene layer where the molecule density is very low as shown in (c) and is a result of the energy penalty when inter atomic distance is small. This energy penalty increases rapidly on further increasing λ to 0.6 as shown in (d) with no molecules present in the exclusion region. Finally, when $\lambda = 1$ the usual Lennard-Jones potential is recovered.

layer are effectively not present so they have no effect on the atoms around them. This can also be seen from the snapshots shown in Fig. 2.8(e). On increasing λ the molecules near the graphene surface move away as shown in Fig. 2.8(c–d). This un-physical switching where the atoms spontaneously appear is also called "alchemical analysis".

2.11 Free energy calculations: methods

The change in free energy indicates the thermodynamic favourability of a process such as solvation and conversion reactions. The calculated free energy is known as the Helmholtz free energy when the volume of the system is kept fixed throughout the process. If the volume changes during the process, the calculated energy is the Gibbs free energy. In the context of molecular solvents interacting with graphene,

the free energy can be calculated using the method discussed in section 2.8 and in section 2.10.

The free energy calculated using density functional theory extended to include the effects of a solvent as a continuous dielectric is described in section 2.8. This takes into account the change in volume during the solvation process. Hence the solvation energies calculated using this formalism are the Gibbs free energies of solvation. For this method, model parameters for a particular solvent have to be determined by fitting the solvation energies for a variety of solutes immersed in that solvent. However general trends such as electrostatic interaction dependence and cavity formation dependence can be studied using this method.

To determine the favourability of the formation of solvation shells for a particular solvent, we can use the method described in section 2.10. This method explicitly include individual molecules and calculated energies indicate the favourability of formation of the solvation shells around a solute. These calculations do not take into account the change in volume of the system due to the solvation process. Hence the Helmholtz free energy is calculated for the formation of the solvation shells.

2.12 Diffusion coefficient of confined particles

In this section we describe the diffusion of particles confined in an external potential. This external potential could be due to the presence of a surface, interface or could be artificially applied. For a subset of M particles present in this confining potential from a total of N particles present in the region, where $M << N$, the motion of the particles is governed by the Langevin equation. This is given as,

$$m\ddot{r} = -\gamma\dot{r} + F(r) + \sigma\eta(t) \tag{88}$$

where m is the mass, $\dot{r}$ is the velocity, $\ddot{r}$ is the acceleration, γ is the friction coefficient, $F(r)$ is the external force, σ is the magnitude of fluctuations and $\eta(t)$ is the noise term. The term $\gamma\dot{r}$ is the drag term which indicates a penalty for acceleration [121]. In the strong friction limit $|\gamma\dot{r}| \gg |m\ddot{r}|$ so the drag dominates over the acceleration. The Langevin equation is then given as,

$$\gamma\dot{r} = F(r) + \sigma\eta(t) \tag{89}$$

Due to randomized nature of Eq. 89 via the noise term $\eta(t)$, simulating a

specific trajectory from all the possible trajectories may not be desirable. Instead, the probability distribution of evolution is required. The Fokker-Plank equation describes this evolution. The Fokker-Plank equation corresponding to Eq. 89 is given as,

$$\partial_t p(r, t|r_0, t_0) = \left(\frac{\nabla^2 \sigma^2}{2\gamma^2} - \nabla \cdot \frac{F(r)}{\gamma} \right) p(r, t|r_0, t_0) \tag{90}$$

where $p(r, t|r_0, t_0)$ is the conditional probability that the particle is at position r at time t given it was at position r_0 at time t_0 and ∂_t is the derivative of the probability with respect to time. The diffusion coefficient is defined as

$$D = \frac{\sigma^2}{2\gamma} \rightarrow D(r) \tag{91}$$

and is position dependent. If the force can be written as

$$F(r) = -\nabla U(r) \tag{92}$$

where $U(r)$ is a scalar potential, then the Boltzmann distribution $(e^{-\beta U(r)})$ is a stationary solution, i.e.

$$\left(\nabla \cdot \nabla D - \nabla \cdot \frac{F(r)}{\gamma(r)} \right) \exp^{-\beta U(r)} = 0 \tag{93}$$

here, we have also assumed that the friction term is position dependent. Substituting this definition of the diffusion coefficient in Eq. 90 results in the Smoluchowski equation [122] given as,

$$\partial_t p(r, t|r_0, t_0) = \nabla \cdot D(\nabla - \beta F(r)) p(r, t|r_0, t_0) \tag{94}$$

Note that the famous Einstein equation is a special case of Eq. 94 when the external force $F(r) = 0$ [123].

For slab–like 2D geometries, the external force is perpendicular to the surface, i.e.,

$$F(r) \rightarrow F(z) = \nabla W(z) \tag{95}$$

where $W(z)$ is the potential due to the surface in the direction perpendicular to it. Additionally, assuming that the diffusion tensor is diagonal

$$\begin{bmatrix} D_{xx} & 0 & 0 \\ 0 & D_{yy} & 0 \\ 0 & 0 & D_{zz} \end{bmatrix} \tag{96}$$

where D_{xx}, D_{yy} and D_{zz} are the diffusion coefficients in the x, y and z direction, the probabilities can be written as,

$$p(r, t|r_0, t_0) = p(z, t|z_0, t_0)p(x, t|x_0, t_0)p(y, t|y_0, t_0) \tag{97}$$

where the conditional probability is in the corresponding direction. Using Eq. 96 and Eq. 97, and the Smoluchowski equation given in Eq. 94, the diffusion coefficient parallel to a surface can be written as

$$\partial_t p(x, t|x_0, t_0) = D_{xx}\partial_x^2 p(r, t|r_0, t_0) \tag{98}$$

In the direction perpendicular to the surface it can be written as

$$\partial_t p(z, t|z_0, t_0) = D_{zz}\partial_z[\partial_z + \beta(\partial_z W(z))]p(z, t|z_0, t_0) \tag{99}$$

It is convenient to relate this diffusion relation to quantities that can be calculated using molecular dynamics simulations. For this, consider the mean square displacement ($\langle \Delta x(t)^2 \rangle_{\{a,b\}}$) of particles in direction parallel to the surface in a region $a < z < b$,

$$\left\langle \Delta x(t)^2 \right\rangle_{\{a,b\}} = \int_{V_{a,b}} d^3 r \int_{V_{a,b}} d^3 r_0 p(r, t|r_0, t_0)p(r_0)(x - x_0)^2 \tag{100}$$

where the $V_{a,b}$ indicates the region $a < z < b$, $p(r_0)$ is the probability that the particle is at position r_0 at time t_0 and x is the x component of the position vector. Using the Smoluchowski equation the mean square displacement can be can be recast as,

$$\left\langle \Delta x(t)^2 \right\rangle_{\{a,b\}} = 2P(t)D_{xx}t \tag{101}$$

where $P(t)$ is the survival probability which indicates the probability that a particle remains in the region $a < z < b$ for time window t. The diffusion coefficient is then,

$$D_{xx} = \lim_{t\to\infty} \frac{\langle \Delta x(t)^2 \rangle_{\{a,b\}}}{2tP(t)} \tag{102}$$

The quantities on the right hand side can be calculated using standard molecular dynamics simulations [124, 125]. Rewriting the averages in terms of the molecular dynamics trajectories, the mean square displacement is given as,

$$\left\langle \Delta x(\tau)^2 \right\rangle_{\{a,b\}} = \frac{1}{T} \sum_{t=1}^{T} \frac{1}{N(t)} \sum_{i \epsilon \zeta(t,t+\tau)} \left(x_i(t+\tau) - x_i(t)\right)^2 \tag{103}$$

where $\zeta(t, t+\tau)$ is the set of all particles that stay in the region $a < z < b$ from time t to $t+\tau$, $N(t)$ is the number of particles in the region $a < z < b$ at time t and T is the number of time steps to average. The survival probablity can be calculated as,

$$P(\tau) = \frac{1}{T} \sum_{t}^{T} \frac{N(t, t+\tau)}{N(t)} \tag{104}$$

where $N(t, t+\tau)$ is the number of particles that stay within the region $a < z < b$ between times t and $t+\tau$. The parameters in the calculation of diffusion coefficient are τ, T and the definition of the region between a and b.

CHAPTER

3

EXFOLIATION OF GRAPHITE AND MOS_2

3.1 Introduction

Liquid phase exfoliation of graphite is one of the most promising and inexpensive methods to produce graphene on the scale required to be industrially viable [29, 126, 127, 128]. It uses an energy input, typically sonication [27, 129, 130] or high-shear mixing[131, 132], to mechanically exfoliate [133] layered solids into mono-layer or few-layer two-dimensional (2D) nanosheets in a solvent. The method is not restricted to graphite, and has been successfully applied to a wide range of other layered materials, including MoS_2 [31], black phosphorus [134], antimonene [135] and hexagonal boron nitride [136]. The dispersions produced in this way can then be used for a variety of applications such as inks for printed flexible electronics [137, 138], fire resistant coatings [139] and printed capacitors [140].

The effectiveness of the method is measured as the concentration of monolayer to few layer slabs that remain suspended in the solvent. This concentration is measured directly as the mass of suspended flakes or using optical experiments

which measure the light absorbed by the layers in the solvent [141]. Unfortunately, yields can be very low, both in terms of the number of monolayers obtained and in the amount of unexfoliated material that remains. The outcome depends on the choice of solvent, and finding the best solvent for a particular material is an important processing step. For example, concentrations as high as 2 mg/ml can be achieved in the case of of NMP with an yield of 10% [34, 142], whereas some solvents such as hydrocarbon chains barely exfoliate graphene layers. NMP is also an effective solvent for MoS_2, resulting in concentrations as high as 7.5 mg/ml and yields as large as 40% [31].

As well as aiming to maximize monolayer yield, there are other restrictions on the choice of solvent. For example, many of the better solvents for graphite exfoliation, including NMP, DMA and DMF, are toxic and face restrictions by the European Chemicals Agency rendering them unsustainable for future industrial use [143]. It is therefore critical to devise screening tools to identify non-toxic, low-boiling point solvents which do not compromise on performance [144]. Ideally these screening tools would be generalizable to other two-dimensional materials beyond graphene.

Exactly how the nature of a solvent affects the resulting yield is not clearly understood. The liquid phase exfoliation process can be divided into two steps: the initial separation of the layers and the subsequent stabilization to prevent reaggregation. As stated previously, the first step involves the separation of the layers via the application of an external force to overcome the interlayer interactions. These forces can originate from sonication, shear mixing or wet ball milling. Next, the separated layers are stabilized via various solvent-layer interactions and remain separated, resulting in a dispersion of monolayers and/or few-layer graphene sheets in the solvent.

It is generally accepted that the solvent plays a minor role in the first step – with extensive exfoliation occurring in most solvents due to the energy introduced by sonication or shear mixing [145, 146, 147, 148]. Despite this, the subsequent dispersion is not always stable with extensive reaggregation and sedimentation found in some cases. The fact that the solvent properties optimum for the initial exfoliation step do not necessarily align with those required to maintain a stable dispersion is most evident by considering the results of solvent exchange experiments [43, 44, 45]. Here, the separation and dispersion steps use different solvents. For example Zang et. al. first exfoliated graphite in NMP, then exchanged NMP with ethanol. This results in a higher

concentration of up to 0.04 mg/ml of graphene in the dispersion compared to using either NMP (4.7 ± 1.9 μg/ml) or ethanol (1.6 ± 0.7 μg/ml) alone [43].

As the concentration of the graphene layers is directly dependent on the number of layers that are initially separated, it is important to compare experimental concentrations where the procedure used for the production of the suspended graphene layers is identical. Parameters such as sonication time, centrifugation speed and centrifugation time have a direct impact on number of exfoliated layers. Optimizing these parameters for a particular solvent can result in concentrations which are order of magnitudes higher than those found initially. For example, the concentration of graphene in NMP can be increased from 4.7 ± 1.9 μg/ml [43] to as high as 2 mg/ml [34] by optimizing the sonication times.

One of the first experimental attempts to screen for effective solvents for graphite exfoliation found that the concentration of dispersed graphene was maximized for those solvents with a surface energy or tension similar to that of graphite [149]. This follows the traditional surface wettability argument. For a liquid to completely cover (wet) a surface by forming a thin film over it, the surface tensions should match. Even a slight mismatch can result in solvent beading on the surface. Full surface coverage (wetting) is desired as the presence of these molecules can prevent reaggregation. Although this method has had some successes, there are also examples where it breaks down: Cyclopentanone and 1-Dodecyl-2-pyrrolidinone (N12P) have very similar surface tensions at 33.31 mJ/m^2 and 34.5 mJ/m^2, respectively, yet cyclopentanone is a very good solvent resulting in a graphene concentration of 8.5 μg/ml whereas N12P results in a graphene concentration of only 2.1 μg/ml [145].

Hansen solubility parameters, characterized by three intermolecular interactions, namely hydrogen bonding, polar and nonpolar (dispersive), were used successfully to predict the solubility of polymers in solvents, and as a result were adapted to apply to small molecules and nanosheets [150]. The enthalpy of mixing will be minimized when solvent and solute have similar values of all three Hansen solubility parameters. These solvent parameters are based on the idea that solvents with similar intermolecular energies are intersoluble. The Hildebrand solubility parameters of a particular solvent are are determined based on the enthalpy of vaporization and can be interpreted as the energy difference between infinitely separated solvent molecules and those same molecules in a liquid. These parameters are given in column 5 (δ_T) of

Table 3.1. The Hansen solubility parameters separate the intermolecular interactions into a polar component (δ_P) due to molecular dipoles, a dispersion component (δ_D) due to the van der Waals interaction and a hydrogen bonding component (δ_H). These parameters are listed in Table 3.1. These components are related to the Hildebrand solubility parameters as,

$$\delta_T^2 = \delta_P^2 + \delta_D^2 + \delta_H^2 \tag{1}$$

This separation is empirical (based on experimental measurements). To determine the optimal solvent for a given solute, the distance (R_α) in 3D space given by

$$R_\alpha = \sqrt{(\delta_P^{solute} - \delta_P^{solvent})^2 + (\delta_D^{solute} - \delta_D^{solvent})^2 + (\delta_H^{solute} - \delta_H^{solvent})^2} \tag{2}$$

is minimized. In order to determine the solubility parameters for graphene, Hernandez et al. exfoliated graphene in 40 different solvent molecules using the same exfoliation parameters to enable a direct comparison between them [145]. The list of these 40 solvents along with the corresponding graphene concentrations are listed in Table 3.1 in decreasing order of the resulting concentration of graphene in the solution (C_G). Using Eq. 2 and an assumption that the distance R_α is minimized for the most favorable solvent, Hernandez et. al. determined the optimal solvent parameters for graphene using the data shown in Table. 3.1. In this way, graphene was found to have Hansen dispersion, hydrogen bonding and polar solubility parameters of $\delta_D = 18$ $MPa^{1/2}$, $\delta_P = 9.3$ $MPa^{1/2}$, and $\delta_H = 7.7$ $MPa^{1/2}$, respectively.

From the experimental data we can see that pristine graphene – which is non-polar in nature – is stabilized in slightly polar solvents. In fact, non-polar solvents such as hexane, heptane and toluene are ineffective, as are highly polar solvents such as water or formamide. From this it is clear that the simplified rule-of-thumb for solvation – that polar solvents dissolve polar solutes and non-polar solvents dissolve non-polar solutes – is no longer applicable.

The effectiveness of LPE for other monolayers such as WS_2, MoS_2 and h-BN is also dependent critically on the choice of solvent [28, 32] with no obvious similarities in between them. From a list of 20 solvents, the best solvent for WS_2 is found to be DMSO while it only the seventh best solvent for MoS_2 and eleventh for h-BN. Instead the best solvent for MoS_2 is NVP. This is the second best solvent for WS_2,

Solvent	δ_D $(MPa^{\frac{1}{2}})$	δ_P $(MPa^{\frac{1}{2}})$	δ_H $(MPa^{\frac{1}{2}})$	δ_T $(MPa^{\frac{1}{2}})$	C_G $(\mu g/ml)$	ΔC_G $(\mu g/ml)$
Graphene	18	9.3	7.7	-	-	-
Cyclopentanone (CPO)	17.9	11.9	5.2	22.1	8.5	1.2
Cyclohexanone	17.8	8.4	5.1	20.3	7.3	1.3
N-formyl piperidine (NFP)	18.7	10.6	7.8	22.9	7.2	1
Vinyl pyrrolidone (NVP)	16.4	9.3	5.9	19.8	5.5	1.5
1,3-Dimethyl-2-imidazolidinone (DMEU)	18	10.5	9.7	23	5.4	1.3
Bromobenzene	19.2	5.5	4.1	20.4	5.1	0
Benzonitrile	18.8	12	3.3	22.5	4.8	0.6
N-methyl-pyrrolidone (NMP)	18	12.3	7.2	23	4.7	1.9
Benzyl Benzoate	20	5.1	5.2	21.3	4.7	1.9
N,N'-Dimethylpropylene urea (DMPU)	17.8	9.5	9.3	22.2	4.6	1.3
γ - Butrylactone (GBL)	18	16.6	7.4	25.6	4.1	1.1
Dimethylformamide (DMF)	17.4	13.7	11.3	24.9	4.1	1.4
N-ethyl-pyrrolidone (NEP)	18	12	7	22.7	4	0.7
Dimethylacetamide (DMA)	16.8	11.5	9.4	22.4	3.9	1.5
Cyclohexylpyrrolidone (CHP)	18.2	6.8	6.5	20.5	3.7	1
DMSO	18.4	16.4	10.2	26.7	3.7	1.5
Dibenzyl ether	19.6	3.4	5.2	20.6	3.5	0.6
Chloroform	17.8	3.1	5.7	18.9	3.4	0.7
Iso-propylalcohol (IPA)	15.8	6.1	16.4	23.6	3.1	1
Cholobenzene	19	4.3	2	19.6	2.9	0.5
1-Octyl-2-pyrrolidone (N8P)	17.4	6.2	4.8	19.1	2.8	1
1-3 dioxolane	18.1	6.6	9.3	21.4	2.8	1.4
Ethyl acetate	15.8	5.3	7.2	18.2	2.6	1.2
Quinoline	20.5	5.6	5.7	22	2.6	0.6
Benzaldehyde	19.4	7.4	5.3	21.4	2.5	1.5
Ethanolamine	17.5	6.8	18	26	2.5	0.4
Diethyl phthalate	17.6	9.6	4.5	20.5	2.2	1.9
N-Dodecyl-2-pyrrolidone (N12P)	17.5	4.1	3.2	18.3	2.1	1.1

Pyridine	19	8.8	5.9	21.8	2	1.7
Dimethyl phthalate	18.6	10.8	4.9	22.1	1.8	0.4
Formamide	17.2	26.2	19	36.7	1.7	0
Ethanol	15.8	8.8	19.4	26.5	1.6	0.7
Vinyl acetate	16	7.2	5.9	18.5	1.5	0.7
Acetone	15.5	10.4	7	19.9	1.2	0.4
Water	15.5	16	42.3	47.8	1.1	0.4
Ethylene glycol	17	11	26	33	1	0.8
Toluene	18	1.4	2	18.2	0.8	0.4
Heptane	15.3	0	0	15.3	0.3	0.4
Hexane	14.9	0	0	14.9	0.2	0.1
Pentane	14.5	0	0	14.5	0.16	0.05

Table 3.1: The table describes the polar component (δ_P), dispersion component (δ_D), and hydrogen bonding component (δ_H) of Hansen solubility parameters, δ_T the Hildebrand solubility parameter, the experimental dispersed concentration of graphene (C_G) and the uncertainty (ΔC_G) reported by Hernandez. et. al.[145]

but only sixth best for h-BN. Although higher concentrations of monolayers can be achieved by optimizing the exfoliation parameters, the solvent order is generally maintained, i.e., the previously designated poor solvents will in general continue to have lower yields than the others.

Searching for new solvents with solubility parameters close to those determined for graphene led to the prediction and confirmation of cyclopentanone and cyclohexanone as very good solvents of graphene. However, here again, there are some examples where this screening technique fails: dimethyl phthalate has very similar Hansen parameters to cyclopentanone, yet is a poor graphene solvent (see Table 3.1). This suggests that matching solubility parameters is quite a blunt tool, missing some information about the stabilization mechanism [151]. In particular, the approach makes the approximation that thermodynamic effects alone determine the nanosheet concentration. This will not be the case, with sedimentation and other effects also playing a role. Nonetheless, semi-empirical methods provide a useful starting point for solvent screening.

The failure of these empirical solubility models suggests that considering only macroscopic solution thermodynamics is not sufficient to find good solvents [152]. Instead, explicit structural and electronic interactions between the solvent molecules and the solute may play an important role. It has been suggested

that solvent molecules can act as a 'wedge', prising the layers apart at the edges, thereby improving the efficiency of subsequent exfoliation attempts [48, 49]. Mutual interactions may also result in the confinement of the solvent molecules at the surface or in interlayer spaces, resulting in changes to the entropic contribution to exfoliation [153, 154, 155, 156, 157, 158].

In this chapter we systematically study the origin of the solvent dependence of the process of liquid phase exfoliation. In Section 3.2 we study the nature of interaction between individual solvent molecules with graphene and MoS_2. We find that the nature of interaction is van der Waals with negligible charge transferred between them. In Section 3.3 we study the collective behavior of multiple molecules near the surface of graphene monolayer, and show that kinetic effects play a major role in the stabilization of the graphene sheets in a solvent, rather than thermodynamic effects alone.

3.2 Adsorption of common solvent molecules on graphene and MoS_2 from first-principles

It is generally assumed that solvent molecules interact only weakly with the layered materials and so their effects can be neglected. However, this is not always the case and given the atomic thickness and large surface area of 2D layers, there may be unintended effects on the structural and electronic properties of the layer. For example, Choi et al. found that common solvents can transfer sufficient charge to transition metal dichalcogenide layers to cause measurable changes in their electrical and optical properties [159].

Very little is known about the nature of the interaction between solvent molecules and 2D layered materials on the atomic level. In this work, we use density functional theory to systematically determine the ground state adsorption configuration of a variety of solvent molecules on two of the most widely studied 2D materials, namely graphene and hexagonal MoS_2. We choose six representative solvents from the polar protic (2-propanol), polar aprotic (bendaldehyde, cyclopentanone and N-Methyl-2-pyrrolidone (NMP)) and non-polar (toluene and chloroform) solvent families. These are shown in Fig. 3.1(a). Our aim is to determine whether observed differences in the ability of particular solvents to exfoliate layered materials can be attributed to differences in how individual molecules interact with the surface of that material. We determine their adsorption configuration and binding energy and show that these molecules are physisorbed on the surface with little charge transfer between the two. Despite this, a significant charge rearrangement occurs at the interface due to an induced dipole interaction.

3.2.1 Computational Methods

3.2.1.1 Density Functional Theory

Density functional theory (DFT) calculations are performed using the projected augmented wave (PAW) method as implemented the VASP code [160, 161, 162, 163]. The Perdew-Burke-Ernzerhof (PBE-PAW) potentials [59, 63] provided with the package are used. The optimized optB86b-vdW functional [77, 78, 82, 164, 165] is used to approximate the exchange-correlation functional and to self-consistently account for van der Waals (vdW) interactions. Here, the exchange-correlation energy (E_{xc}) is given by $E_{xc} = E_x^{GGA} + E_c^{LDA} + E_c^{NL}$, where E_x^{GGA} is the exchange energy calculated using

an optimized version of the B86b exchange functional[166], E_c^{LDA} is the correlation energy calculated using the local density approximation (LDA) and E_c^{NL} is the non-local contribution to the correlation energy. This latter term encompasses the long-range interactions. The optB86b-vdW functional was previously shown to provide accurate binding energies for both gas phase clusters and bulk solids and for molecular adsorption on transition metal surfaces[167].

In order to model the adsorption of isolated molecules, a 3×5 orthorhombic unit cell of both graphene and MoS_2 is used, as shown in Fig. 3.1(b) and (c). As a result, there is a minimum distance of at least 10 Å between periodic images of the molecules. Furthermore, a vacuum layer of at least 15 Å is included in the direction normal to the surface to ensure no spurious interactions between repeating layers, and the dipole correction is applied.

The graphene (MoS_2) Brillouin zone is sampled with a $5 \times 5 \times 1$ ($3 \times 3 \times 1$) Monkhorst-Pack mesh [168] to carry out structural relaxations to a force tolerance of 0.02 eV/Å. All atoms in the unit cell are allowed to move, including those of the substrate. The electronic properties are then calculated using a k-point sampling of $11 \times 11 \times 1$. In all cases, a plane wave cutoff of 500 eV is used to converge the basis set.

The determination of charge transfer depends sensitively on how the charge density is assigned to each atom. Here, we use both the Density Derived Electrostatic and Chemical (DDEC) net atomic charges [169] scheme as implemented in the chargemol program and the Bader partitioning scheme [170, 171].

3.2.1.2 Mapping the Configuration Space

For multi-atom adsorbents, such as the molecules considered here, there is a large phase space of possible adsorption configurations. In order to find the lowest energy binding site, we follow a process similar to Åkesson et al. [172], extended to include molecular rotations. Note that while the symmetry of the substrate is taken into account when creating the initial adsorption configurations, nothing is assumed about the molecular symmetry.

In order to calculate the correct potential energy surface, the atomic coordinates of the molecule at a fixed in-plane position should be allowed to relax. However, this is computationally prohibitive. Instead, we fix the center of

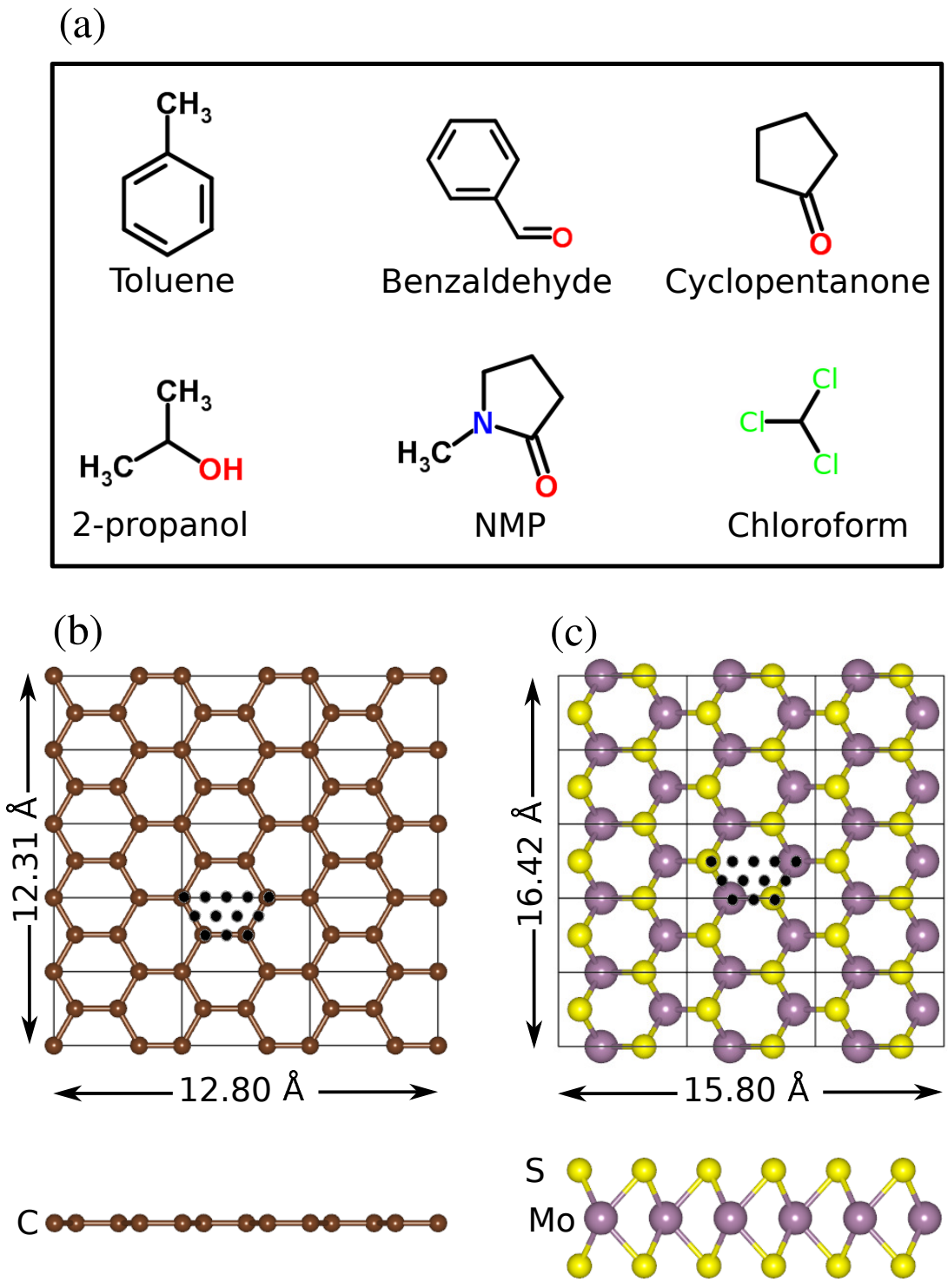

Figure 3.1: (a) Geometry of the six solvent molecules considered in this study. Top and side view of the (b) graphene and (c) MoS_2 supercell used in this work. The 12 irreducible adsorption points are shown as black dots on the lattice.

mass of the molecule at a constant height above the surface for all considered molecular rotations.

The following work-flow is used to determine the ground state binding configuration: The individual components, i.e., the molecule and the 2D layered material, are first relaxed to determine their isolated structures. A uniform grid is then defined at a typical binding height (3.5 Å) above the surface of each material, as shown in Fig. 3.1(b) and (c). The binding height of the molecules is defined as the distance between the center of mass of the molecule and the surface of the 2D layer. The grid spacing is defined as $d/2$ where d is the C–C or Mo–S bond length, projected in-plane. The center of mass of each molecule is placed at each grid point.

Due to the low adsorption concentration considered here, each molecule will minimize its total energy by maximising its total area of overlap with the surface, i.e., planar molecules adsorb flat against the substrate [173, 174]. With this restriction, molecular rotations, in steps of $5°$, around an axis normal to the basal plane of the substrate are considered. Out-of-plane rotations are also included. Planar molecules such as benzaldehyde have only one indistinguishable out-of-plane rotation. NMP, cyclopentanone and toluene are non-planar with two possible rotational configurations obtained by a $180°$ rotation out-of-plane. Chloroform has four possible rotational configurations: two in which the H–C bond is perpendicular to the plane of graphene, and another two in which the H–C bond is at $60°$ to the plane. Finally, 2-propanol also has four possible rotational configurations: two orientations in which the C–O bond is perpendicular to the surface and another two in which it is parallel. A structure matching algorithm, as implemented in pymatgen [175], then reduces the total number of configurations.

The total energy of each of these configurations, without relaxation, is calculated for a fixed binding height. The entire procedure is then repeated for a sub-set of these configurations at a lower height in steps of 0.25 Å until the lowest energy adsorption height is found. At this stage, a structural optimization of all structures at local minima with total energies within 0.05 eV of the global minimum is performed. During the structural optimization, the coordinates of all atoms in the unit cell are allowed to move. The configuratation with the lowest total energy after this structural optimization is the ground state configuration.

3.2.2 Results and Discussion

3.2.2.1 Ground State Configurations

The solvent molecules are found to adsorb at an average binding height of 3.35 Å from the surface of both graphene and MoS_2. The binding heights are shown in Fig. 3.2. The smallest binding height is found for benzaldehyde on graphene (3.00 Å), while the largest binding height of 3.56 Å is found for 2-propanol on graphene. These heights are consistent with physisorption [172, 174, 176].

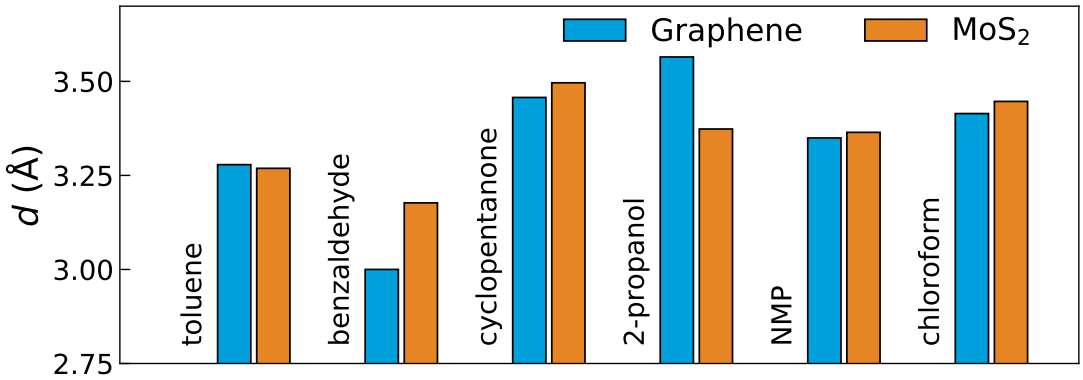

Figure 3.2: The binding height of center of mass of the molecule from the surface of the substrate.

The potential energy surface (PES) for these molecules is four-dimensional, involving the in-plane translational coordinates as well as both in-plane and out-of-plane rotations. An example is shown in the Section 3.2.2.2 for a fixed rotational angle. In the following we present only the final, geometrically optimized, minimum energy configurations for each of the solvent molecules. These are shown in Fig. 3.3.

The adsorption positions of each of the six solvent molecules adsorbed on graphene are shown in the top panel of Fig. 3.3. Molecules which contain a six-member ring are found to adsorb such that every alternate atom of the carbon ring is on top of a carbon atom in the graphene sheet, similar to the AB-stacking of two adjacent carbon layers in a graphite crystal [177]. This is particularly evident for toluene and benzaldehyde where small deviations from the perfect AB-type stacking are dictated by the functional group attached to the ring. The methyl group of toluene is adsorbed at a 'top' position, i.e., on top of a graphene carbon atom, with the edge of the methyl group tripod facing the graphene lattice, in agreement with Borck et al.[176] In contrast, the aldehyde (CHO) functional group of benzaldehyde is adsorbed at a hollow position. This

is due to the different hybridizations of the carbon atoms in the two functional groups – the carbon atom in the methyl group is sp^3 hybridized, whereas it is sp^2 hybridized in the CHO group. As the aldehyde oxygen atom has a partial negative charge, it prefers to adsorb close to a graphene bridge site.

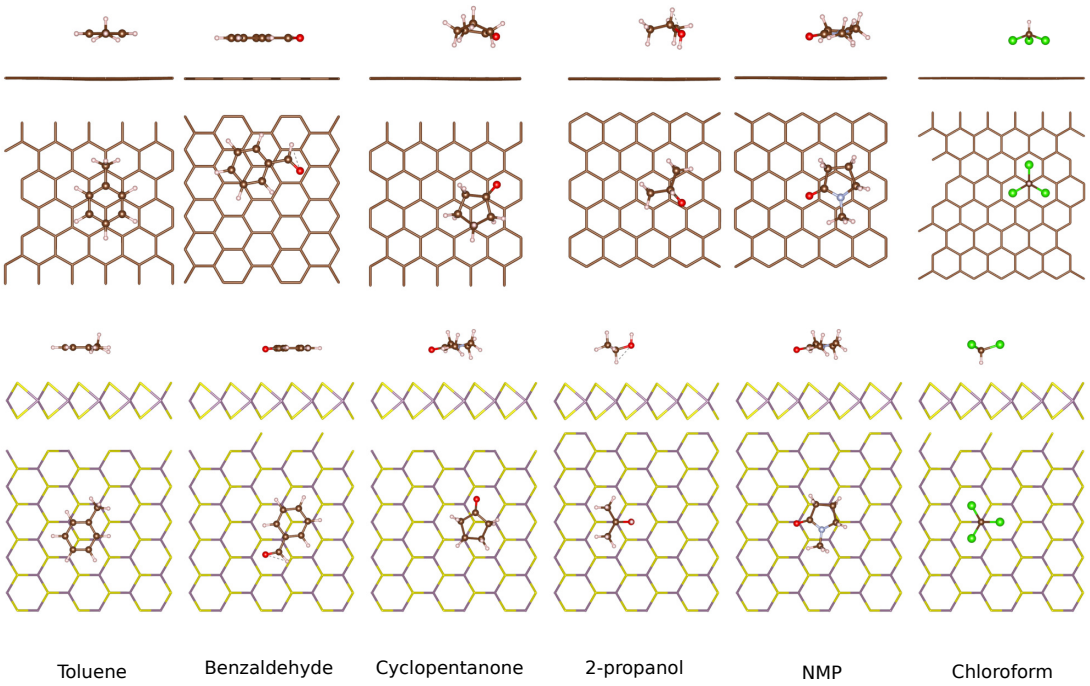

Figure 3.3: Top (bottom) panel: Side and top view of the lowest energy binding site of the solvent molecule on graphene (MoS_2).

The carbon atoms in cyclopentanone are sp^3 hybridized with the exception of that bonded to oxygen, which is sp^2 hybridized. The three carbon atoms bonded to hydrogen atoms which point towards the graphene layer are located above hollow sites. The carbon atom bonded to a hydrogen atom which points away from the graphene layer is adsorbed above a carbon top site. The remaining electropositive carbon atom is adsorbed on a graphene top site, while the electronegative oxygen atom is located close to a graphene bridge site. Similarly, the oxygen atom in 2-propanol adsorbs close to a bridge site and all sp^3 hybridized carbon atoms avoid the top sites. It maximizes its surface contact area by adsorbing such that the C–O bond is approximately parallel to the graphene layer.

For the case of NMP, the electronegative oxygen and nitrogen atoms dictate the orientation of adsorption by adsorbing close to bridge sites. Fixing the adsorption position of these two atoms determines the orientation of the rest of the molecule. Finally, for the case of chloroform, each of the chlorine atoms adsorbs close to a hollow site, with the hydrogen pointing away from the layer in a so-called “H-up”

configuration. Note that this is a different adsorption configuration to that found by Åkesson et al. due to the more restrictive configuration space considered in that work [172]. In all cases the deformation in the graphene substrate is less than 0.1 Å.

The geometrically optimized configurations of the molecules adsorbed on MoS_2 are shown in the bottom panel of Fig. 3.3. In all cases, molecules with hydrogen atoms which point towards the MoS_2 surface prefer to adsorb such that they are located in the hollow formed by the sulfur atoms, i.e., directly on top of the metal atoms. For benzaldehyde and toluene, the carbon ring prefers to have alternate carbon atoms above the metal atoms with the center of the ring directly above a sulfur atom. Similarly, for cyclopentanone, the center of the carbon ring prefers to adsorb directly above a sulfur atom with the carbon atoms located either directly on top of the molybdenum atoms or in the hollow of the substrate hexagon. 2-propanol occupies the valley created by the sulfur atoms, with the functionalized carbon atom located on top of the metal atom. Note that this is a 180° out-of-plane rotation with respect to the orientation of the same molecule on graphene. For the case of NMP, the electronegative oxygen atom is adsorbed on top of the metal atom with the orientation of the rest of the molecule dictated by the hydrogen atoms which point towards the surface.

Finally, the hydrogen atom of chloroform also prefers to adsorb in the valley created by the sulfur atoms, directly above the metal atom, so that the molecule is in a "H-down" configuration. This is in contrast to its binding configuration on graphene where it adsorbs with the hydrogen atom pointing away from the surface, i.e. "H-up". In all cases the deformation of MoS_2 substrate after solvent adsorption is negligible.

3.2.2.2 Potential energy surface for chloroform

In the following, we show the PES for chloroform adsorbed on both graphene and MoS_2 at a particular rotational angle. This molecule and angle is chosen such due to its small size, which makes demonstration of the concepts easier. The inferences drawn from this PES are transferable to all the other molecules and orientation. The ground-state adsorption configuration of this molecule is rotated by 180° out-of-plane on these two surfaces. The PES for a specific rotational angle can illustrate the physical mechanism behind the differing adsorption configurations. In this case, the in-plane rotational angle is fixed at that found for the ground state configuration, as shown in Fig. 3.3.

The PES for chloroform adsorbed in a "H-down" configuration on graphene at a constant height of 3.5 Å is shown in Fig. 3.4(a). Recall that the black dots in these figures corresponds to the adsorption position of the center of mass (COM) of the molecule. When the H atom is adsorbed directly above a carbon atom, the short distance between the two atoms results in a large $p_z - s$ orbital repulsion and hence a maximum in the global energy. In contrast, when the H atom is adsorbed directly above the hollow site, the distance between the H atom and the carbon atoms is large, resulting in a small $p_z - s$ orbital repulsion and thus a local minimum in the total energy.

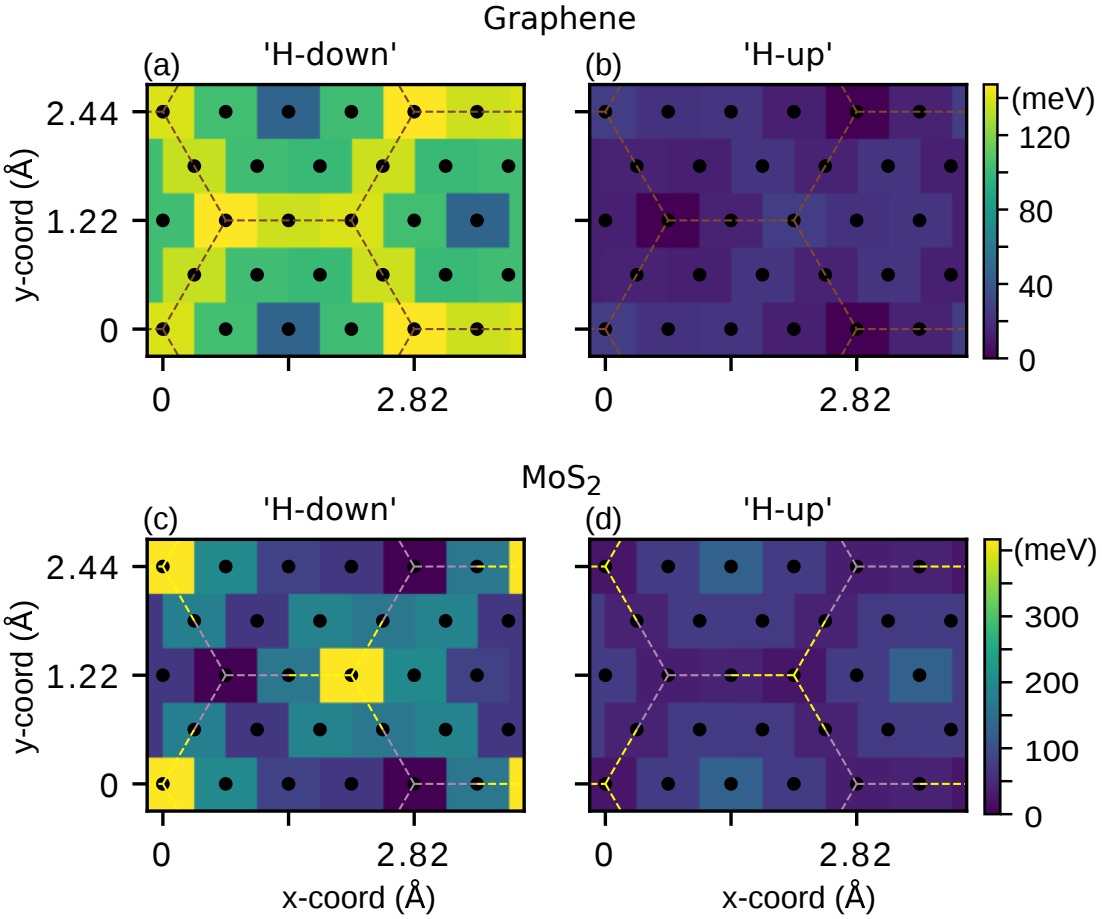

Figure 3.4: Potential energy surface (PES) at a fixed in-plane rotational angle for chloroform in (a) the "H-down" configuration on graphene, (b) the "H-up" configuration on graphene, (c) the "H-down" configuration on MoS_2 and (d) the "H-up" configuration on MoS_2.

Similarly, for the case of the "H-up" adsorption configuration (shown in Fig. 3.4(b)), when the three chlorine atoms are adsorbed directly above the hollow site (so that the COM of the molecule is above a carbon atom), the p_z - lone pair repulsion is minimized, resulting in the global minimum in the total

energy. When the chlorine atoms are adsorbed directly above the carbon atoms, maximum p_z - lone pair repulsion occurs leading to a local maximum in the total energy.

The PES for chloroform adsorbed in a "H-down" configuration on MoS_2 is shown in Fig. 3.4(c). When the H atom is adsorbed directly above the sulfur atom (the yellow dashed lines), the small distance between the atoms results in maximum lone pair - s orbital repulsion and hence a global maximum in the total energy. In contrast, when the H atom is adsorbed directly above the metal atom, in the hollow formed by the sulfur atoms, four atoms are now involved in van der Waals interactions without any increase in orbital repulsion. This leads to a global minimum in the total energy.

Similarly, for the case of the "H-up" adsorption configuration (shown in Fig. 3.4(d)), the adsorption of the central carbon atom (and COM) directly above metal atom results in a local maximum in energy. The minimum in energy is found when the central atom is adsorbed on top of the sulfur atom so that the chlorine atoms adsorb directly on top of the hollow site.

In the case of asymmetric molecules such as chloroform where the center of mass is closer to the chlorine atoms, on rotating the molecule out of plane, the atoms can be unphysically close to the surface of the layer. This can explain the large variation in the corrugation of the potential energy surface shown in Fig. 3.4 for 'H-up' and 'H-down'. In this approach the corrugation is overestimated for a particular rotation. However, the associated uncertainty for the minimum energy configuration is reduced by geometrically optimizing candidates from both the 'H-up' and 'H-down' configurations.

An alternative to this approach that provides a better approximation for the corrugation in the potential energy surface is to make the binding height a function of molecular rotation. While providing a better approximation for the potential energy surface, this approach also eliminates the requirement for geometry optimization of candidate structures. The binding height can be chosen by performing geometry optimizations for a candidate configuration from all the out-of-plane rotations and then using the optimized binding height to calculate the potential energy surface for that rotation.

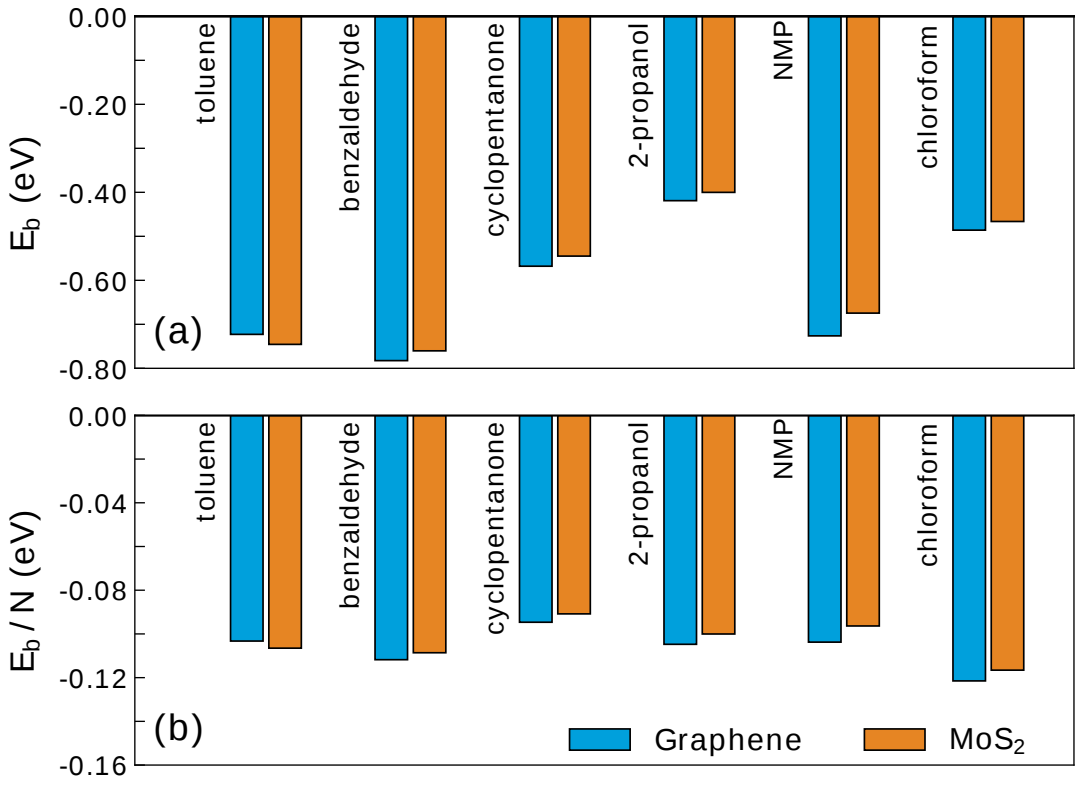

Figure 3.5: (a) Binding energy of each molecule on a graphene (blue) and MoS_2 (orange) substrate. (b) Binding energies normalized by the number of non hydrogen atoms, N, in the molecule.

3.2.2.3 Binding Energy

The binding energy between the layered material and the adsorbed solvent molecule is defined as:

$$E_b = E_{\text{mol+layer}} - E_{\text{layer}} - E_{\text{mol}}$$

where E_{layer} is the total energy of the clean monolayer, E_{mol} is the total energy of the isolated molecule and $E_{\text{mol+layer}}$ is the total energy of the combined system. The binding energies of each solvent molecule adsorbed on both graphene and MoS_2 are shown in Fig. 3.5(a). They range between -0.4 eV and -0.79 eV per molecule. The binding energy of each molecule differs by no more than 7% when adsorbed on graphene compared to MoS_2. The molecular binding energy rescaled by the total number of atoms in that molecule, excluding hydrogen, N, is then shown in Fig. 3.5(b). In all cases, the normalized binding energies lie in a narrow range between approximately 90 and 120 meV/atom, and with a difference of no more than 5 meV/atom between individual molecules adsorbed on graphene

and MoS_2. A similarly narrow range of normalized binding energy was found for aromatic and conjugated compounds adsorbed on MoS_2 [174] and graphene [178] and shown experimentally for acenes adsorbed on copper surfaces [179]. This is evidence of the dominance of the van der Waals contribution to the binding energy. Further evidence is found by neglecting the non-local contribution to the correlation energy in the optB86b-vdW functional. In this case a positive binding energy can be found for all the molecules considered on both surfaces. In a similar way, the interlayer binding energy of graphite was previously shown to be positive using the optB86b-vdW functional when only local contributions to the correlation energy are considered[70].

3.2.2.4 Charge Transfer and Rearrangement

The magnitude of total charge transfer between the molecules and both graphene and MoS_2 is no more than $0.11e^-$ per molecule as determined by both the Bader and the DDEC methods. In some cases, these two methods do not agree on the direction of the charge transfer. Given the difficulties in partitioning space in order to assign charge to the molecule or substrate, this magnitude of the charge transfer may be considered essentially zero.

This is corroborated by a negligible difference in the charge density located on the monolayers before and after adsorption, as shown in Fig. 3.6. From this, we can conclude that the changes in the photoluminescence spectra found by Choi et al. after solvent adsorption on MoS_2 and attributed to charge transfer to/from the layer, must be due to interactions between the solvent molecules and defects in the layers, or with edge sites [159]. Such defects and edge sites have previously been shown to be considerably more reactive than the pristine surface [180, 181, 182].

Notwithstanding the negligible charge transfer involved, significant charge reorganization occurs on both the molecule and the 2D layer as as result of their interaction. To visualize this, we show in Fig. 3.7 a slice through the charge density difference that occurs after molecular adsorption on graphene and MoS_2 at a height of 0.5 Å above the surface of the monolayer. This height highlights the changes that occur in the outermost valence orbitals of the 2D layers. The charge density difference is defined as:

$$\Delta\rho = \rho_{\mathsf{mol+layer}} - \rho_{\mathsf{mol}} - \rho_{\mathsf{layer}}$$

where $\rho_{\mathsf{mol+layer}}$, ρ_{mol} and ρ_{layer} are the charge densities of the molecule adsorbed

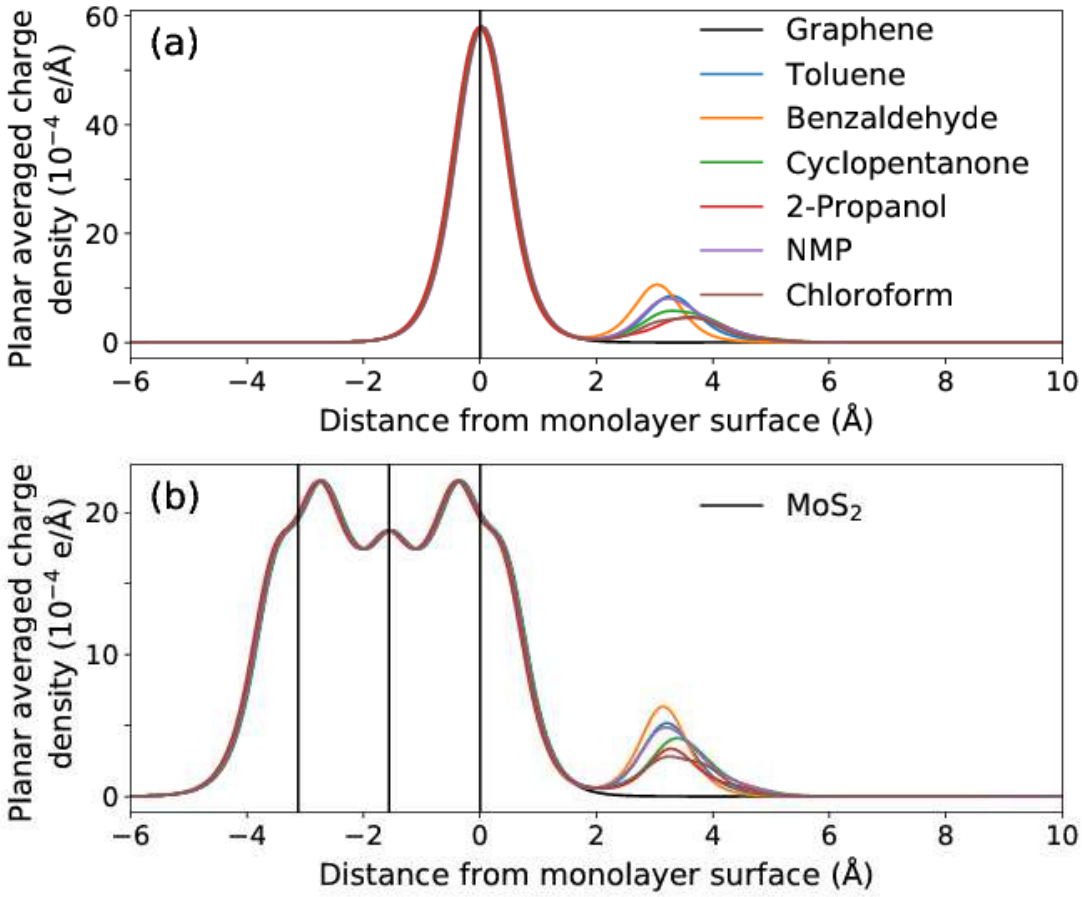

Figure 3.6: Planar average of the charge density of each of the six molecules adsorbed on (a) graphene and (b) MoS_2 compared to the pristine monolayers. The vertical lines indicate the positions of atoms in the monolayers. Note that the average values of the charge density is dependent on the unit cell size and so only qualitative analysis is possible using this quantity.

system, the isolated molecule and the isolated layer, respectively. A charge rearrangement reminiscent of image charges[183] on a metal is found to occur after molecular adsorption on graphene. As a result of their high polarizabilities[184], the substrate's charge density is modified by the polar bonds of the adsorbing molecule. This can be seen as the response of the layer to the net dipole of the molecule. The molecule then interacts with its image charge.

For the case of toluene, the small net molecular dipole points towards the methyl group. As a result, a small charge accumulation (red) is evident beneath the methyl group and a charge depletion (blue) occurs beneath the carbon ring. This dependence of the charge rearrangement on the molecular dipole is particularly evident for molecules with an electronegative oxygen atom, such as benzaldehyde,

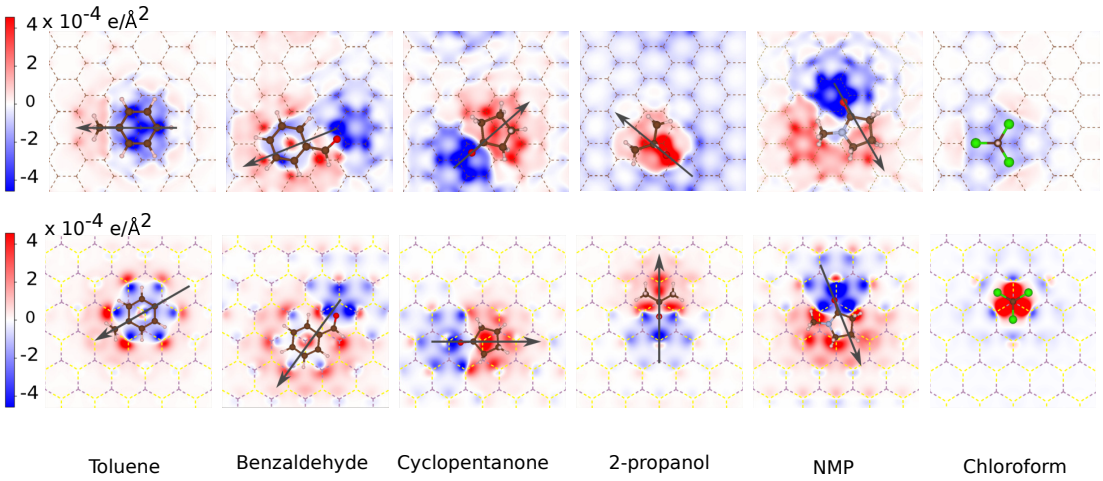

Figure 3.7: Top (bottom) panel: A slice through the charge density difference 0.5 Å above the graphene (MoS_2) plane. Blue represents electron density depletion and red represents an electron density accumulation. The arrows represent the in-plane direction (but not magnitude) of the molecular dipole. The dipole of chloroform is perpendicular to the plane of the monolayer, pointing towards (away from) the layer for the case of graphene (MoS_2).

cyclopentanone and NMP. In these cases, charge depletion occurs beneath the oxygen atom, whereas there is charge accumulation beneath the carbon ring. This is true for those molecules adsorbed on both graphene and MoS_2. Similarly, in 2-propanol the net dipole points away from the oxygen atom. However, the response of the 2D layer to 2-propanol depends on the out-of-plane rotation of the molecule. For the case of graphene, the molecule is adsorbed with the hydrogen atom, which is bound to the oxygen atom, pointing towards the surface. This hydrogen atom has a partial positive charge, and so results in charge accumulation in the layer directly beneath it. When adsorbed on MoS_2, that hydrogen atom points away from the surface. The charge depletion in the sulfur atoms of the substrate is then as a result of the partial negative charge on the oxygen atom. Finally, for the case of chloroform adsorption, the net dipole is perpendicular to the layers so that the changes in charge density around the molecule are symmetric. As the chlorine atoms have partial negative charges, charge depletion is evident directly beneath them when adsorbed on graphene, whereas there is a charge accumulation beneath the hydrogen atom which adsorbs on top of the metal atom of MoS_2.

3.2.3 Conclusion

In conclusion, we have determined the adsorption configuration of six common solvent molecules on the basal plane of both graphene and MoS_2 using first-

principles calculations which take van der Waals interactions into account. The calculated binding energies, adsorption heights and charge transfer all show that the solvent molecules are physisorbed on graphene and MoS_2, with only minor variations in binding height and binding energy between the different molecules and on the two different monolayers.

For those molecules which contain a carbon ring, we find the the lowest energy adsorption configuration on graphene to be one in which a Bernal-like stacking arrangement of the carbon atoms is achieved. Non-planar molecules which have hydrogen atoms pointing towards the surface adsorb such that those atoms are located in the hollow site of the substrate lattice. We find that the orientation of both 2-propanol and chloroform are rotated by 180° when comparing adsorption on graphene and MoS_2.

Finally, despite negligible charge transfer between the solvent and monolayers, there is a significant charge rearrangement within the substrate layers in response to the partial charges on the atoms in the molecules, similar to the creation of an image charge in metals.

Liquid-phase exfoliation is strongly dependent on the type and nature of solvent as well as the material being exfoliated. Here, we have shown that this cannot be attributed to differences in how individual molecules of that solvent interact with the surface of the 2D layer. Instead, the collective behavior of these molecules at high concentrations may play a important role. In the next section we show that the interaction energy is independent of the molecule type at high concentrations and that the dynamical behaviour of molecules near the graphene surface should be considered.

3.3 Interaction of liquid solvents with graphene

In the absence of any differentiation in the nature of the interaction between individual molecules, the next step is to include multiple molecules. Intermolecular interactions now become important, as these can modify the orientation and interaction of the solvent molecules with the surface.

In this section, we address three open questions: (1) Does the behavior of the solvent at the interface between solid and liquid play a role in the stabilization of the monolayers in dispersion or, in other words, is it sufficient to consider only energetic effects via the enthalpy of mixing when choosing screening descriptors, (2) What is the physical mechanism leading to the experimental finding of a non-zero polar component of the Hansen solubility parameter of graphene and (3) How important are kinetic effects, such as reaggregation, to the stabilization of graphene?

We find that there is a molecular-level structural and orientational ordering of the solvent molecules at the solid-liquid interface which extends up to 30 Å away from the graphene layer. These solvation layers form in all cases and behaves similarly irrespective of the solvent polarity. The formation of these solvation shells can explain the non-zero polar Hansen solubility parameter as it is not isolated graphene that is measured experimentally but that of an effective solute comprised of graphene and its solvation shells. These interfacial layers of solvent do not behave similarly to the bulk solvent. Due to surface confinement, the dielectric constant associated with these interfacial molecular layers will be dramatically reduced. Finally, we find that kinetic effects, and in particular the diffusion behaviour of these solvation shells parallel to the graphene sheet, is a reliable descriptor determining the stability of graphene monolayers in solution.

3.3.1 Methods

The twelve solvents included in this investigation are listed in Table 3.2 and were chosen to include those reported by Hernandez et al. [145] to result in a wide range of graphene concentrations after exfoliation. They include cyclopentanone (best performing solvent, polar aprotic), benzaldehyde (low performance, polar aprotic), bromobenzene (intermediate performanace, slightly non-polar) and toluene (low performance, non-polar). All others have

intermediate performance or polar properties. The maximum graphene concentration was achieved by exfoliation in cyclopentanone, resulting in a concentration of 8.5 ± 1.2 μg/ml. Exfoliation in non-polar solvents, including toluene, heptane, hexane and pentane, resulted in much lower graphene concentrations of 0.8 ± 0.4 μg/ml, 0.3 ± 0.4 μg/ml, 0.2 ± 0.1 μg/ml and 0.16 ± 0.05 μg/ml, respectively. However, some highly polar molecules such as water and formamide also perform poorly, with the best performing solvents having a slightly polar nature (although not all slightly polar solvents perform well).

3.3.2 Molecular Dynamics

Molecular dynamics calculations are performed using the Large-scale Atomic/Molecular Massively Parallel Simulator (LAMMPS) [185]. As the interaction between graphene and isolated solvent molecules was found be primarily attractive disperion forces [186, 187], it can be modelled accurately using classical van der Waals (vdW) force fields.

The graphene monolayer is modeled as uncharged vdW spheres. These spheres are described by interaction parameters originally reported by Steele et al. [188] and later used to describe the interaction between graphene and molecular adsorbants [189, 190, 191, 192]. The molecules are described by the All Atom Optimized Potentials for Liquid Simulations (OPLS-AA) potentials, which were obtained from LigPargen web server [193, 194, 195]. The pair interaction coefficients between graphene and the molecules are obtained using Lorentz-Berthelot rules [112, 114]. Binding energies calculated using these potentials agree with experiment for small organic molecules adsorbed on graphene [186].

The initial solvent structure was created using packmol [196] in a box size of 105.91 Å × 106.65 Å × 120.0 Å to reproduce the experimental room-temperature densities (given in Table 3.2). The graphene monolayer was then included in the simulation box by increasing the box size in the direction normal to the plane by (2 × 3.5)Å to account for the increase in the volume due to the introduction of graphene. The python package pymatgen was used to generate the LAMMPS structural data file [197].

The system was annealed from 600 K to 300 K for 50 fs with an integration timestep of 0.01 fs and then equilibriated at 300 K for 1 ns with an integration timestep of 1 fs. The system was further simulated with the NVE ensemble for

Molecules	density (g/ml)	dipole moment (D)
Cyclopentanone	0.95	3.28
Cyclohexanone	0.95	2.9
NFP	1.02	-
Bromobenzene	1.5	1.74
Benzonitrile	1.01	3.2
NMP	1.03	4.1
Chlorobenzene	1.11	1.55
1,3-dioxolane	1.06	1.19
Quinoline	1.09	2.0
Benzaldehyde	1.04	2.89
Acetone	0.78	2.9
Toluene	0.87	0.31

Table 3.2: Experimental densities and dipole moments of the molecules used in the calculations. These numbers are extracted from the on-line databases. [198, 199]

2 ns, of which 2000 samples from the last 1 ns were used to generate statistical distribution functions. For the duration of the complete simulation the graphene layer is held fixed.

3.3.2.1 Diffusion Coefficients

The diffusion coefficient of solvent molecules confined in a region $[a, b]$ parallel to the graphene sheet, $D_{\parallel}$, can be determined from MD trajectories using the method described in Liu et al. [125], Agosta et al. [124] and summarized in Section 2.12.

For these calculations, the equilibrated structure was simulated with the NVE ensemble for 150 ps and the center of mass of each molecule recorded at each time step. A time window (τ) of 35 ps is used to calculate the diffusion coefficient.

3.3.2.2 Helmoltz Free Energy

The Helmoltz free energy of interaction is determined using the finite difference thermodynamic integration method (FDTI) described in Section 2.10.

The free energy is then calculated as:

$$\Delta H = \int \left\langle \frac{\partial U(\lambda)}{\partial \lambda} \right\rangle \approx \sum_{i=0}^{N-1} w_i \left\langle \frac{U(\lambda_i + \delta) - U(\lambda_i)}{\delta} \right\rangle \tag{3}$$

where $\langle ... \rangle$ indicates an ensemble average, w_i are integral weights and δ is the finite difference parameter which satisfies $(\lambda_i - \lambda_{i-1}) >> \delta$. For these calculations we simulate the system for 10 ns in the NVT ensemble at 300K. The parameter λ is incremented in 40 steps or every 250 ps with the finite difference parameter δ of 0.001. For each λ, first 100 ps are discarded for equilibration. A sample taken every 20 fs from the last 150 ps is used to calculate the ensemble average at that λ.

This calculated free energy can further be decomposed into the enthalpy and entropy contributions. These are determined as the slope and y-intercept of the line $\frac{\Delta G}{T}$ versus $\frac{1}{T}$, respectively. The free energy is calculated at temperatures 290 K, 300 K and 310 K.

3.3.2.3 Local Permittivity

To calculate the local permittivity for a periodic molecular slab, the density functional theory (DFT) calculations are performed using the projected augmented wave (PAW) method as implemented the QUANTUMESPRESSO code. Pseusopotentials (pbe-kjpaw) from the pslibrary (V1.0.0) are used. A wavefunction cutoff of 94 Ry is used for all calculations. The Brillouin zone is sampled with a $10 \times 10 \times 1$ Monkhorst-Pack mesh [168] with a Gaussian smearing width of 0.0018 Ry. All electronic calculations are converged with a threshold of 7×10^{-9} Ry. No geometry optimization is performed, so that the molecular orientation is kept fixed.

To make the calculations computationally tractable, for a molecule in a given orientation, the unit cell contains one molecule. The size of the orthorhombic unit cell is chosen such that the atoms in the adjacent molecules are at least 3.5 Å apart in the periodic direction of the molecular slab. In the direction perpendicular to the slabs, a vacuum of 20 Å is included to decouple the periodic images. In this direction the dipole correction is enabled with the counter dipole placed in the center of the vacuum region.

To aid convergence, the charge density is first calculated without the inclusion of the required dipole correction. The dipole correction is then added, and the

corresponding charge density (ρ_0) and the Hartree potential (V_0^H) are saved. Finally, an external electric field of 0.001 Ry a.u. is applied and the corresponding charge density (ρ_E) and the Hartree potential (V_E^H) are saved. In the last two steps, the electron density and the Hartree potential are saved on the three dimensional FFT grid. This can then be used to calculate the relative permittivity profile, $\epsilon(z)$ using Eq. 40, Eq. 41 and Eq. 42, as described in Section 2.5. From $\epsilon(z)$ the effective dielectric constant perpendicular to the molecular layer can be calculated as:

$$\epsilon_{\text{layer}} = \frac{1}{z_2 - z_1} \int_{z_1}^{z_2} \frac{1}{\epsilon(z)}\, dz \tag{4}$$

where z_1 and z_2 are the planes between which the molecular layer is bound. The limits z_1 and z_2 are defined by the positions where the average electron density (ρ_0) falls below 0.001 Å^{-3}.

This calculated local dielectric constant (ϵ_{layer}) is the true dielectric constant only when the molecules are confined and cannot move after the application of an external electric field. In the intermediate case where the molecules have reduced freedom to rotate, the dielectric constant will be higher than this calculated value. These calculated local dielectric constants (ϵ_{layer}) are an indication of the electronic contribution to the local permittivity. The true permittivity of the first solvation shell could be higher than these calculated values here and can be calculated using molecular dynamics simulations.

3.3.3 Results

3.3.3.1 Solvation Shell Formation

The position distribution function $g(z)$, the polar angle distribution function $\theta(z)$ and the azimuthal angle distribution angle $\phi(z)$ of the molecular dipoles close to graphene are shown in Fig. 3.8. The graphene layer is located at 0 Å. The polar angle is measured with respect to the axis aligned to the positive direction (towards the right). $g(z)$ is given relative to the bulk solvent number density so that a value greater (less) than 1 indicates an accumulation (depletion) of molecules relative to the bulk solvent. $\theta(z)$ is the probability distribution function of the polar angle of the molecular dipole, where 90° corresponds to the molecular dipole in the plane parallel to graphene and 0° (or 180°) corresponds to the molecular dipole in the plane perpendicular to the plane of graphene. The panels of Fig. 3.8 shows the 90° orientation of the

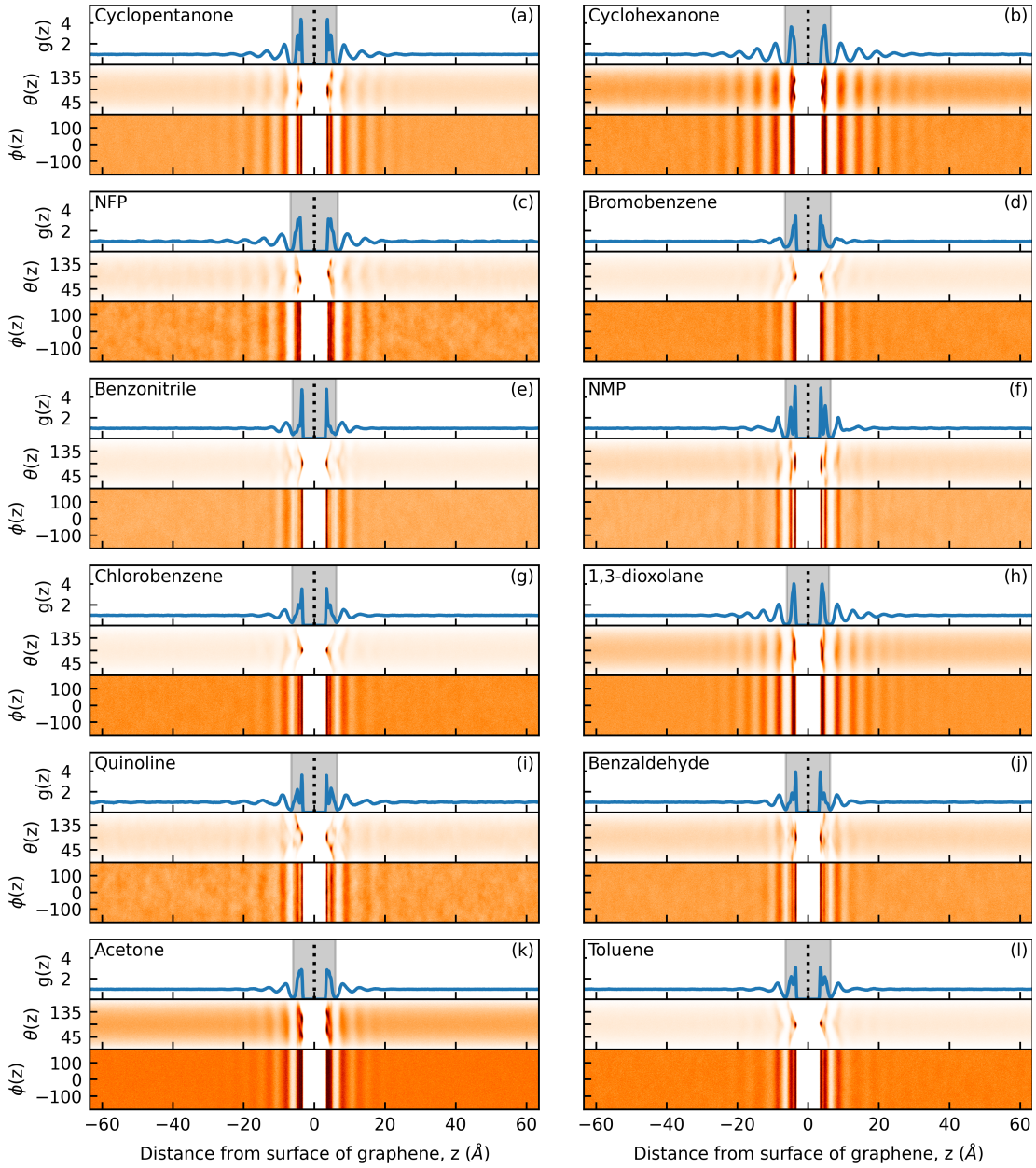

Figure 3.8: Pair distribution functions for the center of mass of the molecule and the graphene layer. (Top panel) $g(z)$ a histogram of the center of mass of the solvent molecules normalised by $(\frac{N}{L}dz)$ where N is the number of molecules in the unit cell, L is the length of the unit cell and dz is the bin width. The graphene monolayer is located at $z = 0$ Å. (Middle panel) $\theta(z)$ is the probability distribution function of the polar angle of the molecular dipole, where $90°$ corresponding to the molecular dipole in the plane parallel to graphene and $0°$ ($180°$) corresponds to the molecular dipole in the plane perpendicular to the plane of graphene. (Bottom panel) $\phi(z)$ is the probability distribution function of the azimuthal angle of the molecular dipole, indicating the orientation of the dipole in the plane parallel to the plane of graphene, with $0°$ ($180°$) corresponding to the orientation along positive (negative) x-axis, $90°$ ($-90°$) corresponding to the orientation along the positive (negative) y-axis.

molecule molecular dipole with the polar axis out of the plane of the paper. $\phi(z)$ is the probability distribution function of the azimuthal angle of the molecular dipole, indicating the orientation of the dipole in the plane parallel to the plane of graphene, with $0°$ ($180°$) corresponding to the orientation along positive (negative) x-axis, $90°$ ($-90°$) corresponding to the orientation along the positive (negative) y-axis.

Although the molecular dipole is located in the molecular plane, in order to completely determine the orientation of the molecule with respect to the graphene layer the angle (α) made by the normal to the plane of the molecule with respect to the z axis is necessary. The position distribution function $(g(z))$ and the angle distribution function $\alpha(z)$ with the z axis aligned to the positive direction (towards right) is shown in Fig. 3.9. The graphene layer is again located at 0 Å.

By examining Fig. 3.8, we see that, irrespective of the polar nature of the molecule, distinct solvation shells are formed next to the graphene layer as a result of surface confinement, molecule-molecule interactions and molecule-graphene interactions. The first solvation shell can be recognized as a peak in $g(z)$ followed by a deep trough near the surface of graphene (grey shaded area). The distance between graphene and the atom of the molecule nearest graphene is determined by the vdW interaction, and so is very similar, regardless of the particular orientation of the molecule. It varies from 1.99 Å for bromobenzene to 2.07 Å for benzaldehyde, as summarized in Table 3.3.

The first solvation shell has a complex structure in most cases due to the way the molecules adsorb on graphene. This is particularly evident for cyclopentanone (Fig. 3.8(a)) and NMP (Fig. 3.8(f)) where the first solvation shell is composed of two distinct peaks. The reason for this can be found by looking at $\alpha(z)$ in Fig. 3.9(a,f): the solvent adsorbs on graphene with two distinct angular orientations – one with the molecular plane lying approximately parallel to the surface and one with the plane almost perpendicular. As the distribution function is based on the centre of mass of the molecules, this manifests as a double peak structure. As a result, the dipole moments of the molecules also show two distinct polar angles $(\Theta(z))$, whereas the azimuthal angle $(\phi(z))$ shows no distinct orientation preference indicating no in-plane ordering of dipoles. The two peaked behavior is schematically illustrated in Fig. 3.10. This behavior was previously found in molecular dynamic calculations involving NMP interacting with both graphene and

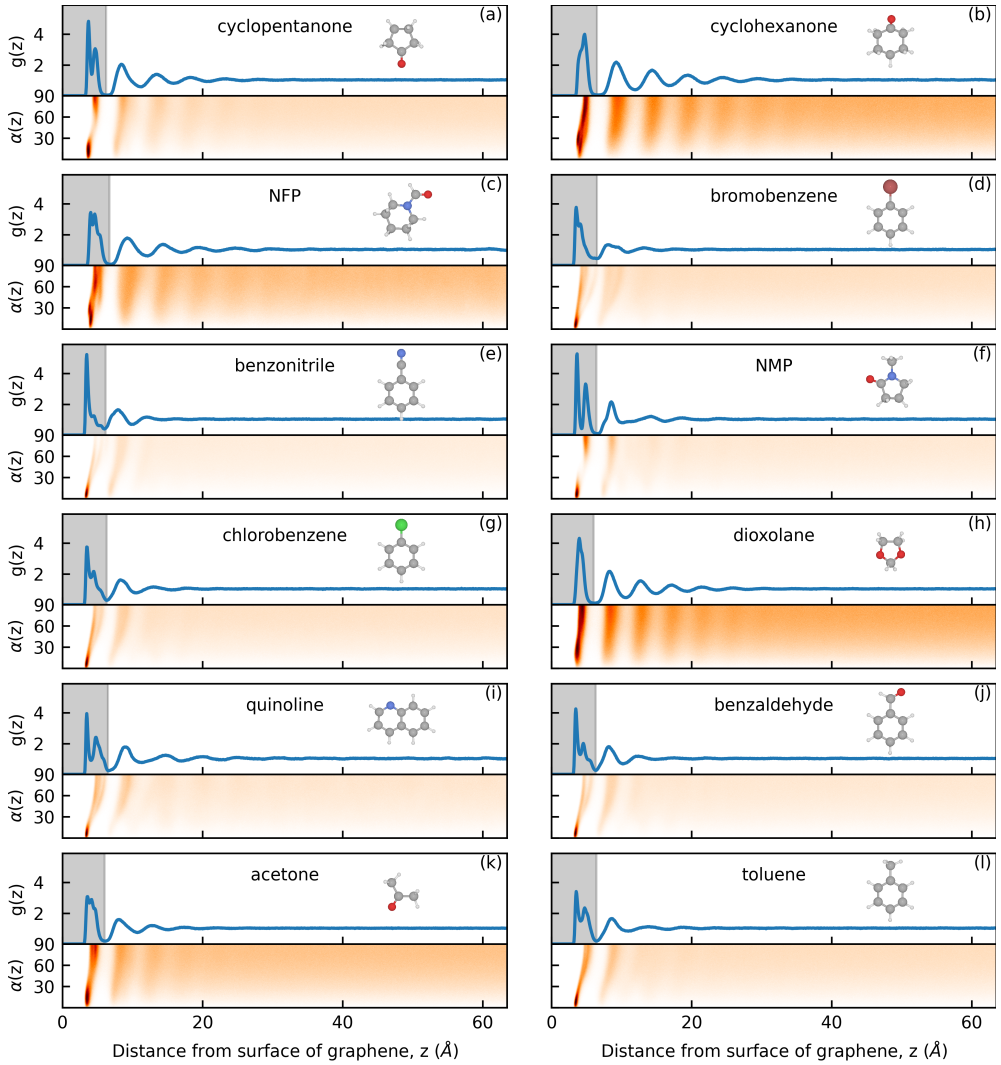

Figure 3.9: Pair distribution functions for the center of mass of the molecule and the graphene layer. (Top panel) $g(z)$ is the distribution of center of mass of molecules (i.e., the same as presented in Fig. 3.8). (Bottom panel) $\alpha(z)$ is the angle made by the normal to the plane of molecule with the axis perpendicular to the plane of graphene.

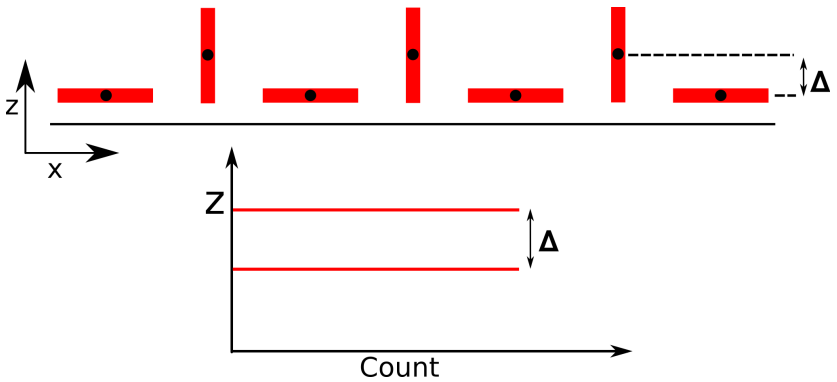

Figure 3.10: Toy model demonstrating the origin of the two peaked behavior in $g(z)$.

carbon nanotubes [191, 200, 201].

In other cases, the distinction between the two peaks is not as clear. For example, the first solvation shell of cyclohexanone (Fig. 3.8(b)) has a small peak corresponding to those molecules located closest to graphene and orientated parallel to graphene, but the remainder of the molecules in the first solvation shell do not exhibit an angular preference. This is also the case for NFP (Fig. 3.8(c)), bromobenzene (Fig. 3.8(d)), chlorobenzene (Fig. 3.8(g)), dioxolane (Fig. 3.8(h)), quinoline (Fig. 3.8(i)), acetone (Fig. 3.8(k)) and toluene (Fig. 3.8(l)). In all cases, the dipole moments of the molecules show polar angles consistent with the orientation of the molecular planes. For the case of benzonitrile (Fig. 3.8(e)) and benzaldehyde (Fig. 3.8(j)) the first solvation shell is comprised almost entirely of molecules lying parallel to the graphene layer, with no second peak visible.

This distinction in the molecules could be due to the orientation dependence of the binding energy in between the graphene layers and the molecules. This orientation dependence is due to the nature of the van der Waals interaction, where the interaction energy is the sum of pair wise interaction between all the atoms in the molecules. The molecules orient in such a way that the number of atoms near the graphene layer is maximized. Molecules that are found to orient perpendicular to the plane of graphene fill all the gaps that exist in between the flat-lying molecules.

Within the first solvation shell we can determine the percentage of molecules in each of these two peaks, particularly for those with two very distinct peaks. In the case of cyclopentanone, 49% of the molecules are present in the first peak of the first solvation shell, that is lying parallel to the graphene plane. This value reduces to 48%, 41% and 37% for NMP, toluene and quinoline, respectively.

To visualize this orientational ordering, Fig. 3.11 shows a snapshot from the molecular dynamics simulation showing only the first solvation shell of benzonitrile and NMP. As expected in the case of benzonitrile from Fig. 3.8(e), the majority of molecules are adsorbed with their plane orientated parallel to graphene (shaded in red) and very few molecules are adsorbed perpendicularly to graphene (green shading). In the case of NMP, a small but significant number of NMP molecules are adsorbed perpendicularly to the sheet (Fig. 3.8(e)). This is evident in the larger proportion of molecules shaded in green as compared molecules shaded in red. Note however that strong long-range lateral order is not present. This can be verified by calculating the pair correlation functions

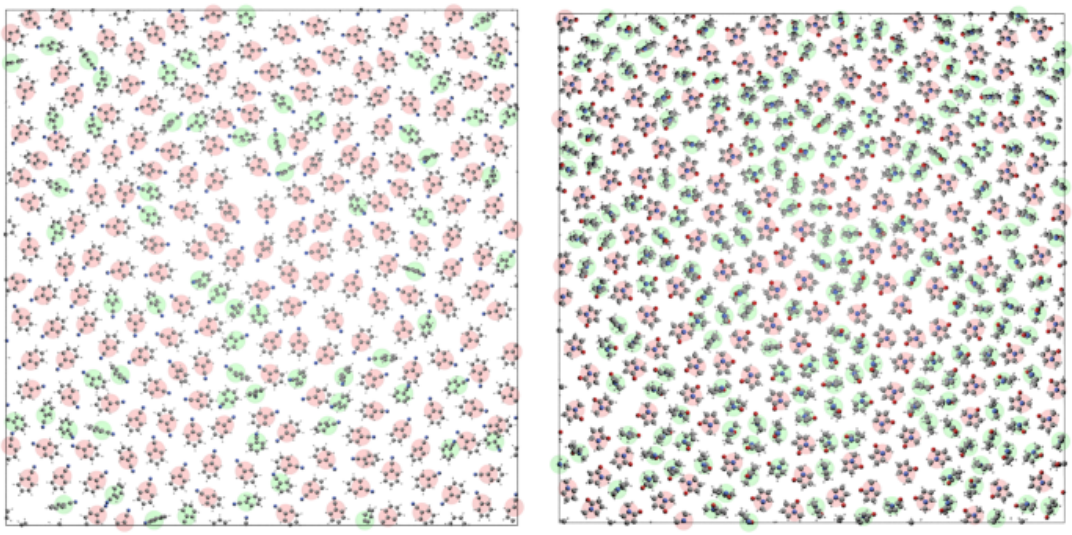

Figure 3.11: A snapshot of molecules in first solvation shell of benzonitrile (left) and NMP (right) with red circles indicating molecules belonging to the first peak in the solvation shell and green circles indicating the rest of the molecules. It can be seen that the molecules in the first peak are parallel ($\theta \approx 0°$) to the plane of graphene and the molecules in the second peak are biased towards the transverse direction ($\theta \approx 90°$).

for the geometric centers for the molecules in the first solvation shell and is shown in Fig. 3.12. In all cases, there is a local ordering around the center (0,0) due to the presence of an exclusion zone around the molecule. This ordering decays rapidly moving away from the center. The strongest ordering is seen in case of cyclopentanone (Fig. 3.12(a)), cyclohexanone (Fig. 3.12(b)) and 1,3-dioxolane (Fig. 3.12(h)). Intermediate ordering behaviour is seen in case of NFP (Fig. 3.12(c)), benzonitrile (Fig. 3.12(e)), NMP (Fig. 3.12(f)), quinoline (Fig. 3.12(i)), acetone (Fig. 3.12(k)) and toluene (Fig. 3.12(i)), with no ordering beyond the first shell seen in case of bromobenzene (Fig. 3.12(d)), chlorobenzene (Fig. 3.12(g)) and benzaldehyde (Fig. 3.12(j)).

Terrones et al. previously found that a monolayer of NMP molecules confined between two graphene sheets exhibit long-range hexagonal ordering, but that this is ordering is lost as the thickness of the molecular layer increases. This agrees with our calculations, which show very little ordering near the graphene sheet [201]. The confinement of molecules near the surface of graphene can also be measured experimentally [153]. Arunachalam et al. showed that the NMP molecules near the surface of graphene show a reduction in rotational degrees of freedom using rotating frame Overhauser effect spectroscopy – nuclear magnetic resonance (ROESY–NMR) technique [153].

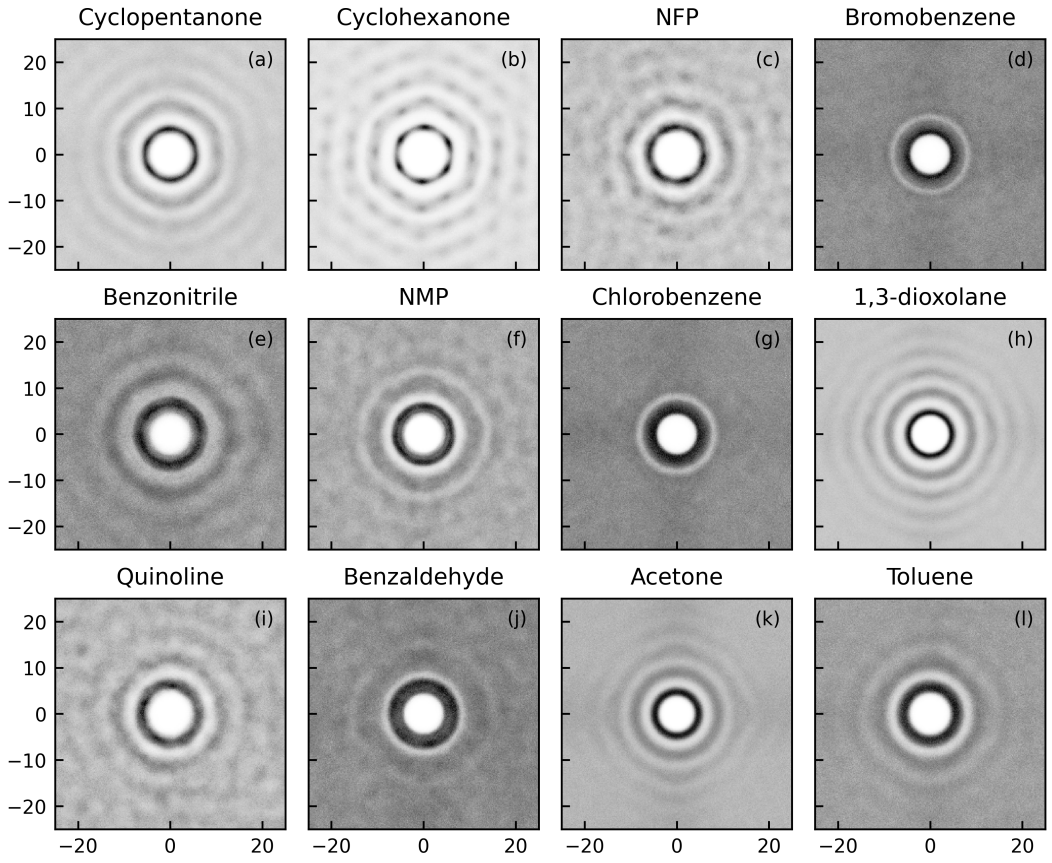

Figure 3.12: Pair correlation function of the center of geometry of the molecules present in the first solvation shell.

The peak associated with the first solvation shell is also the sharpest, indicating that the highest degree of transverse ordering occurs for those closest to graphene. In response to the formation of the first molecular layer, the rest of the solvent reorganizes to form further solvation shells as seen in Fig. 3.8. As expected, the amplitude of the peak decays as the effect of the solute vanishes, finally approaching a constant, indicating bulk solvent behaviour.

The positions of the atoms closest to the graphene layer, the number of solvation shells (N_{shells}), the depth to which the solvation shells extend from graphene, the average distance between two consecutive solvation shells and the excess number of molecules in the first solvation shell (N_1^{excess}) are given in Table. 3.3. For all molecules the atoms closest to the graphene layer lie in a very narrow window around 2 Å, with a minimum of 1.99 Å for bromobenzene and a maximum of 2.07 Å for benzaldehyde. The positions of the solvation shells are extracted manually with the last shell defined as the last peak that deviates from bulk by at most 5%. The number of solvation shells varies from a minimum of 3 in the case of bromobenzene, benzonitrile, chlorobenzene and benzaldehyde to a maximum of

Molecules	Z_{min}	N_{shells}	Depth (Å)	Period (Å)	N_1^{excess} %
Cyclopentanone	2.03	5	23.34	4.97	54.57
Cyclohexanone	2.02	6	29.31	5.02	56.57
NFP	2.0	5	24.67	5.14	49.56
Bromobenzene	1.99	3	13.11	4.95	35.3
Benzonitrile	2.03	3	12.16	4.25	28.03
NMP	2.0	4	18.7	5.08	46.12
Chlorobenzene	2.02	3	12.92	4.64	36.16
1,3-dioxolane	2.05	6	25.94	4.41	47.6
Quinoline	2.0	5	24.86	5.25	37.66
Benzaldehyde	2.07	3	12.41	4.38	33.21
Acetone	2.02	4	17.37	4.7	48.3
Toluene	2.01	4	18.51	4.95	40.24

Table 3.3: The table contains data extracted from the histograms in Fig. 3.8. Z_{min} indicates the distance of atom nearest to graphene, N_{shells} indicates the number of solvation shells, depth indicates the distance of last solvation shell from graphene, period indicates the average periodicity of the solvation shells and N_1^{excess} indicates the percentage of excess molecules in the first solvation shell. If we define the the last solvation shell to be that with a maximum peak which deviates from bulk by at most 5%.

6 for cyclohexanone and 1,3-dioxolane. The average distance between adjacent solvation shells ranges from 4.25 Å for benzonitrile to 5.25 Å for quinoline.

Despite these differences, it is clear from Fig. 3.8 that the solvation structure cannot be used to explain the observed phenomenon of solvent-dependent graphene stabilization. For example, there is no appreciable difference between the solvation structure of cyclopentanone and toluene, one of the best and worst solvents for the LPE of graphite, respectively.

3.3.3.2 Effect of Confinement on Electric Permittivity of First Solvation Shell

The dielectric response of polar molecules to an external electric field, E_{ext}, is a result of both the alignment of the permanent dipoles (μ_{per}) to E_{ext} and any induced dipole moment (μ_{ind}) resulting from the electron density relaxation in response to the external field. The polar molecules in the first solvation shell do not behave as they would in the bulk liquid due to the confining potential of the graphene surface. If they are no longer free to rotate with an external electric

field [153], their response will be dominated by μ_{ind} alone.

To determine how this depends of the type of solvent, we calculate the local dielectric constant associated with the molecules in the first solvation shell assuming a toy example where the molecules are held fixed by the graphene layer and are not free to rotate. The calculations are done using using density functional theory for a periodic slab with one molecule per unit cell as described in section 3.3.2.3. To make this computationally tractable, we make the assumption that all molecules are fixed in certain representative orientations. These orientations are chosen in such a way that the dipole moment of the molecule rotates in the plane perpendicular to the plane of the two dimensional layer.

The first thing to note is that the electronic response is not affected by the magnitude of the solvent dipole moment, with very similar average values found for chlorobenzene (bulk dielectric constant of 5.7) and NMP (bulk dielectric constant of 32.0). We rotate the molecule in 12 steps such that the dipole moment of the molecule rotates a full 360° in the plane perpendicular to the two dimensional slab. In Table 3.4, we present the maximum and minimum calculated dielectric constant of all rotations, as well as the average value. The calculated dielectric constant for the fixed molecular monolayer does not depend strongly on the orientation of the polar molecule. It lies in a very narrow range with maximum value of 2.08 for chlorobenzene and minimum value of 1.52 for cyclopentanone and cyclohexanone.

This reduction in the permittivity of confined molecules are previously observed for the case of water confined in a graphene slit pore. Fumagalli et al. reported a surface-layer dielectric constant of 2, compared with the bulk value of 80 for water, and attributed this to an inhibition of rotational motion of water at the surface [202]. In some cases, confinement can even result in the observation of a negative local permittivity. This was shown to be the case for water confined between the layers of titanium carbide MXene nanosheets in the presence of Group-1 metal ions [203].

3.3.3.3 Free Energy of Formation

Near the surface of a graphene monolayer, a negative Helmholtz free energy of interaction (ΔG_{mix}) is an indication of the favorable formation of a solvation structure. As $\Delta G_{\mathsf{mix}} = \Delta H_{\mathsf{mix}} - T\Delta S_{\mathsf{mix}}$, where ΔH_{mix} and ΔG_{mix} are the enthalpy and entropy of mixing, a requirement of mixing is that $\Delta H_{\mathsf{mix}} < T\Delta S_{\mathsf{mix}}$.

Solvent	ϵ_{bulk}	ϵ_{max}	ϵ_{min}	ϵ_{avg}
Cyclopentanone	1.56	1.52	1.54	13.6
Cyclohexanone	1.56	1.52	1.54	15.0
Bromobenzene	2.3	2.11	2.21	5.4
Benzonitrile	2.0	1.82	1.92	26.0
NMP	1.6	1.52	1.56	32.0
Chlorobenzene	2.18	2.05	2.12	5.7
Benzaldehyde	2.16	2.02	2.08	17.8

Table 3.4: The calculated local dielectric constant of frozen solvent molecule monolayers. The first column indicates the maximum of the effective dielectric constant for a range of rotations, the second column contains the corresponding minimum, the third column contains the average and the final column contains the experimental bulk dielectric constant of the solvents for the purpose of comparison [204, 205, 206, 207].

The free energy of mixing for graphene in all 10 solvents has been determined from molecular dynamics simulations using the finite difference thermodynamic integration method (FDTI), as described in Section 2.10. This will indicate the spontaneity of formation of the solvation structures presented in the previous section.

The results are shown in the first column of Table 3.5. At 300 K, ΔG_{mix} is always negative, irrespective of the solvent. It ranges from -11.08 MJ/mol for quinoline to -7.57 MJ/mol for cyclohexanone. This suggests the favorable solubility of monolayer graphene in each of the solvents. However, no correlation can be found between the magnitude of ΔG_{solv} and the experimentally-determined concentrations. As such, this cannot be used as a mechanism of screening for more effective solvents. Note that Oyer et al. calculated a change in the Helmholtz free energy upon graphene aggregation in various solvents to be in the range of 1 MJ/mol. This magnitude is consistent with the values reported here for the free energy of mixing of graphene in similar solvents[208].

The decomposition of the solvation energy into its enthalpic and entropic contributions are then given in the second and third column of Table 3.5, respectively. In all cases, except for bromobenzene, there is a significant entropic penalty for solvating graphene. This is because the bulk solvent molecules must rearrange to form solvation shells around graphene. The entropic penalty is compensated by a strong vdW interaction in all cases which results in a large

Solvent	ΔG_{mix} (MJ/mol)	ΔH_{mix} (MJ/mol)	$T\Delta S_{mix}$ (MJ/mol)
Cyclopentanone	-8.33	-24.07	-15.74
Cyclohexanone	-7.57	-22.26	-14.69
NMP	-10.172	-28.15	-18.01
Bromobenzene	-10.41	-9.57	0.83
Benzonitrile	-8.94	-21.98	-13.06
Chlorobenzene	-9.65	-23.10	-13.45
1,3-dioxolane	-9.22	-25.23	-16.0
Benzaldehyde	-9.90	-26.57	-16.64
Toluene	-8.99	-21.10	-12.07
Quinoline	-11.08	-28.32	-17.13

Table 3.5: The calculated Helmholtz free energy ΔG_{mix}, corresponding enthalpy ΔH_{mix} and the entropy term at room temperature $T\Delta S_{mix}$.

negative Helmholtz free energy of interaction. The solvation of graphene is most favourable in quinoline (ΔG_{mix} =-11.08 MJ/mol) followed by bromobenzene (ΔG_{mix} =-11.41 MJ/mol). However, the decomposition into enthalpy and entropy contributions in these two solvents are remarkable different.

The enthalpy change associated with the mixing of graphene in these solvents lies in a very narrow range between -28.32 MJ/mol (associated with quinoline) to -21.10 MJ/mol (associated with toluene). The exception is for graphene in a bromobenzene dispersion. In this case, ΔH_{mix} is much smaller in magnitude at -9.57 MJ/mol. Likewise, the entropy contribution ($T\Delta S_{mix}$) is very similar for all solvents, lying between -17.13 MJ/mol and -12.07 MJ/mol, except again for bromobenzene. The entropy contribution is here is positive at 0.83 MJ/mol. Overall, however, this unusual behavior of the bromobenzene solvent is not evident in the Helmoltz free energy of mixing.

Parameter matching - whether surface energies, Hildebrand solubility parameters or Hansen solubility parameters methods - works by minimizing the enthalpic contribution to the free energy of mixing. Poor predictability with this method in some specific cases was attributed to neglecting the entropic effects associated with interfacial interactions. Yet, here we show that there is a significant entropic contribution to the total free energy of mixing in all solvents, with the exception of bromobenzene.

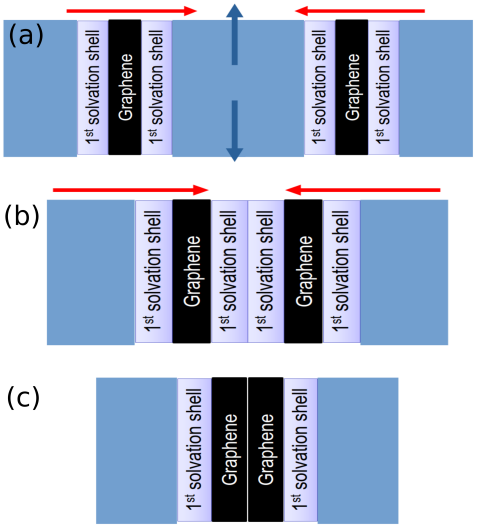

Figure 3.13: Simple model describing the process of reaggregation for two layers of graphene suspended in a solvent. (a) First, the isolated graphene layers move towards each other (indicated by red arrows) so that the molecules in between the layers are expelled (indicated by blue arrows), (b) the molecules in the first solvation shell then form a sandwich like structure in between the two graphene layers, and (c) Finally, the molecules in the first solvation shell diffuse from in between the layers completing the reaggregation process.

3.3.3.4 Dynamics of the First Solvation Layer

If the solvent-dependence of monolayer graphene stability in a dispersion is instead determined by re-aggregation effects, then solvent descriptors based on energetic considerations alone are not appropriate. Descriptors based on kinetic considerations, such as viscosity on the macroscopic scale, or diffusion of molecules on the nanoscale, should be considered.

For dispersions of graphene, long-term stability can only be obtained if the dispersion is kinetically stabilized against reaggregation when layer collision occurs. For this reason, surfactants or polymers are typically added to the dispersion. They adhere to the exfoliated sheets thereby preventing reaggregation. We hypothesize here that, in some cases, interactions between the graphene surface and the organic solvent molecules themselves may be sufficient to stabilize the graphene layers in solvent.

The re-aggregation of two neighboring graphene monolayers requires the solvent molecules between the two layers to be ejected. If the layers are far apart, this will be determined by the viscosity of the solvent [144]. When the layers are close together, the diffusion coefficient of the molecules parallel to the graphene sheet will determine the ease at which the molecules will be ejected. The molecules in

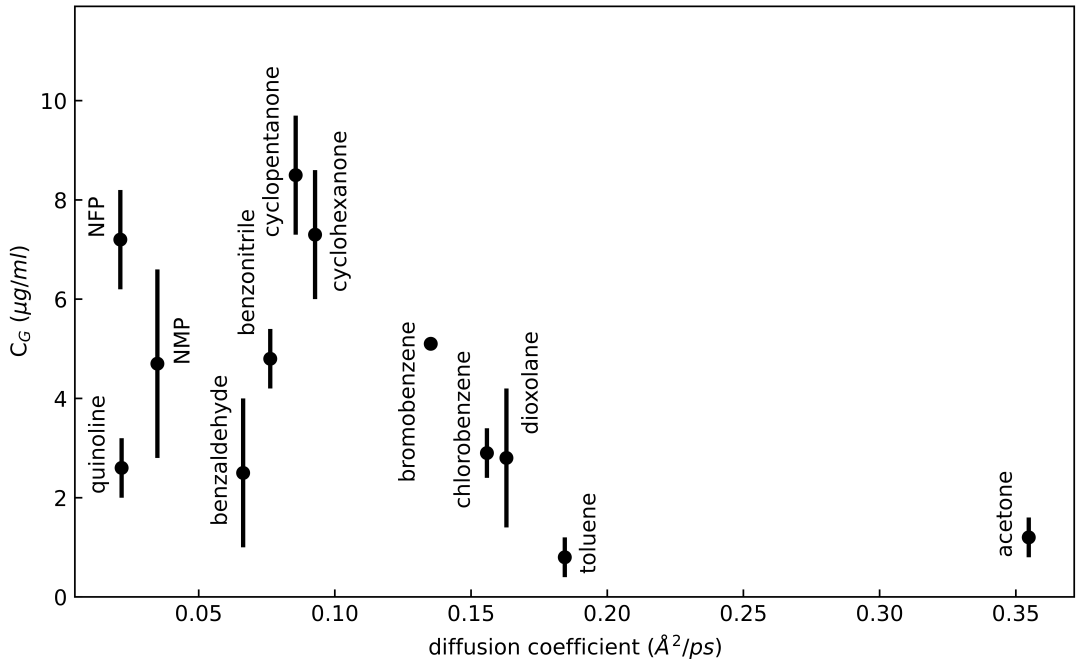

Figure 3.14: The diffusion coefficient of the molecules in the first solvation shell plotted against the concentration of graphene $C_G(\mu g/ml)$ in the solution.

the first solvation shell, confined as they are on the graphene surface, will play a particularly important role.

To visualize this, consider a slab of graphene layers suspended in a solvent. The solvent molecules around the layers form a solvation structure as shown in Fig. 3.13(a). This solvation structure can be divided into the first shell and the rest of the solvent molecules. For the graphene layers to reaggregate, the molecules in between these layers have to be ejected. This ejection can proceed in two steps: First, all the molecules in the rest of the solvation shells are ejected. This is illustrated in Fig. 3.13(a). This ejection of molecules results in the molecules in the first solvation shell sandwiched in between the graphene layers as shown in Fig. 3.13(b). Second. to complete the reaggregation process, those molecules in between the layers have to be ejected. This results in reaggregated layers suspended in the solution as shown in Fig. 3.13(c). If the solvent molecules are easily expelled from between two graphene layers, they will not hinder graphene reaggregation. This will lower the concentration of graphene in the dispersion.

To determine the extent to which the solvent molecules considered here can kinetically block reaggregation, we calculate the diffusion coefficient for the molecules in the first solvation shell in the direction parallel to the graphene

surface. The results are shown in Fig. 3.14 as a function of the experimental graphene concentration taken from Ref. [145]. The highest parallel diffusion coefficient is found for acetone, at 0.35 $Å^2$/ps. This is followed by toluene (0.18 $Å^2$/ps), dioxolane (0.16 $Å^2$/ps) and chlorobenzene (0.16 $Å^2$/ps). Interestingly, these are all poor solvents for the exfoliation of graphite, with the worst solvent corresponding to that with the largest parallel diffusion coefficient. As the diffusion constant decreases, the experimental concentration increases, with the best solvent (cyclopentanone) having a parallel diffusion constant of 0.085 $Å^2$/ps.

However, in the very-low diffusion regimen the concentration does not follow this upward trend. Here, the molecular hindrance to re-aggregation is higher, so one would expect that the exfoliated layers would remain in the dispersion and increasing stability would be found for solvents with lower diffusion coefficients parallel to the plane. Instead, the experimental concentration decreases again. It is possible that the actual concentration of graphene is now dependent on the ease of exfoliation.

To summarise, when the diffusion rate is high, the concentration of graphene layers in the solvent will decrease over time due to reaggregation. When the diffusion rate is low the concentration of graphene layers will be maintained due to a low reaggregation rate resulting in same graphene concentration at the beginning. In other words, when the diffusion coefficient is high the graphene concentration is always low due to higher rate of reaggregation, whereas when the diffusion rate is low, the graphene concentration will directly depend on number of layers that were initially present in the solution.

Experimentally, the solvent dependence of exfoliation can be inferred from the variation in the separation efficiency. This can be calculated as the percentage of monolayers in the exfoliated graphene slabs. Hernandez.et al. showed that the exfoliation in NMP results in 29% monolayers as compared to 7% in acetone and 5% in cyclopentanone [145].

To conclude, the diffusion coefficient calculated here a very good candidate for computational screening of the solvent molecules. In such a screening method, the diffusion coefficient of molecules can be calculated for a small set of molecules for which exfoliation experiment data is available. Comparing the two will then give an cut-off for the diffusion coefficient above which the solvent molecules will not perform well. This information can then be used to filter other molecules. We can then further identify solvent molecules for which the

graphene concentration will be enhanced by optimizing the separation process. For example, given that toluene has a high diffusion coefficient, it will result in low concentration dispersion even if larger amount of layers are initially created. Benzaldehyde, on the other hand, is a good candidate for the optimization of the separation process as it has a low surface diffusion coefficient.

In the analysis up until now, we have assumed that the separation is not affected by the solvent molecule due to the large forces involved. This may not be necessarily true, and in certain conditions is the most important consideration and needs further investigation.

3.3.4 Discussion

3.3.4.1 Non-zero Polar Hansen Solubility Parameter

The physical mechanism leading to the non-zero polar Hansen solubility parameters of non-polar graphene ($\delta_P = 9.3$ MPa$^{1/2}$) is so far unknown. There was some discussion in the literature regarding the contribution of edge-sites, but these should cancel to a large degree, leaving only unintentional chemical functionalisation of the basal plane as a potential physical mechanism [33]. Yet, Raman spectra typically find little evidence for this [209].

Here, we argue that rather than being assigned to monolayer graphene alone, the Hansen solubility parameters extracted from experimental data must be assigned to an effective solute, comprised of the graphene monolayer and its solvation shells, and in particular the first solvation shell. As our results show, these solvent molecules have a molecular-level structural and orientational ordering on the graphene surface.

The high non-dispersion components of the fitted solubility parameters must then be due to the dipole moment of the ordered solvent molecules. Due to this ordering, the effective solute, from a distance, appears to carry a net charge. For example, NMP orders in such a way that oxygen atoms are orientated away from the graphene sheet. The effective solute then appears to have a surface charge, resulting in the polar component of the assigned Hansen solubility parameter.

3.3.5 Conclusion

The solvent molecules near the surface of graphene re-organize into solvation shells. These solvation shells are formed such the first solvation shell is distinct

and is followed by a deep trough. The subsequent solvation shells are broader and decay rapidly away from the surface of the graphene layer. The number of solvation shells and the distance at which the last shell is formed varies in a very narrow range for all the molecules. The formation and the nature of the solvation shells is similar for all the considered molecules, irrespective of whether they are polar or non-polar.

Within the first solvation shell the molecules are organized in two distinct categories. These appear as two peaks in the position distribution function. The molecules associated with the first peak are adsorbed on graphene such that the plane of molecules is parallel to the graphene plane. The molecules associated with the second peak are oriented in such a way that the molecular plane lies perpendicular to the graphene plane. Some intermediate orientations can occur in some cases. This out-of-plane ordering is also seen in the orientation of the dipole moment of the molecules. In contrast to the strong out-of-plane ordering, the lateral ordering of these molecules is negligible. This is reflected in both the distributions of the molecular positions and their dipolar orientation. The molecules confined in the first solvation shell also have a drastically reduced dielectric permittivity. If they are immobilized due to surface confinement. This prevents the permanent dipole from aligning to an externally applied electric field.

The formation of these solvation shells is also favorable as indicated by the free energy and its decomposition in enthalpy and entropy contributions. This independence of the solvation structure on the nature of the solvent molecule hints that non energetic contributions may be responsible for the observed solvent-dependence of graphene stabilization. We propose that the diffusion coefficient of molecules in the first solvation shell is an appropriate property to determine the possibility of re-aggregation in a solvent. We note that in the low-diffusion limit, this appears to break-down, at least for the solvents investigated here. This origin of this requires further work, but could be related to the role of the solvent in the separation step which is typically thought to play a minor role.

We also speculate that the non-polar Hansen parameter obtained by fitting the experimental data can be attributed to the formation of solvation shells. The molecules in the first solvation shell and the graphene form an effective solute. Due to partial charges on the atoms of the first solvation shell, at a distance the effective solute appears to have surface charges. This results in the designation

of a non-zero polar solubility parameter.

CHAPTER

4

ION-ASSISTED EXFOLIATION

4.1 Introduction

An alternative strategy for the exfoliation of individual layers from their corresponding bulk structures is to use Group-1 metal ions, such as lithium or potassium, to accelerate the process [11, 35, 36, 37, 210]. This is known as ion-assisted exfoliation, and the effectiveness of this method is attributed to the charge transferred from the ions to the layers. It avoids the use of large forces to separate the layers, and the associated degradation of the exfoliated layers [211]. Ion-assisted methods generally involve introducing ions between the layers, followed by spontaneous exfoliation in presence of polar solvents.

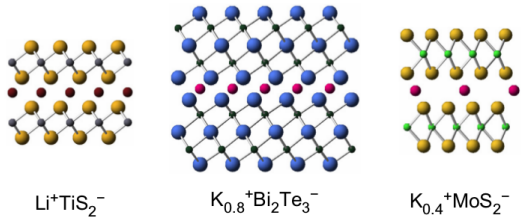

Figure 4.1: Layers intercalates with group-1 metal ions. (Left – Right) lithium intercalated TiS_2, potassium intercalated Bi_2Te_3 and potassium intercalated MoS_2. Figure reproduced from Ref. [35]

The intercalation of ions in a layered material is generally not a spontaneous process but it can be achieved via various methods. Fan et al. mixed n-butyllithium (BuLi) and MoS_2 in hexane at room temperature [36]. This was sonicated for 1.5 hours, resulting in Li intercalation between the MoS_2 layers. These intercalated layers were then separated from the mixture using centrifugation and exfoliated by sonicating the mixture of intercalated layers and water for 5 min. Cullen et al. mixed alkali metals and a variety of bulk layered materials such as MoS_2, TiS_2, FeSe and V_2O_5, in an environment of ammonia gas, at low temperatures of -63°C and at pressures of less than 10^{-6} mbar. This resulted in intercalated layers [35], as shown in Fig. 4.1. High temperatures can also be used to enhance intercalation. Wang et al. used a mixture of lithium salts and layered material in water at 100°C to achieve intercalation [210]. These intercalated layers can then be removed from the intercalating solvent mixture and used for exfoliation.

Cullen et al. also showed an interesting phenomenon for partially intercalated layers of Bi_2Te_3 [35]: High-angle annular dark field (HAADF) scanning TEM (STEM) found that these layers stack in a very particular way upon deposition. The adjacent few layer slabs are offset in such a way that the intercalation layer (positive) is adjacent to the negatively charged layer of Bi_2Te_3.

Wang et al. used salts such as Li_2SO_4 to achieve simultaneous cation-anion cointercalation [210]. They showed that the presence of the cation is critical for exfoliation. They propose that the simultaneous presence of anion species greatly accelerates the process of exfoliation and results in larger ratio of monolayer graphene layers [210]. They find that for this to occur, the geometry of the anion is important - similar enhancements are observed for KCl and not for LiCl.

Molecules, can also co-intercalate between graphite layers. In such cases the molecular structure plays a important role. This is demonstrated in case of ethylene carbonate (EC) and propylene carbonate (PC) electrolyte solutions [212]. In the case of PC, which differs in structure from EC by just a CH_3 functional group, molecule-ion cointercalation results in exfoliation of the graphite slab. In contrast, EC does not cointercalate and no exfoliation occurs.

Intercalating ions donate charge to the individual layers. In some cases this excess charge can modify the entire structural and electronic properties of the layered material. This is the case for alkali-metal intercalated group-VI transition

metal dichalcogenides (TMD) [11, 38, 39, 40, 41, 42], where the charge induces a structural phase transition from a semi-conducting H phase to a metallic T phase.

In Section 4.2 we show that the spontaneous disintegration of alkali-metal (specifically potassium) intercalated graphite is due to an enhanced solvation energy of the now-charged graphene layers. In Section 4.3 we discuss the changes to the structural and electronic properties of group-VI transition metal dichalcogenides (TMD) that occurs due to the presence of excess charge. Finally, in Section 4.4 we develop a computational methodology to determine whether selective ion intercalation, selective molecule intercalation or molecule–ion co-intercalation will occur when a layered material is placed in a solvent containing alkali metal-ions.

4.2 Ion-assisted Liquid Phase Exfoliation

Some graphene intercalation compounds have been shown to spontaneously exfoliate when mixed with a polar solvent [11, 35, 36, 37, 210]. This spontaneous disintegration is desired as it avoids the fragmentation of the slabs which occurs with the introduction of shear forces in the LPE method. The spontaneity of this process and the final product of the disintegration can be estimated by calculating the binding energy of the intercalated slabs in a solvent medium. A positive binding energy indicates an unstable structure which will spontaneously exfoliate releasing energy. A negative binding energy indicates a stable structure which will not spontaneously exfoliate.

4.2.1 Disintegration into neutral slabs

Experimental evidence suggests that for a potassium-intercalated slab of graphite, the exfoliation in polar solvents is spontaneous and results in charged layers [35]. First we determine if this is the only possibility or if exfoliation into neutral layers is also possible. For this we calculate the binding energy of a potassium intercalated graphene bilyer as shown in Fig. 4.3(a). Here, we use the potassium concentration of KC_6 as this is one of the highest concentrations that can be achieved experimentally [213]. Higher concentrations such as KC_4 require extreme conditions [214].

Here, the DFT calculations were performed with VASP, using the additional module VASPsol [83, 84] to account for implicit solvent interactions. A description of the implicit solvation method is given in Section 2.8. The Brillouin zone was sampled with a $11 \times 11 \times 1$ $\Gamma-$centered mesh. The unit cell is hexagonal with the in-plane unit cell size of size 4.29 Å $\times$ 4.29 Å. We allow all atoms in the unit cell to move. In all cases, a plane wave cutoff of 700eV was used to converge the basis set.

In vacuum, the potassium intercalated graphene bilayer is stable. This is confirmed by a negative binding energy of -1.6 eV associated with the slab exfoliating into two neutral monolayers and isolated potassium atoms. It is defined as:

$$E_{BE} = E_{2L+K} - E_{1L} - E_{1L} - E_K \tag{1}$$

where, E_{BE} is the binding energy of the intercalated graphene bilayer, E_{2L+K}

is the total energy of the intercalated graphene bilayer, E_{1L} is the total energy of a graphene monolayer and E_K is the total energy of an isolated potassium atom.

From experiment, we know that alkali-metal intercalated graphite is exfoliated upon immersion in a polar solvent [11, 35, 36, 37, 210]. We therefore calculate the binding energy, E_{BE}, of an intercalated bilayer slab in an implicit solvent environment as a function of the relative permittivity (ϵ_r) and surface tension (τ) of the solvent. The results are showed in shown in Fig. 4.2. The Coulombic interaction between the solvent molecules and the layer (solute) is included in the relative permittivity term, which fixes the charge density and the boundary between the solute and solvent. The surface tension term accounts for the other non-electrostatic contributions. These contributions are dependent on the boundary between the solute and the solvent. As a result, when we increase the surface tension, the binding energy increases linearly for a fixed relative permittivity (ϵ_r). We find a negative binding energy for all values of ϵ_r and τ, so that exfoliation into neutral graphene monolayers and isolated potassium methods is not energetically favorable, regardless of the solvent parameters.

4.2.2 Disintegration into charged slabs

Next we consider a process where the neutral slab disintegrates into charged products, i.e., into isolated monolayer anions and a isolated potassium cation. The description of anions in DFT must be performed carefully for two main reasons: (1) In VASP a negatively charged system can converge to a state in

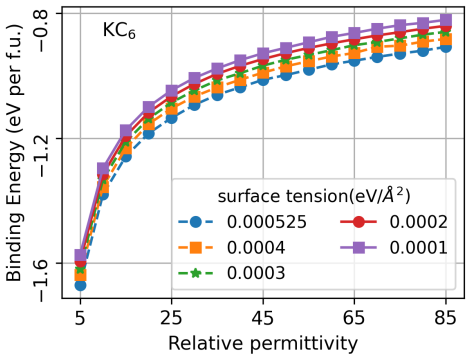

Figure 4.2: Binding energy of KC_6, calculated according to Eqn. 1, as a function of the relative permittivity of bulk solvent (ϵ_r) and the surface tension of the solvent (τ).

which positive eigen-values are occupied - an unconverged result [215], and (2) the linear term in periodic corrections for 2D systems is not implemented. The effect of a polarization charge is also neglected. This leads to charge leakage into the solvent in VASP. Instead, we use QUANTUMESPRESSO to perform DFT calculations in this section with the additional plugin Environ[87] to account for solvent interaction. This choice was motivated by the fact that this code has implemented suitable periodic boundary conditions for the solvent potential [86].

As polar solvents are required to screen the excess charge on the graphene sheet, this gives a lower bound of the relative permittivity. Here, we consider only $\epsilon_r > 20$. We consider a few different experimentally relevant concentrations for potassium intercalated bilayers. Cullen et al. achieved a concentration of KC_{24}, so here we consider concentrations KC_{12}, KC_{24}, KC_{16} and KC_{32}, to test the robustness of the analysis to changing concentrations [35]. The unit cell for KC_{12} and KC_{24} is hexagonal with an in-plane unit cell size of 8.58 Å × 4.29 Å and 8.58 Å × 8.58 Å respectively, whereas for KC_{16} and KC_{32} it is orthorohombic with an in-plane unit cell size of 8.52 Å × 4.92 Å and 8.52 Å × 9.84 Å respectively. Furthermore, a vacuum layer of 20 Å was included in the direction normal to the surface. In all cases, a plane wave cutoff of 75 Ry was used to converge the basis set. This high cutoff is required to resolve the cavity, which has a very sharp gradient. The PBE-PAW potentials provided with the pslibrary.1.0.0 were used. These potentials were tested by reproducing common properties of graphene and bulk potassium. The optimized optB86b-vdW functional was used. The Brillouin zone was sampled with a $6 \times 11 \times 1$ $\Gamma-$centered mesh for KC_{12} and KC_{16}, whereas for KC_{24} and KC_{32} a $6 \times 6 \times 1$ $\Gamma-$centered mesh is used. For structural relaxations a force tolerance of 3.88×10^{-4} Ry/Bohr is used. We allow all atoms in the unit cell to move. The point counter charge correction for 2D slabs was used for the monopole and dipole correction.

Fig. 4.3(a) shows a schematic of the potassium intercalated bilayer graphene. Fig. 4.3(b) shows the solvation energy of positively charged potassium ions. This energy decreases for higher values of ϵ_r due to increased Coulomb interaction between the charged atom and the solvent. Fig. 4.3(c) shows the binding energy for a potassium intercalated bilayer graphene slab with concentration KC_{12} as a function of the relative permittivity (ϵ_r) and surface tension (τ) of the solvent. To calculate this binding energy the intercalated slab is split into an isolated positively charged potassium and two isolated monolayers of graphene each with

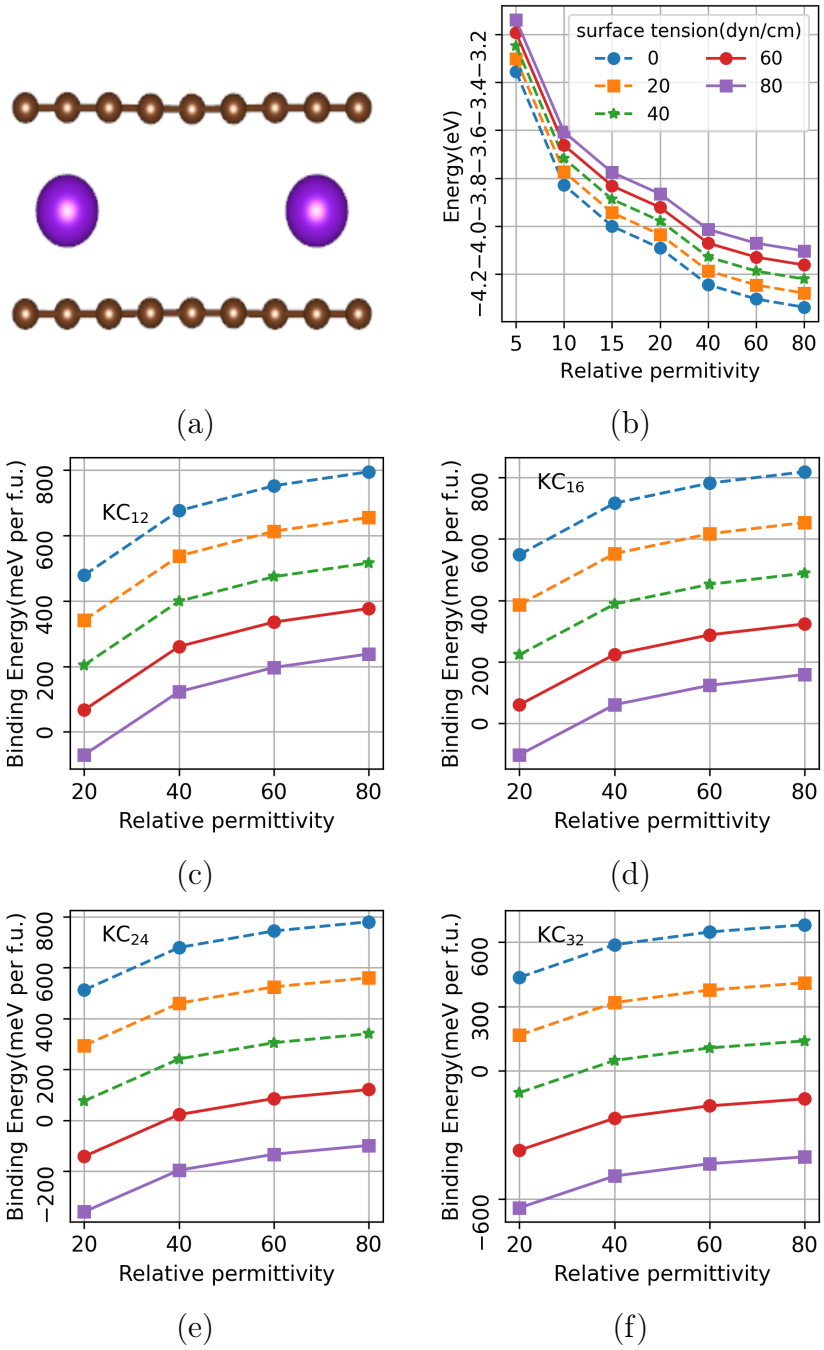

Figure 4.3: (a) Schematic of a graphene bilayer intercalated with a potassium atom, (b)The solvation energy of a positively charged potassium ion as a function of the relative permittivity of bulk solvent (ϵ_r) and the surface tension of the solvent. Binding energy of graphene intercalated with potassium(K) atoms. Binding energy is calculated for case when the 2-layer intercalated slab breaks into positively charged potassium ion and two negatively charged monolayers each with a total excess charge of 0.5 electron. The binding energy is calculated as a function of both relative permittivity of bulk solvent (ϵ_r) and the surface tension of the solvent with varying ion concentration, (c)KC_{12}, (d)KC_{16}, (e)KC_{24}, (f)KC_{32}; the common legend is given is (b)

half an extra electron per 12 carbon atoms. That is, the binding energy is defined as:

$$E_{BE} = E_{2L+K} - E_{1L^{0.5-}} - E_{1L^{0.5-}} - E_{K^+} \tag{2}$$

where, E_{BE} is the binding energy of the intercalated graphene bilayer, E_{2L+K} is the total energy of the intercalated graphene bilayer, $E_{1L^{0.5-}}$ is the energy of monolayer graphene with an excess charge of 0.5e on the layer and E_K is the energy of a positively charged potassium ion. A positive binding energy (E_{BE}) indicates a spontaneous splitting of the graphene bilayer into two charged monolayers without the application of external forces.

For a fixed value of ϵ_r, increasing τ results in a much reduced or even negative binding energy. This is because the energy gained as a result of the Coulomb interaction between the charge density of the solute and polarization charge of the solvent (dictated by ϵ_r) is used to create a cavity in the solvent. This can be seen from the rigid shift of isolines downwards with increasing τ in Fig. 4.3(c).

However, for a fixed value of τ, increasing ϵ_r will result in an increased binding energy. This is because increasing ϵ_r results in a higher polarization charge of the solvent, which results in a higher Coulomb attraction between it and the charge density of the solute. This increase in attraction will be higher for the charged solutes than for the neutral solutes. This can be seen from the monotonic increase of the isolines going from left to right in Fig. 4.3(c) with increasing ϵ_r.

When decreasing the concentration of adsorbed potassium from KC_{12} to KC_{32} (shown in Fig. 4.3(f)), the energy required to create the cavity for a fixed τ increases because of the larger overall quantum volume. As a result, a higher Coulomb attraction compensates for this increase in energy. This results in a much reduced or even negative binding energy for same value of ϵ_r and τ compared to the system with a higher potassium concentration. The binding energies for intermediate concentrations KC_{16} and KC_{24} are shown in Fig. 4.3(d) and Fig. 4.3(e), respectively.

We can therefore conclude from Fig. 4.3 that a spontaneous splitting of an intercalated bilayer graphene into charged species will be achieved for higher potassium ion concentration in the intercalated slab, for higher relative permitivities of the bulk solvent (ϵ_r) and lower surface tensions (τ) of the solvent. The spontaneous splitting of these intercalated slabs into individual

layers of graphene suspended in the solvent without the introduction of external forces is advantageous because the application of external forces can damage the exfoliated layers, with the amount of damage proportional to the applied force [216]. This damage is often observed as defects or a reduced surface area of separated layers.

The solvation energy is defined as an energy gain or loss as a result of solute-solvent interaction. It is calculated as:

$$E_{\text{solvation}} = E_{\text{in solvent}} - E_{\text{in vacuum}}$$

where $E_{\text{in solvent}}$ is the energy of the solute in solvent and $E_{\text{in vacuum}}$ is the energy of solute in vacuum. As we cannot calculate the energy of anions in vacuum[85], due to problems associated with charge leakage, we cannot calculate the exact *ab-initio* solvation energy of the individual charged graphene layers. However, from the solvation energy of the positively charged potassium, shown in Fig. 4.3(b), and the binding energy, we can conclude that the solvation energy of the negatively charged slab will be very large compared to a neutral slab. These large solvation energies associated with both charged species is responsible for the spontaneous exfoliation of the intercalated slabs: the exfoliated charged products are better stabilized than the neutral parent slab. The charge on the monolayers also prevents the re-aggregation of the individual layers due to Coulomb repulsion.

We note that the case considered here required the bilayer slab to disintegrate into charged slabs, but this may not be necessary in other cases when the solvation energy of the neutral disintegrated products is large enough to compensate for the binding energy.

4.2.3 Conclusion

The experimentally observed spontaneous disintegration of intercalated layered materials into their charged components can be explained by the large solvation energy of charged species. The increase in binding energy of the intercalated slabs compared to non-intercalated slabs can be countered by this solvation energy.

4.3 Phase transitions in group-VI transition metal dichalcogenides

The charge donated by the group-1 metal ions to the layers can have unintended consequences, such as a modification of electronic or structural properties of the exfoliated layers. Achieving control over these modifications is desirable.

Transition metal dichalcogenides (TMDs), comprised of layered sheets of transition metal atoms sandwiched between two layers of chalcogen atoms (MX_2), are chemically versatile, exhibiting a broad range of electronic properties from insulating (ZrS_2) to superconducting ($NbSe_2$) [217]. As well as by changing the composition, the conductivity of a TMD can be modified by inducing a structural transition between different polymorphs. Several such polymorphs exist, distinguished by the metal coordination of the chalcogen atoms. In the semi-conducting H phase, the chalcogen atoms are AA-stacked so that the metal atoms occupy alternate trigonal-prismatic voids. The metallic T phase, on the other hand, has a tetragonal symmetry, with the metal atoms occupying octahedral voids between AB-stacked chalcogen atoms. This particular phase can transform to a semi-metallic distorted octahedral phase, designated here T′. Recently, a further mixed phase, designated T″, which can be viewed as a series of alternating H and T′ phases, was theoretically predicted to be lower in energy than the T′ phase for MoS_2 [218].

The ability to induce a transition in MoS_2 from its ground state H phase to an octahedral phase via alkali metal intercalation has been known since the 1980s [40]. This phase transition was attributed to a transfer of charge from the intercalated atom to the TMD, and more specifically to the d states of the transition metal atom [219, 220]. Indeed, the entire family of group-VI TMDs, where M = Mo, W and X = S, Se and Te, can be manipulated to undergo phase transitions close to ambient conditions [38]. This has been achieved using a variety of methods, including alkali metal adsorption [39, 40, 41, 42], the introduction of impurities or vacancies [221, 222, 223], electron or laser irradiation [36, 222, 224, 225, 226, 227] and electrostatic gating [228, 229].

The electronic properties of a TMD are evidently strongly dependent on its structural phase. In MoS_2 the conductivity of the T phase was found to be up to 10^7 times higher than that of the semiconducting H phase [230]. The ability to reversibly and reliably switch between these two phases would result in applications as monolayer-thick field effect transistors [231], gas sensors [232]

and catalysts [233]. Such applications require precise control over the phase transition process so that a complete phase change to T′ phase can be achieved and maintained.

Liquid phase exfoliation, with the aid of alkali metal intercalation, is a common and effective way of isolating TMD monolayers from the bulk on an industrial scale. In such experiments, the alkali metal atoms are first intercalated into the bulk TMD using an organolithium compound. The intercalated TMD is then solvated in a polar solvent. This results in the discharging of the monolayers, the deintercalation of the metal ion and the exfoliation of individual monolayers from the bulk materials. These layers are subsequently measured to have both H and T phases present.

Of the group-VI TMDs, the phase transition in MoS_2 has been investigated in detail. Yet, compared to other group-VI TMDs, the phase transition efficiency in MoS_2 can be relatively low: a comprehensive side-by-side comparison of the experimental transition efficiency in four group-VI TMDs – MoS_2, $MoSe_2$, WS_2 and WSe_2 – found that WS_2 exhibited the largest increase in the proportion of the 1T phase compared to the starting 2H phase (i.e., the 1T/2H ratio), followed by $MoSe_2$ and WSe_2, and eventually MoS_2. [11] While the exact ratios were subsequently found to depend on the nature of the organolithium intercalant group used in the experiment, the general trend remained: WX_2 compounds display a higher proportion of T phase compared to MoX_2, for both X = S and Se [12, 234].

In these alkali metal induced exfoliation experiments, the measured phase transition efficiency will depend not only on the intrinsic composition-dependent free-energy barrier between the different phases, but also on the composition-dependent exfoliation efficiency of the chosen organolithium intercalant. Experimentally, it is difficult to decouple these two contributions. As ion-assisted liquid phase exfoliation is the most suitable method of producing sufficient T phase TMDs on an industrial scale, a complete understanding the mechanism is essential to maximize the amount of metallic phase produced and to prevent a transition back to the H phase.

Previous computational investigations of the phase transition barrier have concentrated on MoS_2, looking primarily at the threshold charge density required to induce the phase transition. However, a disconcertingly wide range of values have been reported, including 0.35 e per formula unit (f.u.) [235], 0.55 e per f.u. [218], 0.78 e per f.u. [236] and almost 2 e per f.u. [237]. The

origin of this discrepancy is discussed in detail in Section 4.3.3

Here, using first-principles calculations, we determine the transition barriers between all possible polytypes of both the pristine and Li-adsorbed group-IV TMDs, with the aim of determining whether the composition dependence of experimental transition efficiency in four group-VI TMDs can be explained using the intrinsic barriers to the phase transitions alone.

4.3.1 Computational Methods

Density functional theory (DFT) calculations were performed using the VASP-5.4 code [63, 162, 163]. The optB86b-vdW exchange-correlation functional was used to account for long range dispersion interactions [77, 82]. This functional was previously shown to give accurate lattice parameters and energies for layered materials [81, 187]. All calculations are performed with a cutoff energy of 500 eV for the plane wave basis set. A Γ centered K-point grid of $11\times7\times1$ is used to calculate the total energy of the H and T$'$ phases, while a $11\times5\times1$ grid is used for the T$''$ mixed phase.

The structures were relaxed until the force on each atom was less than 0.01 eV/Å. The unit cell length in the direction normal to the plane was fixed at 25 Å for H and T$'$ phase calculations, and 26 Å for T$''$ mixed phase calculations and all transition state calculations. This corresponds to a minimum vacuum of 18 Å between repeating monolayers and dipole corrections were applied.

Transition states are determined using the climbing image nudged elastic band (CI-NEB) method [96, 238] with a spring constant of 5 eV/Å. The CI-NEB is used to determine the transition barrier between two different phases. The transition barrier is determined by a constrained geometry optimization of a series of interpolated structures between the stable phases connected by springs. The structure with highest energy after optimization determines the transition barrier. The role of the spring is to prevent the interpolated structures from converging to the nearest stable phase. All atoms in the transition state calculations are optimized so that the force on each atom is less than 0.05 eV/Å.

4.3.2 Neutral Monolayers

The crystal structures of the H, T$'$ and T$''$ mixed phases are shown in Fig. 4.4. The structural parameters determined for all neutral monolayers (without adsorbed

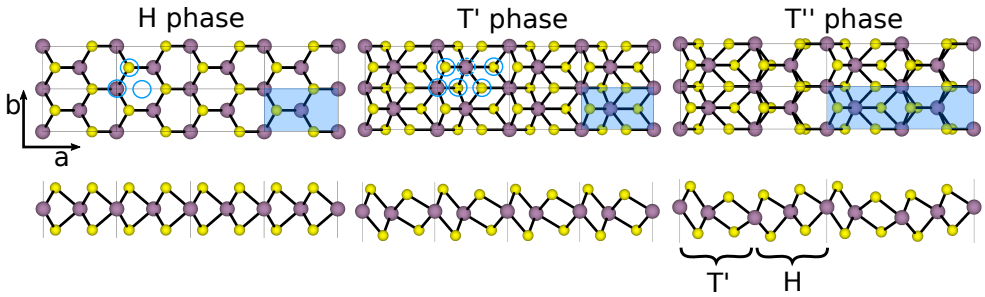

Figure 4.4: Top and side view of the H, T′ and T″ polytypes. The orthorhombic cells of all three phases are shown as blue shaded regions. Note that the T″ mixed phase can be viewed as alternating T′ and H phases. The blue circles indicate the possible candidate sites for lithium adsorption.

	H		T′		T″	
	a	b	a	b	a	b
MoS_2	5.48	3.16	5.57	3.22	11.23	3.16
$MoSe_2$	5.71	3.30	5.79	3.34	11.69	3.27
WS_2	5.48	3.17	5.59	3.23	11.24	3.18
WSe_2	5.71	3.30	5.81	3.35	11.69	3.28

Table 4.1: The lattice parameters a, b (in Å) of the H, the T′, and the T″ mixed phase of MoS_2, $MoSe_2$, WS_2 and WSe_2.

Li) are given in Table 4.1. The lattice constants are dictated by the chalcogen atom, with MoS_2 and WS_2 having very similar values in all three phases. Likewise, $MoSe_2$ and WSe_2 have almost identical lattice constants. These values are in good agreement with the available experimental data [239, 240, 241, 242, 243, 244, 245, 246, 247, 248] and with previous calculations[249, 250, 251, 252] in the literature. For the T′ phase, the calculated *a* lattice constant of 5.57 Å for MoS_2 is consistent with the experimentally observed length of 5.6 Å.

In agreement with previous DFT studies, we find the H phase to be the ground state structure for all four materials[222, 229, 236, 237, 253, 254, 255]. The total energy differences between this phase and both the T′ phase and the T″ mixed phase are given in Fig. 4.5. We find that the energy difference between the H phase and the T′ phase is larger for the sulphides compared to the selenides. It reduces from 0.57 eV for MoS_2 to 0.35 eV for $MoSe_2$ and from 0.56 eV for WS_2 to 0.29 eV for WSe_2. Similarly, the energy difference between the H phase and the T″ mixed phase reduces from 0.49 eV for MoS_2 to 0.35 eV for $MoSe_2$ and from

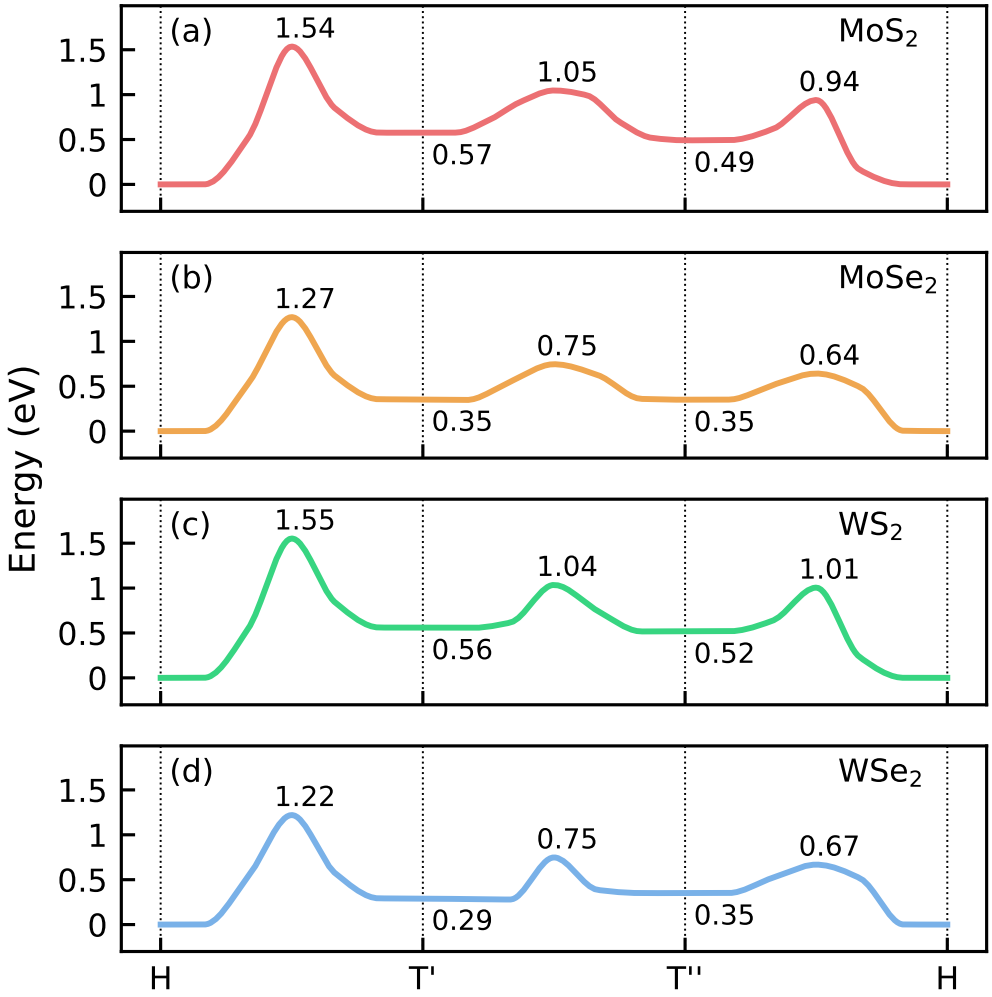

Figure 4.5: The relative energy difference and transition barrier between the H phase, the T′ phase and the T″ mixed phase of (a) MoS_2, (b) $MoSe_2$, (c) WS_2 and (d) WSe_2. Energies are referred to that of the H phase for each material.

0.52 eV for WS_2 to 0.35 eV for WSe_2. While the H phase is the ground state in all four cases, the T′ phase is energetically more favourable than the T″ mixed phase for WSe_2 but the ordering is opposite for the MoS_2 and WSe_2 (the difference is negligible for $MoSe_2$).

The band structures of these materials in all three phases are shown in Fig. 4.6. The opening of a band-gap in the H phase is due to a mixing of the p_z orbitals from the top and bottom chalcogen atoms at K-point of the hexagonal Brillouin zone [219]. We find a bandgap of 1.74, 1.50, 1.90 and 1.62 eV for MoS_2, $MoSe_2$, WS_2 and WSe_2, respectively, in good agreement with previous calculations in the literature [256, 257]. The band gaps for the MSe_2 compounds are smaller compared to the corresponding MS_2 compounds. As a result of the AB-type stacking of the chalogen atoms in the T phase, this particular p_z interlayer mixing

is absent, and the band-gap closes. The distortion of the T phase to produce the T′ phase facilitates in part this interaction again, so that the resulting phase is semimetallic [219](The inclusion of spin-orbit coupling opens a small band gap. [258]) The relative energy ordering of the H and the T′ phase is driven by this interlayer interaction.

The alternating H (insulating) and T′ (metallic) stripes in the T″ phase (cf. Fig. 4.4) produces an effective one-dimensional (1D) quantum well structure, with flat bands evident perpendicular to the direction of confinement (here, along Γ – X). This confinement causes the overlapping energy levels in the T′ phase to split, opening a small band-gap of 0.27, 0.29, 0.05 and 0.25 eV for MoS_2, $MoSe_2$, WS_2 and WSe_2, respectively, in good agreement with the previous calculations of Ma et al. [218]. The formation of these 1D quantum wells causes the T″ phase to be lower in energy than the T′ phase for MoS_2, $MoSe_2$ and WS_2.

The activation barriers to induce a phase transition from the H phase to the T′ and T″ mixed phases, as calculated with the CI-NEB method, for all four materials are also shown in Fig. 4.5. In all cases, the energy barrier to transition directly from the H phase to the T′ phase is large, ranging between 1.22 eV and 1.54 eV. In general, the barrier is smaller for MSe_2 than for MS_2. The energy barrier to transition from the H phase to the T″ mixed phase is smaller, ranging between 0.64 eV and 1.01 eV. Again, the smallest values occur for the MSe_2 compounds. In all cases the energy barrier to transition from the ground state H phase to the lowest-lying T phase (namely, T″ for MoS_2, $MoSe_2$ and WS_2, and T′ for WSe_2) lies between 0.64 eV and 1.22 eV. Evidently, the H phase is very stable and will not convert to the T phase spontaneously, in agreement with experiment. Note that the transition from the T′ phase to the T″ mixed phase requires the conversion of only half of the lattice from the T′ phase to the H phase while keeping the other half fixed. Consequently, the barrier to transition from the T′ phase to the T″ mixed phase is lower (by between 50 and 65%) than the barrier to undergo the complete transition from T′ phase to the H phase.

The calculated barriers reported here are in units of eV per formula unit (MX_2) to facilitate comparison between four materials and the total activation energy required for transition will scale with the number of formula units which transition simultaneously [227]. Note that the phase transition between the H phase and the T phase was shown to be diffusive, rather than a simultaneous phase transition of the entire monolayer. As a result, the activation barrier per f.u. will be modified by the exact details of the nucleation process.

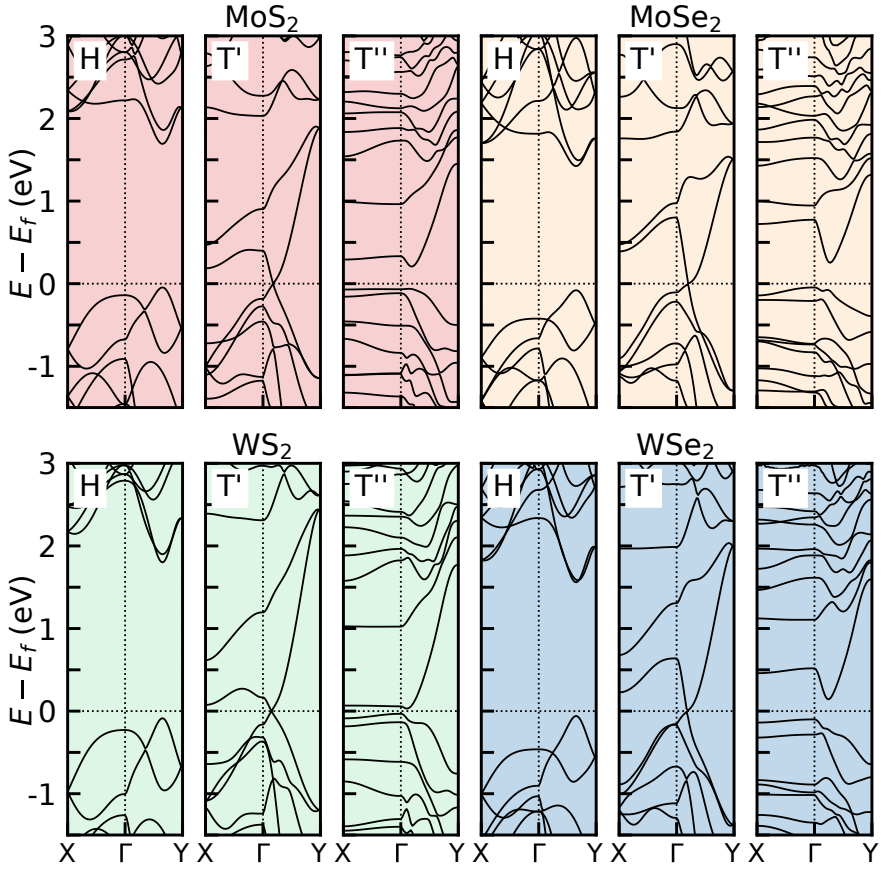

Figure 4.6: The band structure of the H, T′ and T″ phases of MoS_2, $MoSe_2$, WS_2 and WSe_2.

4.3.3 Implicit Charging

We highlight here some issues related to statically charging monolayers or slabs in DFT with periodic boundary conditions, as it is to these issues that we attribute the wide range of values reported in the literature for the critical charge required to induce a structural phase transition in TMDs.

For the case of isolated charged slabs, such as the TMD monolayers considered here, the electric field due to the extra uniform charge density is constant and should result in potential that varies linearly with distance from the surface of the slab. When periodic boundary conditions are implemented, this linear potential is replaced by the combined effective potential due to the consecutive periodic images. The quantities relating to the isolated slabs can be recovered from these periodic calculations by applying a correction term to the effective potential and total energy. The exact functional form of this potential is discussed in detail by Andreussi at al. [86] As discussed in manual for VASP (in the section Monopole, Dipole and Quadrupole corrections) the leading term of this correction, which

cancels the interaction of the linear potential with the background compensating charge, is absent. As a result, the total energy is essentially incorrect and cannot be relied upon.

Furthermore, we find that above a certain critical charge, positive eigenvalues are occupied. The occupation of positive eigenvalues could be due to the ambiguous reference energy for periodic DFT calculations or due to self-interaction error as was previously shown to occur for atomic anions [215].

Finally, Topsakal et al. showed that, when the basis set is present in the vacuum region, excess negative charge does not stay on the slab but spills over in the vacuum, beyond a critical value which depends on the vacuum thickness [259]. This phenomenon is demonstrated in Fig. 4.7(a) for the H phase of MoS_2 with a vacuum length of 25 Å perpendicular to the surface of the slab and was previously shown for graphene [260]. The excess charge density added is placed in the vacuum and on the outer faces of the monolayer rather than on the *d* orbital of the metal atom.

To illustrate how these issues affect the determination of the critical charge required to induce a structural phase transition, we show in Fig. 4.7(b) the total energy difference between the H and the T′ phase of MoS_2 as a function of excess charge, and for two different vacuum lengths. All three sources of error are now present, namely charge has spilled into the vacuum (above a certain critical excess charge value), the appropriate monopole correction is absent and positive eigenvalues are occupied. We find that the vacuum length of 15 Å (blue squares) shows a phase transition for excess charge of around 0.5 e per f.u. On increasing the vacuum length to 25 Å (orange circles) no such transition is observed.

Clearly, it is not possible to get physically meaningful results using statically charged slabs combined with periodic boundary conditions using the current implemetation of VASP (V5.4.1). A similar erroneous dependence on the vacuum length was also reported by Bal et al. for adsorbed molecules on charged surfaces, further highlighting the irreproducibility of such results[261]. These problems can be mitigated by applying correct boundary conditions when calculating the Hartree potential[91, 92, 97, 98, 262], e.g., by applying open boundary conditions in the direction perpendicular to the slab while keeping the periodic boundary conditions in the plane of the slab.

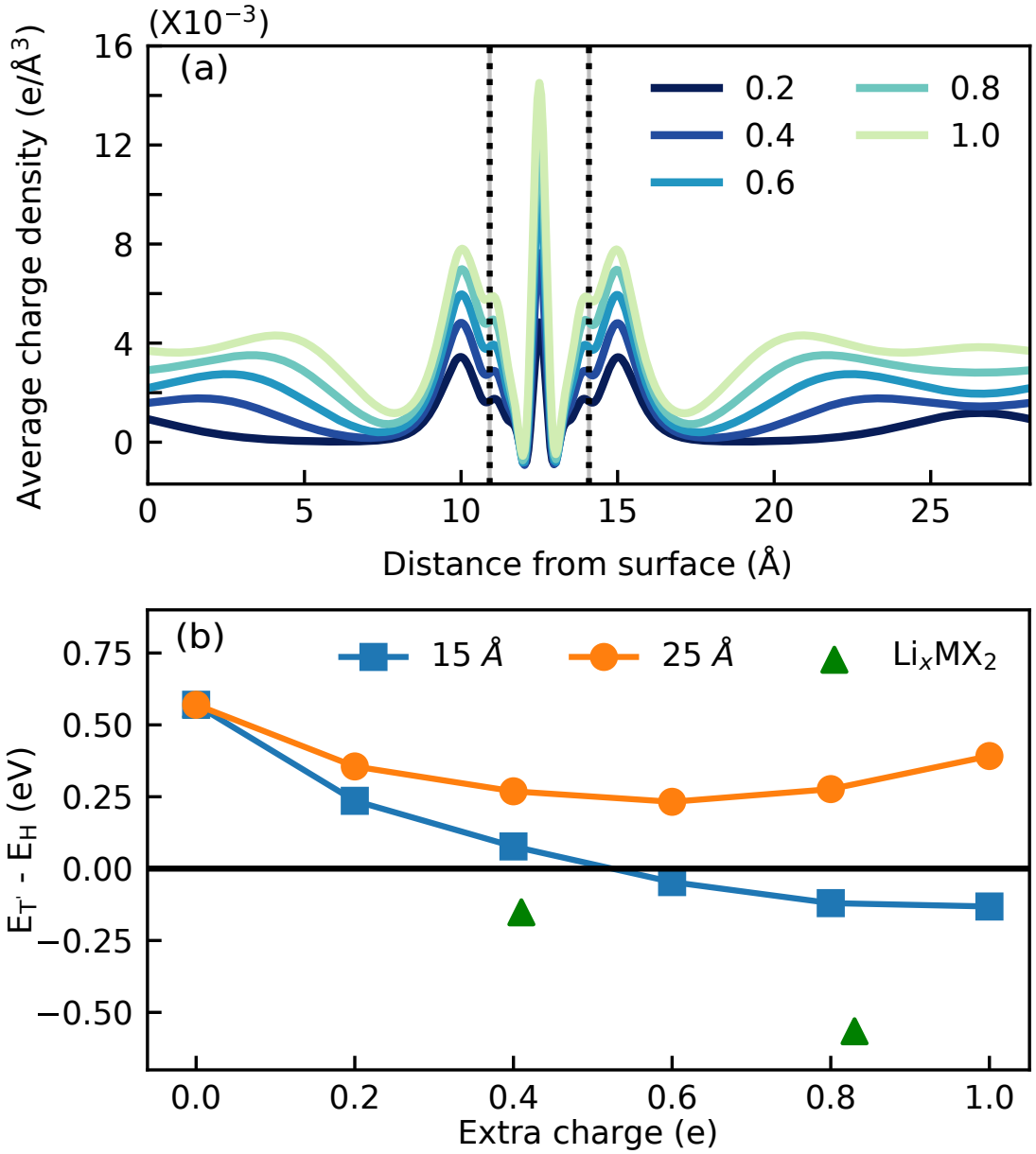

Figure 4.7: (a) Planar average of the charge density across the TMD monolayers showing charge leakage into the vacuum region for typical values of excess charge. The positions of the chalcogen atoms are marked by black dashed lines. (b) The energy difference between the T′ and the H phase of MoS_2 as a function of excess static charge for two different vacuum thickness, compared to the values found by explicitly charging the slab using Li atoms.

4.3.4 Charged Monolayers

Introducing extra charge to the TMD via an interaction with explicitly-modelled strong donor atoms bypasses these issues related to static charging. We consider two different concentrations of Li atoms adsorbed on the surface of the monolayers, namely $Li_{0.5}MX_2$ and Li_1MX_2. The stability of the

alkali metal-adsorbed monolayer decreases at higher concentrations, and eventually becomes unstable for $Li_{1.5}MX_2$, in agreement with experiment.[263, 264, 265]

The adsorption sites were determined by calculating the total energy of lithium adsorbed on all of the unique candidate sites, shown as blue circles in Fig. 4.4. These sites include those directly on top of the metal atom, on top of the chalcogen atoms and on the hollow site. In agreement with previous calculations in the literature [266], we find that irrespective of the material or phase the lowest energy adsorption site is on top of the metal atom (The preferred adsorption position on the T′ phase is shown with a dashed circle in Fig. 4.4). When increasing the Li concentration to $LiMX_2$, the second Li atom per unit cell adsorbs on the opposite surface, minimizing the electrostatic interaction between the two Li atoms. This configuration is 0.1 eV per formula unit lower in energy than that with both Li atoms adsorbed on the same side of the monolayer. For the case of the T″ mixed phase, the lithium atoms are also positioned on top of the metal atoms. For $Li_{0.5}MX_2$, one lithium atom is placed in the H phase region and another in the T′ phase region. For Li_1MX_2, the remaining lithium atoms were placed on top the metal atoms on the opposite side of the slab. The adsorption on opposite surfaces is consistent with a uniform intercalation in the bulk material[36].

The extra charge introduced by the Li atoms causes an expansion of the TMD lattice constants. These values are given in Table 4.2. A Li concentration of $Li_{0.5}MX_2$ increases the lattice constants of the H phase by between 0.3 and 1.75% compared to the neutral lattice. Similarly, Li adsorption increases the lattice constants of the T′ phase by between 9% and 3.23%. Increasing the lithium concentration causes the lattice to expand further, and the expansion is higher in the selenides compared to the sulfides. Bader charge analysis [171] finds that, for both concentrations considered here, each Li atom donates approximately 0.82 electrons per formula unit. This value is independent of the material type and phase, indicating that the nature of the interaction is similar.

The energy differences between the different polytypes, for all four compounds and for both Li concentrations, are summarized in Fig. 4.8. The T′ phase becomes the ground state structure of all four Li-adsorbed TMDs. This is followed by the H phase and finally the T″ mixed phase. This is in agreement with previous studies on MoS_2 which have shown a phase transition to occur at a Li concentration of $Li_{0.4}MoS_2$[267], a K concentration of $K_{0.225}WSe_2$[42] and a Na concentration of $Na_{0.375}MoS_2$[264].

		H		T′		T″	
	Å	a	b	a	b	a	b
$Li_{0.5}MX_2$	MoS_2	5.53	3.19	5.75	3.25	11.49	3.20
	$MoSe_2$	5.8	3.32	6.	3.37	11.95	3.34
	WS_2	5.51	3.18	5.74	3.26	11.47	3.19
	WSe_2	5.81	3.29	5.97	3.4	11.90	3.33
$LiMX_2$	MoS_2	5.68	3.23	5.9	3.29	11.79	3.22
	$MoSe_2$	5.98	3.36	6.12	3.46	12.2	3.38
	WS_2	5.98	3.36	5.88	3.27	11.72	3.19
	WSe_2	5.94	3.33	6.06	3.47	12.30	3.33

Table 4.2: The lattice parameters a, b (in Å) of the H, the T′, and the T″ mixed phase of $Li_{0.5}MX_2$ and $LiMX_2$ in the orthorhombic unit cell.

The energy difference between both the T′ and T″ mixed phases compared to the H phase increases going down the group from S to Se and also going from Mo to W for both considered Li concentrations. On increasing the lithium concentration from $Li_{0.5}MX_2$ to Li_1MX_2, the energy difference between the T″ mixed phase and the H phase decreases slightly for the sulfides but increases for the selenides. In contrast to our observation that the energy of the T″ mixed phase increases with respect to the H phase, Ma et al. reported a threshold of 0.4 e per MoS_2 to induce the transition from the H phase to the T″ mixed phase [218]. This discrepancy could be a consequence of the static charging method used in obtaining those results.

These trends in stability can be explained by simple electron filling in the rigid band approximation [42]. For the H and T″ mixed phases, excess electrons cause an increase in total energy equal to the band gap. As the T′ phase is semi-metallic, the next available energy level is at the Fermi level, and so this phase becomes lower in energy.

The barriers for the H to T′ phase transition in the charged monolayers are also shown in Fig. 4.8. In all cases, the barrier for the phase transition decreases due to lithium adsorption. The maximum barrier for the transition from the H phase to the T′ phase is found for MoS_2 at a value of 0.96 eV for $Li_{0.5}MoS_2$ and 0.57 eV for $Li_{0.5}MoS_2$. The minimum transition barrier from the H phase to the T′ phase is found for WSe_2 with a barrier of 0.62 eV for $Li_{0.5}WSe_2$ and 0.24 eV for Li_1WSe_2.

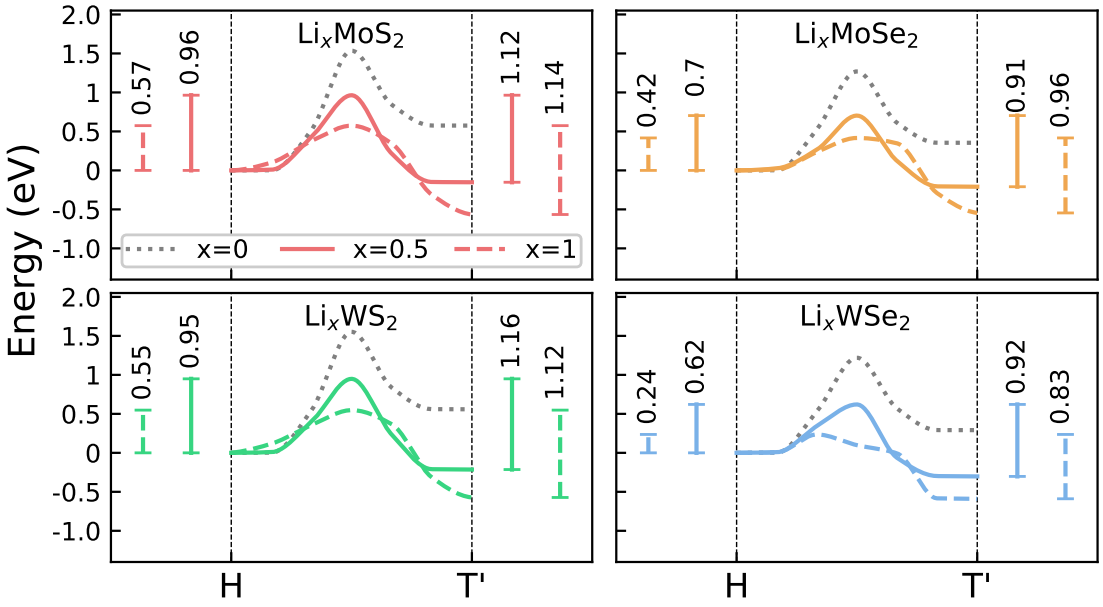

Figure 4.8: The relative energy difference and transition barrier between the H phase and the T′ phase of Li_xMoS_2, Li_xMoSe_2, Li_xWS_2 and Li_xWSe_2 with $x = 0$ (dotted line), $x = 0.5$ (solid line) and $x = 1$ (dashed line). The segments on the left (right) of the curves indicate the barrier for transition from the H to T′ (T′ to H) phase. Energies are referred to that of the H phase of each material.

WS_2 has the second highest barrier, at a value of 0.55 eV for the Li_1WS_2 structure, while $MoSe_2$ has a barrier of 0.42 eV at the same Li concentration. In all cases, the barrier to transition does not decrease to zero. As such, the transition cannot be spontaneous and an energy equal to the barrier height needs to be provided to induce the transition.

4.3.5 Discussion

Li adsorption is an exothermic process. The adsorption energies, defined as $E_{ads} = E_{Li_xMX_2} - E_{MX_2} - xE_{Li}$ where $E_{Li_xMX_2}$ is the total energy of the Li adsorbed structure, $E_{Li_xMX_2}$ is the total energy of the pristine monolayer, E_{Li} is the energy of an isolated Li atom and x refers to the Li concentration, for all four materials are given in Table 4.3. The Li adsorption energy is higher for T′ phase as compared to the H phase. For $Li_{0.5}MX_2$, the adsorption energy is largest for WSe_2 at -1.03 eV followed by $MoSe_2$ and MoS_2 at -0.99 and -0.97 eV per formula unit respectively, and smallest for WS_2 at -0.85 eV per formula unit. This energy is comparable to the energy barrier to the phase transition at this Li concentration. For Li_1MX_2, the adsorption energy per MX_2 approximately doubles, to at least 2.5 times the energy barrier. If some of this energy is used to overcome the barrier to the transition, Li adsorption may be sufficient to

	$Li_{0.5}MX_2$		$LiMX_2$	
	E^{H}_{ads}	$E^{T'}_{ads}$	E^{H}_{ads}	$E^{T'}_{ads}$
MoS_2	-0.97	-1.64	-2.51	-3.24
$MoSe_2$	-0.99	-1.41	-2.36	-2.89
WS_2	-0.85	-1.58	-2.26	-2.98
WSe_2	-1.03	-1.38	-2.16	-2.70

Table 4.3: Adsorption energy, E_{ads}, of lithium on the H and T′ TMD phases (eV per unit MX_2).

make the process spontaneous. Furthermore, given that the rate of transition decreases exponentially with activation energy (as per the Arrhenius equation), we can conclude that, for a given X, WX_2 will transition at a slightly higher rate than MoX_2. Likewise, for a given M, MSe_2 will transition at a higher rate than MS_2.

This is contradictory to the observation of a higher percentage of T′ phase found for WS_2 compared to $MoSe_2$ and WSe_2. To explain this, we must also consider the fact that in order to measure the T/H ratio experimentally, the exfoliated monolayers are washed with deionized water and dried in vacuum. In this process the Li ions desorb and the monolayers revert to their neutral state. They are prevented from transitioning immediately back to the ground-state H phase by an energy barrier. This is supported by the observation of the M^{4+} oxidation state in X-ray photoelectron spectra (XPS) [11, 12, 264].

The barriers for the reverse transition from the neutral T′ phase to the neutral H phase, shown in Fig. 4.5, are now relevant. For all materials, the barrier to return directly to the H phase is prohibitively high, ranging between 0.90 eV and 0.99 eV. Instead, the barrier to transition to a mixed T″ type phase is significantly lower, ranging between 0.39 eV and 0.48 eV. Experimental evidence for such an indirect transition from the T′ phase back to the H phase for MoS_2 via a mixed T″ mixed phase can be found: By fitting the rate equation to in-situ Raman measurements, the barrier to transform from the meta-stable metallic phase to the ground state was found to be 400 meV [227]. This barrier value is consistent with the calculated barrier to transition from the T″ mixed phase to the H phase of 450 meV calculated here (cf. Fig. 4.5) whereas the barrier to transition from the T′ phase back to the H phase directly is 970 meV. This suggests that the transition from the T′ phase to the H phase occurs in two steps for this material,

via the T″ mixed phase.

The barrier to transition from the T″ mixed phase to the H phase is smallest for the two selenium compounds at 0.23 eV and 0.27 eV for $MoSe_2$ and WSe_2, respectively. The barrier for WS_2 is twice as high, at 0.49 eV. The significance of this difference in barrier for WS_2 and WSe_2 can be determined by calculating the exponential factor of the Arrhenius equation at room temperature ($k_B T = 25.7\ \mathrm{meV}$). This is of the order of 5×10^{-9} for WS_2, whereas it is of the order of 1×10^{-4} for WSe_2. This rate difference is significant and its effects should be experimentally observable. This can explain the significant difference between the percentage of T′ phase observed in WS_2 compared to both $MoSe_2$ and WSe_2, [11]. However, the calculated activation barriers cannot explain the low 1T/2H ratio found in exfoliated MoS_2. This discrepancy could be due to non-electronic effects, such as a poor exfoliation efficiency in certain organometallic compounds, edge effects related to the change in lateral size of the exfoliated monolayers, the presence of defects or the oxidation of the exfoliated layers. Another possibility is that the simplified phase transition mechanism considered here does not consider the full nucleation process.

Finally, we note that the T″ mixed phase comprises of alternating H and T′ phases, each a unit cell thick, as illustrated in Fig. 4.4. However, this phase can be viewed as just one example of a family of mixed T′ and H phase structures. By changing the T′:H ratio in MoS_2 from 1:1 for the T″ structure to 2:1, the total energy difference between it and the H phase increases from 0.49 eV to 0.51 eV. By increasing the ratio further to 3:1, the energy difference increases further to 0.52 eV. Clearly, the total energy of MoS_2 is strongly dependent upon the fraction of H phase. The energy of all such families of confined structures will be higher than that of the H phase but lower than that of the T′ phase. The exact composition of such confined structures will be dependent on the available energy and the TMD flake size and shape and are not confined to the idealised one dimensional structures discussed here. Experimentally, the boundary between the H phase and T′ phase areas are observed to be atomically sharp, as in the T″ mixed phase. This boundary evolves over time via a transversal displacement of one of the S planes [224, 268] leading to the complete phase transition of the flake. The observed partial phases, with mixed metallic (T′) and insulating (H) regions, can be understood as intermediate stable structures which have lower barriers of transition.

4.3.6 Conclusion

Group-VI TMDs are known to undergo structural phase transitions from a semi-conducting H phase to a metallic T phase when subjected to alkali-metal assisted exfoliation. The efficiency of this process is strongly dependent on the chemical composition of the material. We show that the ratio of T′ to H phase is maximized if the charge-induced transition from the H phase to the T′ phase is favourable and the reverse transition upon removal of charge is unfavorable. For example, the high proportion of T phase found in WS_2 monolayers after alkali treatment can be explained by a high barrier to revert back to the H phase after the initial phase transition has been induced. While charged MSe_2 materials have the lowest energy barriers to the phase transition, the barriers to revert back to the H phase are also low. This can explain the relatively low content of metallic phase found in $MoSe_2$ and WSe_2 after exfoliation. Finally, the low proportion of metallic phase found in MoS_2 monolayers in some experiments cannot be explained using the activation barriers alone and so non-electronic effects, such as a differing exfoliation efficiency or differing levels of monolayer oxidation, must also contribute to the outcome.

4.4 Cointercalation

To achieve selective intercalation of ions, molecules, or both simultaneously, an atomic level understanding of the relative energetics of the various scenarios is necessary. Computationally, due to increasing degrees of freedom, attempting a brute force geometry optimization to determine the minimum energy configurations is not feasible. Here, we present a work-flow to determine the lowest energy configurations when both a representative alkali metal ion (potassium), and a selection of organic molecules, namely benzaldehyde, NMP, chloroform and toluene, interact with each other and with a graphene bilayer. The work-flow is both ion and molecule independent.

Several possible relative orientations of the solvent molecule (M), the two graphene layers (L) and the potassium ion (K) are possible:

- LMLK – the molecule is intercalated between the two graphene layers while the potassium ion is adsorbed on the outer graphene layer.
- LMKL – both molecule and potassium ions intercalate between the two graphene layers.
- LLMK – both the molecule and potassium ion do not intercalate, but instead adsorb on the surface of the bilayer.
- LKLM – the potassium ions intercalate between the layers while the molecule is adsorbed on the outside.

To determine the most likely configuration of a given molecule-ion pair, we can rank the relative orientations based on their calculated total energies. The orientation with lowest energy is energetically most favorable. The orientation with the highest total energy is least likely to form.

The desired relative orientation depends on the application. In some cases, it is vital that co-intercalation of ion and molecule does not occur. For example, the co-intercalation of propylene carbonate (PC) with Li ions is understood to be responsible for the degradation of graphite electrodes, primarily by exfoliation. This is the LMKL orientation. In other cases, exfoliation may be the desired outcome, such as in salt-assisted exfoliation techniques.

Calculations are done using VASP (V5.4) and the recommended PAW-PBE potentials. To account for long range van der Waals interactions, the optB86b-vdW exchange-correlation functional was used [77, 82]. This is used

due to its broader applicability in the presence of charge transfer [81, 187].

Each layer of graphene contains 60 atoms with an in-plane unit cell size of 12.80 Å × 12.31 Å. In the direction perpendicular to the graphene plane we add a vacuum region of 15 Å to decouple the periodic images. To remove spurious interactions between periodic images the dipole corrections enabled.

For all calculations, a plane wave energy cutoff of 640 eV is used for the plane wave basis set with the energy convergence criteria of 10^{-7}eV. All the energy and geometry calculations are carried out using a Γ-centered K-point grid of 5×5×1. The positions of the atoms are relaxed until the force is less than 0.025 eV/Å on all atoms.

4.4.1 Determination of relative orientations

To determine the relative orientations of all components, we use an additive method in which the position of each new component such as graphene layer, molecule and potassium is obtained assuming the components already present remain fixed. For example, to obtain the orientation of a molecule absorbed on top of the bilayer graphene slab, we first find the relative orientation of the molecule with respect to the monolayer graphene and then assume that the second layer of graphene will be in the same orientation as bilayer graphene. This assumption is valid due to the van der Waals nature of the graphene–molecule interaction. Similarly, when a molecule is intercalated in bilayer graphene, we first determine the relative orientation of the molecule with monolayer graphene and then add the second graphene layer on top of the molecule. Again, this is valid due to the van der Waals nature of the interaction between the molecule and graphene. Following this strategy the relative positions of various components are discussed below.

4.4.1.1 Potassium interacting with monolayer graphene

To determine the position of potassium with respect to a graphene layer, we calculate the total energy of the monolayer – potassium system for the three high-symmetry adsorption sites, namely on-top, bridge and hollow site. These positions are shown in Fig. 4.9 for a potassium ion adsorbed at a height of 2.7 Å from the graphene surface. This distance was chosen as the van der Waals radius of potassium is 2.8 Å. From this we find that the lowest energy adsorption site of K is at the hollow site, followed by the bridge site with an energy 82 meV above

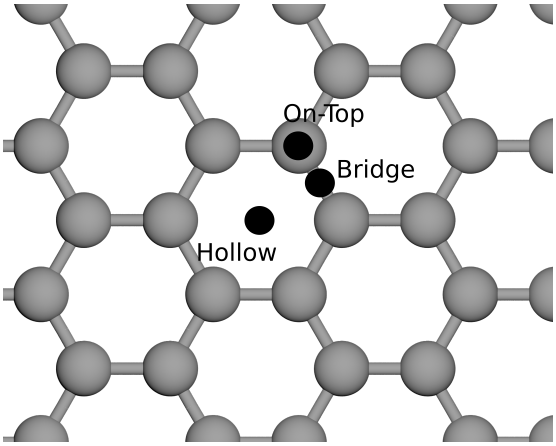

Figure 4.9: The three high-symmetry adsorption sites on graphene, namely on-top, bridge and hollow sites.

that of the hollow site and finally the on-top site with an energy 94 meV above that of the hollow site.

To determine the final position of the potassium ion near the graphene surface, the geometry is optimized with the potassium atom placed at the hollow site, while keeping the graphene layer fixed. For this optimized geometry, the potassium ion adsorbed at a height of 2.59 Å above the surface of graphene. This adsorption position of K is used to determine all graphene-potassium distances. In cases where the potassium ion is present in between the layers, we assume that the layers are stacked in the AA configuration with the potassium ion adsorbed on the hollow site in between the layers.

4.4.1.2 Solvent molecule interacting with monolayer and bilayer graphene

When a molecule is adsorbed on the outer surface of the graphene bilayer, we can use the potential energy surface calculated in Section 3.2.1.2 to determine the minimum energy orientation. In cases where the molecule is intercalated between two graphene layers, we have to determine the potential energy surface of molecules with respect to two layers. We start by using the potential energy surface of a molecule adsorbed on monolayer graphene, as calculated in Section 3.2.1.2, to determine the position of the molecule for a given rotation. Of these, we discard all positions higher in energy than the absolute minimum by at least 100 meV. For all the remaining positions within 100meV of the minimum, we allow only two choices for the registry of the second graphene layer - either AB or AC stacking with respect to the first graphene layer. The

AB stacking is defined as that found when the second layer is shifted along the armchair direction by one bond length in the positive direction, while AC stacking is defined as that found when the second layer is shifted along the armchair direction by the same amount in the negative direction. The second graphene layer is placed at a height of 3.5 Å above the center of mass of the molecule. The total energy is calculated for each of these structure. For the configuration with the lowest energy, we optimize the distance between the two graphene layers and the molecule to find the equilibrium structure. This is then designated the ground-state structure for that configuration.

4.4.1.3 Co-adsorption on monolayer graphene

We first determine the lowest-energy configuration when both the potassium and molecule adsorb on opposite sides of a graphene layer. Their relative positions can be determined from a potential energy surface. We restrict the orientation of molecule and graphene layer to the one determined in Section 4.4.1.2 and optimize the position of the potassium atom. Only the on-top, hollow and bridge sites are considered as the candidate positions for potassium.

We find that, in all cases, the potassium adsorbs on the hollow site located closest to the most electronegative site of the molecule. We assume that when both the molecule and ion are adsorbed on the same side of a graphene layer, K also adsorbs on the hollow site closest to the most electronegative site of the molecule.

4.4.2 Determining the Equilibrium Structures

To determined the relative orientations of the two graphene layers, the molecule and the potassium ion, static calculations are combined to obtain the starting point for a full structural relaxation. Using the determined position of the molecule in between the graphene layer and the position of potassium ion when the molecule is present on the opposite side of the layers, we determine the configuration where the molecule in present in between the layer and potassium is on top (LMLK). Using the same position of the molecule in between the bilayer, and the fact that the molecule–graphene distance is larger than the potassium–graphene distance we can obtain the configuration where both the molecule and the potassium in present in between the layers (LMKL).

Using the positions determined for the molecules near monolayer graphene and assuming that the potassium ion adsorbs on the hollow site, we can determine the configuration where the molecule is on top of the layer and the potassium

Molecule	L1–L2	K–L1	K–L2	M–L1	M–L2
benzaldehyde	5.18	2.59	2.59	8.41	3.23
NMP	5.18	2.59	2.59	8.56	3.38
toluene	5.18	2.59	2.59	8.5	3.32
chloroform	5.18	2.59	2.59	8.58	3.4
cyclopentanone	5.18	2.59	2.59	8.65	3.48

Table 4.4: Relative distances (in Å) between the center of masses of each components in the LKLM arrangement.

Molecule	L1–L2	K–L1	K–L2	M–L1	M–L2
benzaldehyde	3.35	6.11	2.75	6.81	3.46
NMP	3.35	6.05	2.69	6.84	3.49
toluene	3.35	6.04	2.68	6.82	3.46
chloroform	3.35	6.02	2.66	6.91	3.56
cyclopentanone	3.35	6.02	2.67	6.9	3.54

Table 4.5: Relative distances (in Å) between the center of masses of each components in the LLMK arrangement.

is present in between the layers (LKLM). For the same position of the molecule and the potassium ion adsorbed on the nearest hollow site, we can determine the configuration where the molecule and potassium are both present on top of the bilayer (LLMK).

These configurations are the starting points for full structural relaxations (the atoms in the graphene layers are held fixed). The final relaxed structures are shown in Fig. 4.10. For all optimized structures, the total energies relative to the lowest energy orientation are given in Tab. 4.8. The minimum energy configuration occurs when the molecule and potassium ion are absorbed outside the bilayer (LLMK) regardless of the molecule type. The next most energetically favorable configuration depends on the molecule. In the case of chloroform and toluene, the minimum energy configuration is followed by that where the potassium has intercalated between the layers while the molecule remains adsorbed on top, i.e., the LKLM configuration. In the case of NMP and benzaldehyde, the minimum energy configuration is followed by that where both the molecule and potassium intercalate between the layers (LMKL). Finally in case of cyclopentanone, the energies are similar for both the configuration where potassium alone has intercalated and the molecule is adsorbed on top (LKLM) and that where the molecule and ion co-intercalate.

Molecule	L1–L2	K–L1	K–L2	M–L1	M–L2
benzaldehyde	6.57	9.14	2.57	3.31	3.27
NMP	7.05	9.63	2.57	3.59	3.46
toluene	6.72	9.3	2.58	3.3	3.43
chloroform	7.34	9.91	2.57	3.57	3.77
cyclopentanone	7.15	9.72	2.57	3.62	3.53

Table 4.6: Relative distances (in Å) between the center of masses of each components in the LMLK arrangement.

Molecule	L1–L2	K–L1	K–L2	M–L1	M–L2
benzaldehyde	6.57	3.3	3.27	3.29	3.28
NMP	7.05	3.49	3.56	3.53	3.52
toluene	6.72	3.86	2.87	3.3	3.42
chloroform	7.34	4.39	2.95	3.59	3.75
cyclopentanone	7.15	3.68	3.47	3.58	3.57

Table 4.7: Relative distances (in Å) between the center of masses of each components in the LMKL arrangement.

For all optimized structures, the distances between the centers of mass of the various components are given in Table 4.4 for configuration LKLM, Table 4.5 for configuration LLMK, table 4.6 for configuration LMLK and Table 4.7 for configuration LMKL. The distance given is measured in the direction perpendicular to the graphene layers. L1 is the bottom-most layer and L2 is the top-most graphene layer. The layers are labeled such that the potassium ion is always adsorbed on the top-most layer (L2) when it is not between the layers.

If the molecule is adsorbed on the surface of the bilayer (Table 4.4 and 4.5), the distance between the molecule and layer depends on the position of the K atom. If K is also located outside the bilayer, the M-L2 distance is higher than when the K is intercalated between the layers. The interlayer distance decreases due to K intercalation.

When K is adsorbed on the surface of the graphene layer and the molecule is intercalated between the layers, the K–L2 distance is similar to the equilibrium distance of 2.59 Å when no molecule is present. When both the molecule and the potassium are present in between the layers, the potassium is equidistant from both the layers regardless of the molecule type. This is shown by the distances

Molecule	LKLM	LLMK	LMKL	LMLK
benzaldehyde	2.88	0	2.47	3.64
chloroform	2.37	0	2.95	3.58
cyclopentanone	2.92	0	2.94	4.05
NMP	3.02	0	2.78	4.04
toluene	2.09	0	2.5	2.99

Table 4.8: Energies (in eV/u.c.) of all configuration, given relative to the minimum energy configuration (0 eV/u.c.).

K–L1 and K–L2 in Table 4.7.

The lowest energy for the configuration LLMK is due to the higher van der Waals binding energy of the bilayer graphene ($E_b^{bilayer}$ = 3.90 eV/u.c.) as compared to both the molecule–layer and potassium–layer binding energy. For a molecule or potassium ion to intercalate between the layers, the binding energy of molecules or potassium has to compensate for this interlayer binding energy of graphene. In all cases, $2E_b^{molecule-layer} << E_b^{bilayer}$, where $2E_b^{molecule-layer}$ is the molecular binding energy on monolayer graphene and where the factor of 2 is to compensate for the molecule in contact with the two graphene layers. Similarly, the potassium–graphene layer binding energy of 1.4 eV is also not comparable to the interlayer binding energy ($E_b^{bilayer}$).

The relative energies for next two configurations, namely LMKL and LKLM, can be understood by considering the structure for those configurations. When a molecule is intercalated between the layers, the interlayer distance is larger than that when only potassium is present. Hence the interaction between the potassium ion and the graphene layers is negligible when the molecule is also located between the layers. Additionally, the molecule–layer binding energy is smaller than the potassium–layer binding energy. Highly polar molecules such as benzaldehyde, cyclopentanone and NMP which can accept electrons, prefer to bind to the potassium ion. This is not the case for non-polar toluene and chloroform. As a result, for these two molecules, the binding energy is maximized when the potassium atom alone remains between the layers, while the molecule binds on the outside of the bilayer. Finally, the LMLK configuration has the highest relative energy due to the lower molecule–layer interaction compared to the potassium–bilayer interaction and the absence of any potassium–molecule interaction.

The total charge on each component can be calculated using Bader charges.

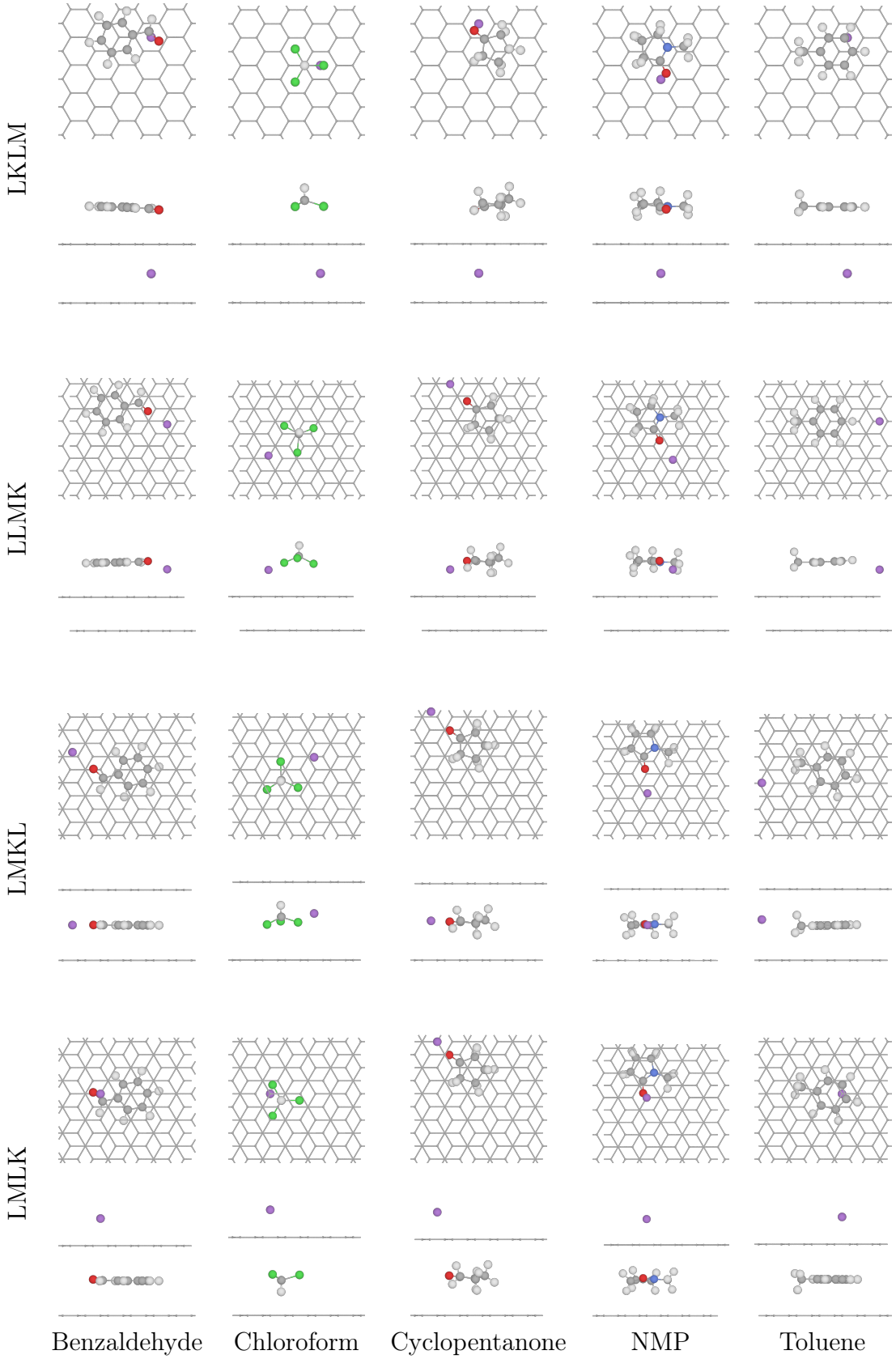

Figure 4.10: The top view (top panel) and the side view (bottom panel) of all optimized structures.

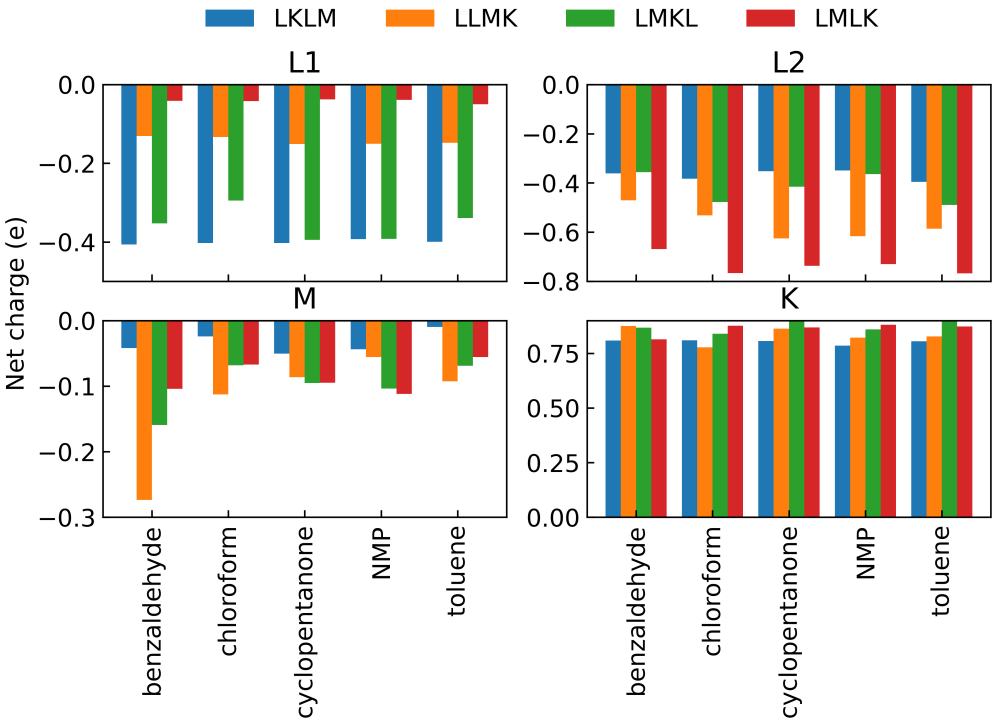

Figure 4.11: Total charge present on the bottom layer (L1), top layer (L2), molecule (M) and the potassium ion (K) for all the arrangements LKLM (blue), LLMK (orange), LMKL (green) and LMLK (red) arrangement for the molecules considered here.

The total charge on each component in all considered arrangements is shown in Fig. 4.11. In all cases, electrons are transferred from the potassium ions to the nearest components. In the LMLK arrangement, charge is predominantly transferred to the molecule (M) and the layer nearest to potassium (L2) with negligible charge transferred to the farthest layer (L1). In the LKLM arrangement, charge is transferred equally to both layers (L1 and L2) with minimal charge transferred to the molecule. In the LMKL and LLMK arrangements, charge is distributed to both the layers and molecules. When the molecule is near the potassium ions the charge is distributed over both layers and molecules.

From these charge transfer calculations we can conclude that the potassium transfers equal amounts of charge irrespective of the arrangement of the components. Most of this charge is transferred to the nearest components with components not directly in contact with the ion receiving negligible charge.

4.4.3 Conclusions

We have developed a work-flow to determine the relative orientations of molecules, metal ion and bilayer graphene. This work-flow takes into account all the possible intercalation configurations while considering the symmetry of the molecules to eliminate duplicate structures, hence reducing the computational cost. This work-flow can be further improved by performing geometry optimizations for all the possible configurations. This can be achieved by considering individual components such as the molecule, the metal ion and the two layers as rigid bodies which can move only in the direction perpendicular to the graphene layers. This approach will eliminate the requirement of determining the equilibrium distances for each pair of components.

For the particular molecular and ionic concentration considered here, total energy calculations suggest that neither the molecule or potassium ion intercalate the bilayer graphene. The calculated energies also show that the intercalation of the molecule alone is the most unfavorable configuration. The charge transferred from potassium is localized to the nearest molecule and the layer in contact with the ion.

This initial work can be extended to consider other concentrations of molecules or ions to model more realistic experimental situations. It can also be further improved by considering other graphene stacking. This work flow can then be used to screen solvents that enable spontaneous ion- or molecular-intercalation without the use of particular experimental procedures requiring high temperatures or pressure.

CHAPTER

5

FERROELECTRIC MOLECULAR SWITCH

5.1 Introduction

Electronic sensors detect external stimuli, whether gas molecules [269, 270, 271, 272], mechanical deformations [273] or variations in temperature [274], by measuring changes in the current voltage (I-V) characteristics. Gas sensors detect the presence of a particular molecule or a class of gas molecules. They generally consist of an exposed surface on which the molecules adsorb. These molecules modify the local electronic structure thereby modifying the transport properties of the device. This modification can then be measured as a change in the I-V response. For example, the Ga doped ZnO surface is used for the sensing of CO molecules and the SnO_2 surface is used to detect small hydrocarbons [275]. The choice of surface dictates the gas molecules that will be detected by the sensor.

Since their discovery, graphene and other two dimensional materials have emerged as prime candidates for electronic sensors due to their high specific area, i.e., the high surface area available for adsorption per unit mass. The surface, also

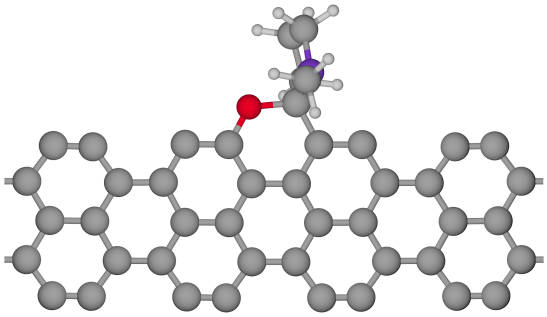

Figure 5.1: An example of NMP molecule bound to the dangling bonds of the graphene flake due to their high reactivity.

known as the basal plane, can act as a host on which the molecules can adsorb. Graphene in particular has attracted considerable attention due to its high specific surface area of close to 2600 m^2g^{-1} [276], its ability to accept and donate electrons simultaneously and its ability to detect of fractional charges [277]. In practice, manufacturing the ideal surface that demonstrates these unique properties can be a challenge. Edges are more reactive than the basal plane. Due to their high reactivity, molecules can be chemisorbed on the edge rather than physiorb on the surface. An example is shown in Fig. 5.1. The chemisorption process is generally irreversible and molecule agnostic. If the dangling bonds are passivated, i.e., terminated with some functional groups such as hydrogen, fluorine or oxygen, this reduces the reactivity of the edge. These passivated edge sites can then act as physisorption sites for small molecules which bind via a combination of dispersion and Coulomb interactions.

Molecular adsorption can modify the charge transport properties of the monolayer. Caridad et al. demonstrated that polar molecules (water, ammonia, and nitrogen dioxide) adsorbed on graphene edges can be switched reproducibly between two available states in response to an external electric field [50]. This switching introduces large changes in the graphene resistance. This change in resistance can be attributed to a ferroelectric-like behavior of the polar molecules. A schematic of the experimental device is shown in Fig. 5.2(a). A flake of graphene is encapsulated between layers of hexagonal boron nitride (h-BN). This encapsulation prevents molecules from adsorbing on the surface of graphene and instead to adsorb only on the terminated edge sites. A scanning electron micrograph (SEM) of the fabricated device is shown in Fig. 5.2(b).

The resistance is measured for two types of graphene edge terminations (oxygen

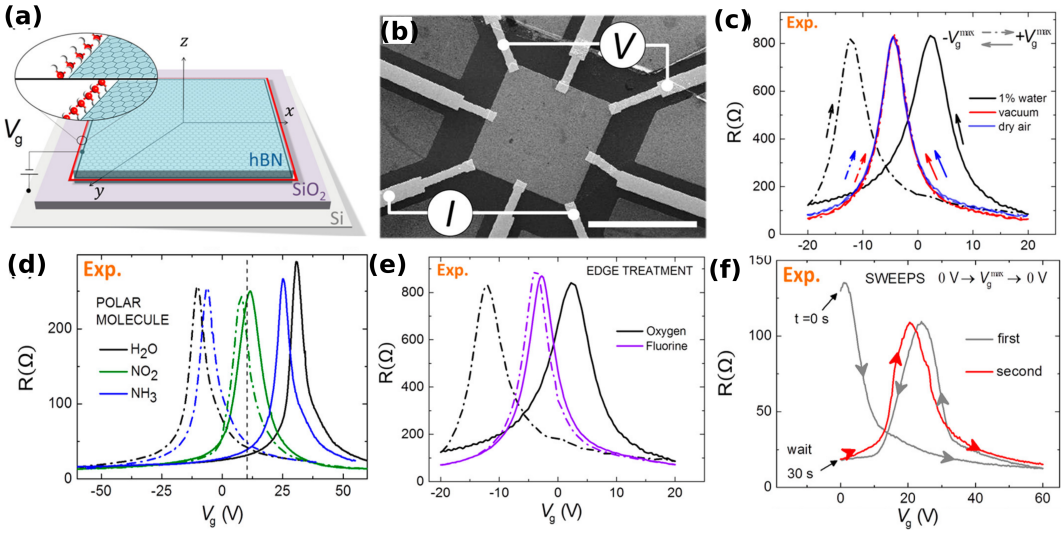

Figure 5.2: (a) A schematic of the fabricated device of graphene encapsulated inside hexagonal Boron Nitride layers with oxygen terminated edge and adsorbed H_2O molecules, (b) Scanning electron micrograph (SEM) of a fabricated device shown, (c) measured resistance of device with oxygen terminated edges when exposed to vacuum, dry air and air with 1% humidity, (d) measured resistance of device with oxygen terminated edges when exposed to H_2O, NO_2 and NH_3, (e) measured resistance of device with oxygen and flourine terminated when exposed to H_2O molecules. (f) measured resistance of a freshly prepared device with oxygen terminated edges when exposed to water molecules, here the gate voltage cycle $0V \rightarrow V_{max} \rightarrow 0V \rightarrow V_{max}$ is indicated as arrows. All figures are reproduced from Caridad et al. [50]

and fluorine), when exposed to different environmental conditions: vacuum, dry air, dry air mixed with 1% water vapor, dry air mixed with 1% nitrogen dioxide and dry air mixed with 1% ammonia. In vacuum, when a gate voltage is applied, the resistance across the graphene sheet decreases, as seen from the red line in Fig. 5.2(c). On exposing this device to dry ambient air (i.e., without water molecules), the resistance of the device behaves similarly to the case when as exposed to vacuum as seen from the blue line in Fig. 5.2(c). The peak in the measured resistance is designated the charge neutrality point (CNP) and corresponds to a zero net polarization of the graphene electron density. On application of a gate voltage, the electron density polarizes which results in a lower measured resistance. However, when the device is exposed to water molecules (1% H_2O in ambient air) the resistance trends of the device change. The measured resistance now shows two distinct peaks depending on the direction of the voltage sweep, as seen from the black lines in Fig. 5.2(c). The distinction between the curves for two directions of gate voltage sweep can be interpreted as a hysteretic behavior which can be controlled by the gate voltage.

The change in the position of the peaks corresponds to a shift in the neutrality point of the device. The position of the peak relative to that in vacuum is an indication of the molecules ability to polarize the electron density of the device, and the ability of the gate to align the molecular dipoles.

The resistance behavior has a strong dependence on both the type of adsorbed molecule and the type of edge termination. For an oxygen terminated device, H_2O molecules induce the strongest hysteresis effect, closely followed by NH_3 with NO_2 showing essentially no hysteresis behavior, as shown in Fig. 5.2(d). This trend roughly follows the electric dipole moment of the molecules which is highest for H_2O (1.85D) followed by NH_3 (1.74D) and then NO_2 (0.4D). On changing the type of graphene edge termination, from oxygen to fluorine, the peak separation in the case of H_2O drastically reduces as shown in Fig. 5.2(e).

The mechanism for hysteresis can be understood from experimental measurements starting from a fresh sample where the gate voltage is cycled from $0V \rightarrow V_{max} \rightarrow 0V \rightarrow V_{max}$ this is shown in Fig. 5.2(f). For a freshly prepared sample the charge neutrality point is at 0V. From this one can expect that the molecules are randomly oriented. As a result, there is a net cancellation of the polarizing effect of the molecular dipoles on the electron density of the device. This is seen as a peak in the resistance measurements at 0V. On increasing the gate voltage from $0V \rightarrow V_{max}$ the resistance decreases rapidly due to the polarization of electron density. This is similar to what happens when the device is in vacuum (red line in Fig. 5.2(c)). The gate voltage also induces the alignment of the molecular dipoles to the external field. When the voltage is reversed from $V_{max} \rightarrow 0V$ the external field decreases in strength while maintaining its direction. The molecules do not immediately revert back to their original random orientations. As a result, there is still a net polarization of the device electron density. This polarization is present even at 0V and can be seen from the lower resistance at 0V at the end of this sweep cycle. Since the polarizing effect of the dipoles is opposite to that of the gate, the voltage at which these two effects cancel each other corresponds to the charge neutrality point, i.e., the charge density of the device shows no net polarization and corresponds to a peak in the resistance measurements. The position of this peak does not shift in subsequent cycles as seen from the voltage cycle $0V \rightarrow V_{max}$. As the position of peaks depends on the alignment of molecules to the external field, the molecules will change direction on reversal of the gate voltage. As a result, the peak is symmetric around 0V as shown in Fig. 5.2(c,d,e).

Using density functional theory calculations, Caridad et al. showed that the adsorbed molecules have two stable positions with respect to the graphene layer: one where the molecules are below the plane of graphene and another where the molecules are above the plane of graphene. These two positions are mirror images of each other with respect the graphene layer, with the orientation of the molecular dipoles opposite to each other. To determine the effect of the external field on the orientation of the molecules, they also calculated the total energy of the device when the molecules are aligned to the external field and when they are misaligned to the external field. They find that the energy is lower when the molecular dipoles are aligned to the external field. For the oxygen terminated device, the magnitude of the energy difference between the two cases depends on the type of molecule. It is highest for H_2O followed by NH_3 and with NO_2 showing a very small difference. In the case of H_2O this large magnitude vanishes on changing the termination of the device from oxygen to fluorine. This dependence on the edge termination would suggest that the molecule dipole strength is not the sole parameter that dictates the effect of orientation of the molecules.

They also show that the observed resistance changes are due to a realignment of molecules, with the position of the peak dependent on the difference in the number of molecules (N_s) present in the two stable positions. To do this, they modeled the molecules as a chain of dipoles. The dipoles can either be parallel (i.e., located on same side of the graphene) or anti-parallel (located on different sides of the graphene). When equal number of molecules are present in both the stable positions, i. e., $N_s = 0$, the peak is exactly at 0V as the effect of the molecular dipoles on the electron density of the device cancel each other. On increasing the difference between molecular populations, so that $N_s > 0$, the effect of the dipoles in the parallel and anti-parallel configurations no longer cancel. This results in the peak in the resistance shifting away from zero. This shift is maximum when all the molecules are present in one of the two positions.

From both the experiment and the calculations it is clear that the hysteresis is due to an alignment of the molecular dipoles to the external field of the gate. Additionally, in order to maximize the hysteresis, the molecular dipoles have to align in the parallel configuration, similar to ferromagnets. The dipoles in this parallel configuration must then be effectively coupled to the external electric field in order for them to change direction with the change in the sign of the gate voltage. To tune the performance of the device and to understand the effect of the molecule type and edge termination of the hysteresis, it is essential to determine

the factors affecting the alignment of molecular dipoles and its coupling to the external field.

The aim of this work is to understand (1) what is the effect of the edge termination on the orientation of molecules, (2) what is the effect of the edge termination on the molecule–molecule interaction, (3) under what conditions the molecular dipoles align parallel to each other, (4) what is the effect of the device edge termination on the molecule dipole – gate interaction and (5) to develop an effective Ising-like model to study the relative importance of these effects on the measured hysteresis.

5.2 Computational Details

All density functional theory calculations are performed using CP2K (V7.1) [278] code, with DZVP-MOLOPT-SR-GTH basis sets and the corresponding recommended pseudopotentials [279]. For all the energy calculations the tolerance of 10^{-7}Ry was used. In the non-periodic directions a vacuum length of at least 16 Å was used.

The geometry optimizations used a relative cutoff of 50 Ry and cutoff of 850 Ry with the progression factor of 3 and 4 multi grids. A k-point grid of 21×1×1 was used. The calculations used a Fermi-Dirac smearing scheme with an electronic temperature of 300 K. The Broyden–Fletcher–Goldfarb–Shanno (BFGS) algorithm was used for geometry optimization with a force tolerance of 1.9×10^{-4}Ry/Bohr.

The gate calculations used a relative cutoff of 50 Ry and cutoff of 850 Ry with the progression factor of 3 and 4 multi grids. The calculations used a Fermi-Dirac smearing scheme with an electronic temperature of 300 K. The implicit Poisson equation with the applied gate voltage is converged to a tolerance of 10^{-7}Ry. The gate region was set to have a width of 0.5 Å and a smoothing width of 0.2 Å. Similarly, for the gate dielectric we use the a smoothing width of 0.2 Å.

To decouple the periodic images, an implicit Poisson solver with appropriate boundary conditions is used. The boundary conditions for the implicit solver are given along with the corresponding results.

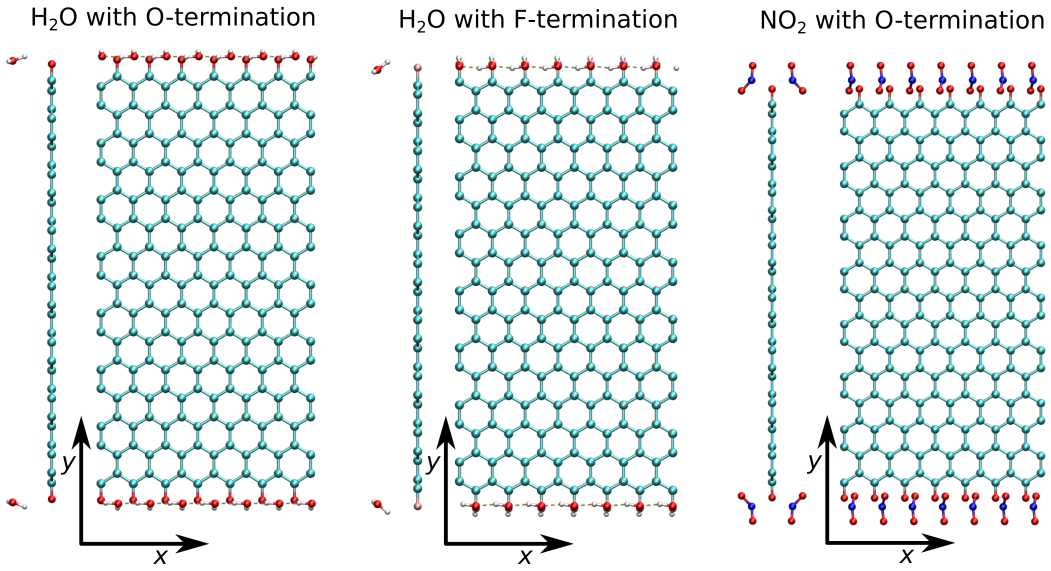

Figure 5.3: Side view showing a H-bonded H_2O chain adsorbed on both an O- and F-terminated graphene edge, and the absence of H-bonding for an NO_2 chain adsorbed on the O-terminated graphene edge.

5.3 Molecular orientations at graphene edge

To emulate the graphene flake in the experimental device, we use a periodic zigzag graphene nano-ribbon with a width of 30 atoms in the lateral direction. The width of the ribbon was chosen to avoid interactions between molecules adsorbed on opposite edges. The graphene nano-ribbon is periodic along the x direction. The z direction is perpendicular to the surface of the ribbon. In order to decouple the periodic images we use a real space Poisson solver with von Neumann boundary conditions in the y-z direction with periodic boundary conditions in the x direction. The geometry of the unterminated nano-ribbon was first optimized to obtain the pristine structure (before molecular adsorption). The planar geometry was then further optimized with either oxygen or fluorine added to the edge sites. For all further geometry optimizations the functionalised graphene nano-ribbon structure was kept fixed.

To determine the orientation of molecules near a terminated graphene edge, we start with molecules oriented such that they are not in the same plane as the ribbon. The adsorption concentration is fixed at one molecule per terminating atom. The implications of this will be discussed later. The relaxed geometry is shown in Fig. 5.3.

In the case of oxygen functionalised edges, the oxygen atoms act as anchors forming hydrogen bonds with the adsorbed water molecules. Due to this, one

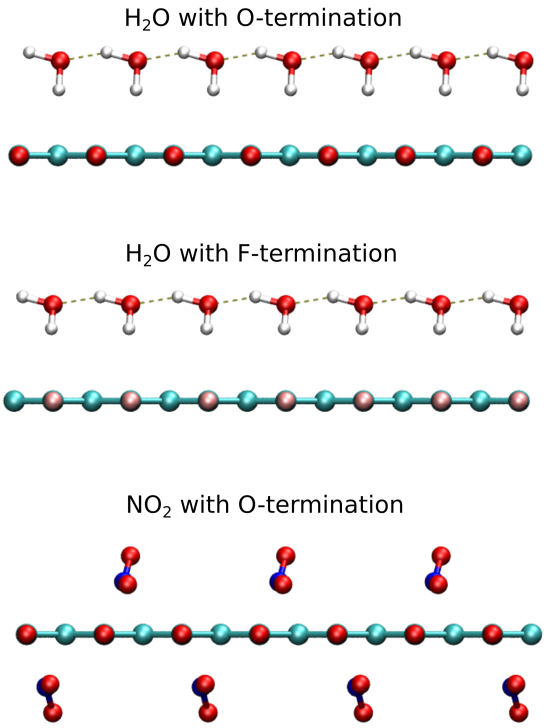

Figure 5.4: H-bonding structure for H_2O on both oxygen/fluorine terminated graphene and the its absence in NO_2 on oxygen terminated graphene.

hydrogen atom of each molecule is bonded to the functionalised oxygen edge and the other hydrogen atom is bonded to the oxygen atom of the neighboring water molecule as shown in Fig. 5.4. This anchoring results in the dipoles moments of the adjacent molecules oriented parallel to each other. In the case of fluorine functionalised edges, the water molecule chain rotates such that the polar O-H bond aligns with the C-F bond of the functionalised edge while maintaining the hydrogen bond in between the molecules as shown in Fig. 5.3 and Fig. 5.4.

The angle between the molecular plane formed by the three atoms in the H_2O molecules and the functionalised graphene nano-ribbon is also dependent on the type of edge functionalization. The angle between the normal to the molecular plane and the z axis is 70.23° in the case of an oxygen termination and 52.04° in the case of a fluorine termination.

In the complete absence of a H-bonding interaction between molecules, as in the case of NO_2, the molecules on adjacent edges prefer to orient on the opposite side of the nano-ribbon. This configuration is shown in Fig. 5.3. We label this the 'anti–parallel' configuration. The energy difference between this molecular configuration and the one where all molecules are located on the same side of the graphene edge (the 'parallel' configuration) is 0.48 eV/molecule. This anti-parallel

Structure	$E_{flip}(eV)$
H_2O+ O-terminated	-0.50
H_2O+ F-terminated	-0.54
NO_2+ O-terminated	-1.38

Table 5.1: Energy required to flip one molecule from the ground state configuration.

alignment of the molecular dipoles is driven by the dipole–dipole interaction and the absence of a H-bonding interaction and will be discussed further in the next Section.

We also test the possibility that the molecules adsorb completely in the plane of the ribbon. However, this energy is larger than either of the out-of-plane configurations by 0.61 eV/molecule for the case of H_2O adsorbed on an O-terminated nano-ribbon.

5.3.1 Intermolecular interactions

To determine the intermolecular interactions of molecules adsorbed on the functionalised edge, we calculate the energy required to move one molecule from the minimum energy configuration. For example, in the case of water adsorbed on a O-terminated graphene edge, this is defined as the energy difference between the configuration where all the molecules form a chain beneath the plane of graphene and the configuration where a single molecule has flipped to the opposite side of the plane. In terms of the molecular dipole orientation, this is the energy difference between the configurations when all the molecular dipoles are parallel (E_P) and when one molecular dipole is anti-parallel (E_{1AP}), i.e., $E_{flip} = E_P - E_{1AP}$. For the case of NO_2 molecules, which have an anti-parallel ground-state configuration, $E_{flip} = E_{AP} - E_{1P}$. These energies are given in Table. 5.1. The energy to flip one NO_2 molecule adsorbed on the O-terminated graphene edge is -1.38 eV/molecule. This is the maximum energy difference of all considered cases. The energy to flip one H_2O molecule from the parallel configuration is -0.50 eV/molecule and -0.54 eV/molecule for O-terminated and F-terminated graphene edge respectively. From this similarity it can be concluded that the effect of type of edge functionalization has a negligible effect on the intermolecular interaction. Instead, the role of the functionalised edge is limited to determining the orientation of the molecules near it.

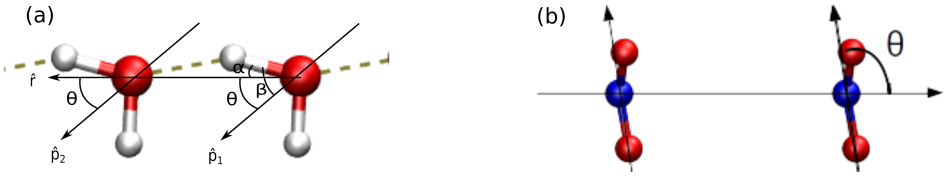

Figure 5.5: Schematic of all the measured and derived angles used to determine the relative dipole orientations.

As the interaction between the molecules is independent of the funtionalised edge, the difference in relative orientation of H_2O molecular chains and NO_2 molecular chains can be understood from simple dipole–dipole interactions. The interaction energy between two dipoles with dipole moment μ in S.I. units is given as [280]:

$$E_{\hat{p}_1,\hat{p}_2} = \frac{\mu^2}{4\pi\epsilon_0 r^3}\left(\hat{p}_1 \cdot \hat{p}_2 - 3\left(\hat{p}_1 \cdot \hat{r}\right)\left(\hat{p}_2 \cdot \hat{r}\right)\right) \tag{1}$$

where $\hat{p}_1$ is the unit vector pointing in the direction of the first dipole, $\hat{p}_2$ is the unit vector pointing in the direction of the second dipole, r is the distance between two dipoles, $\hat{r}$ is the unit vector along the line joining the centers of the two dipoles and $\frac{1}{4\pi\epsilon_0}$ is Coulomb's constant. For the case of the coplanar parallel dipoles shown in Fig. 5.5, Eq. 1 can be simplified as:

$$E_P = \frac{\mu^2}{4\pi\epsilon_0 r^3}\left(1 - 3\cos^2\theta\right) \tag{2}$$

where θ is the angle the dipole makes with the radial vector.

In the case of water molecules adsorbed on both O- and F- terminated graphene edges, the angle θ can be derived from the optimized structure assuming that the dipole is orientated along the angle bisector of $\angle HOH$ and is shown in Fig. 5.5(a). The angle θ can be calculated as $\theta = \beta - \alpha$, where $\beta = \frac{\angle HOH}{2}$ and α is measured for the optimized structure shown in Fig. 5.5(a). Similarly, in the case of NO_2 the dipole is along the angle bisector of $\angle ONO$ and lies in the same plane as the O–N–O bond. Hence the angle θ is approximately the same as the angle made by the N–O bond with the horizontal line as shown in Fig. 5.5(b).

For coplanar anti-parallel dipoles, Eq. 1 can be simplified as:

Structure	β	α	θ	$C_\theta = (1 - 3\cos^2\theta)$
H_2O+ O-terminated	51.75°	16.77°	35.0°	-1.01
H_2O+ F-terminated	51.32°	15.54°	35.8°	-0.97
NO_2+ O-terminated			100°	+0.91

Table 5.2: The angles α, β, θ and the prefactor (C_θ) for H_2O adsorbed on O- and F-terminated graphene edge and NO_2 adsorbed on O- terminated graphene edge

$$\begin{aligned} E_{AP} &= \frac{\mu^2}{4\pi\epsilon_0 r^3}\left(-1 - 3\cos\theta\ \cos(180-\theta)\right) \\ &= -\frac{\mu^2}{4\pi\epsilon_0 r^3}\left(1 - 3\cos^2\theta\right) \\ &= -E_P \end{aligned} \tag{3}$$

where the angle between the anti-parallel dipole and the radial vector is $180 - \theta$ due to symmetry.

The angles α,β and θ for the case of H_2O molecules adsorbed on both O- and F-terminated graphene edges are given in Table 5.2. The calculated value for the dipole prefactor (C_θ) is -1.01 and -0.97 for H_2O adsorbed on O- and F-terminated graphene edge, respectively. These similar values indicate that the energy difference between the molecular dipole–dipole interaction is independent of the type of edge termination. This is consistent with the calculated energies to flip H_2O molecule on O- and F-terminated graphene edges given in Table 5.1 which are also very similar.

In the case of NO_2 adsorbed on an O-terminated edge, the measured θ is given in Table 5.2. The calculated prefactor (C_θ) for this case is +0.909. This positive coefficient is consistent with the anti-parallel ground state determined using DFT.

From these calculations it is clear that the formation of the molecular chain, which is critical for the observation of hysteresis, has a strong dependence on the intermolecular interactions. These intermolecular interactions are independent of the type of edge termination. Therefore, to determine the molecular properties that are important for the formation of these molecular chains, we can consider the molecular chains independently of the nanoribbon.

5.3.2 Model to describe molecular orientation

For molecules with a net dipole moment, intermolecular interactions can be broadly categorized into two types: (1) dipole–dipole interactions which account for all Coulomb-type interactions and (2) H-bonding interactions which also include van der Waals interactions. The ground state of a chain of molecules with a net dipole moment is dependent on a balance between the short range additive interaction terms (H-bonding or van der Waals) and the long range dipole–dipole interaction terms. This competition can be verified using a Monte-Carlo simulation for a system of dipoles with the H-bonding-like interaction modeled as an additive term in addition to the usual dipole dipole interaction given in Eq. 1. A simplified Hamiltonian for such as system, where the co-planar dipoles make an angle θ with the shortest vector joining them as shown in Fig. 5.5, can be given as:

$$\begin{aligned} H &= \frac{C_\theta 2\mu^2}{4\pi\epsilon_0 a^3} \sum_{i,j} \frac{S_i \cdot S_j}{|j-i|^3} + \frac{J_H}{2} \sum_i abs(S_i + S_{i+1}) \\ &= E_b \sum_{i,j} \frac{S_i \cdot S_j}{|j-i|^3} + \frac{J_H}{2} \sum_i abs(S_i + S_{i+1}) \end{aligned} \tag{4}$$

where $S_i = \pm 1$ indicates the dipole orientation, C_θ is the θ-dependent prefactor, μ is the dipole moment, a is the first nearest neighbor distance, J_H is the hydrogen bonding energy and $E_b = \frac{C_\theta 2\mu^2}{4\pi\epsilon_0 a^3}$. The first term in Eq. 4 is the dipole-dipole interaction and the second term is the H-bonding interaction term. The latter additive interaction term only contributes when the adjacent molecules are on the same side of the graphene edge, which corresponds to parallel alignment of molecular dipole moments.

In order to understand the competition between these two interaction terms, we performed Monte Carlo calculations using the Hamiltonian given in Eq. 4. The results are shown in Fig. 5.6 for three values of the additive hydrogen bonding term when $E_b > 0$. A positive dipole–dipole coefficient (E_b) favors anti-parallel alignment of the dipoles and a negative hydrogen bonding coefficient favors parallel alignment of the adjacent dipoles. As expected, when $J_h = 0$ and $C_\theta > 0$ the anti-parallel configuration is the ground state due to the dipole-dipole interaction. This is shown in Fig. 5.6 (top panel). On increasing J_h to $-2E_b$, domains with parallel dipoles are formed as shown in Fig. 5.6 (middle panel). This is because the hydrogen bonding term only affects immediately adjacent dipoles, so they have a tendency for parallel alignment, creating domains. On

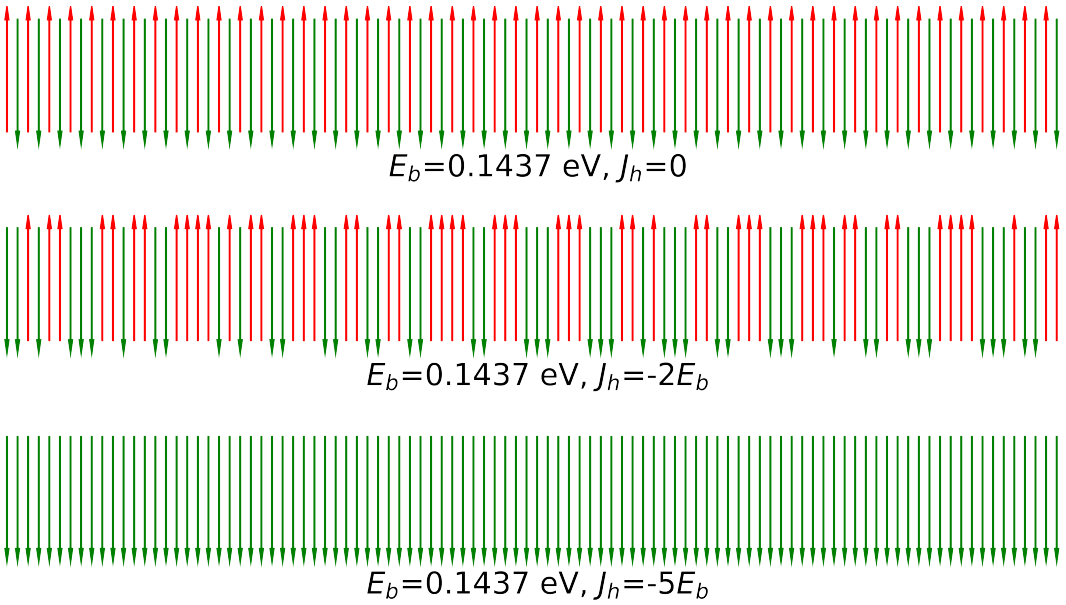

Figure 5.6: Monte-Carlo simulation for chain of dipoles when the first neighbor interaction increases from 0 to -5E_b where $E_b = \frac{C_\theta 2\mu^2}{4\pi\epsilon_0 a^3}$ is the dipole-dipole interaction coefficient.

further increasing J_h to $-5E_b$ all the dipoles align in the parallel configuration. This is because the energy penalty for parallel alignment due to dipole–dipole interactions is completely dominated by the hydrogen bonding energy. When the dipole-dipole interaction coefficient (E_b) is positive, a first nearest neighbor additive interaction with opposite sign to the dipole-dipole interaction coefficient is required to achieve parallel alignment. When $C_\theta < 0$, the ground state is parallel irrespective of the first neighbor interaction.

The parallel ground state orientation of the molecular dipoles is the driving force for the hysteresis as shown in Fig. 5.2. Additionally, the additive first neighbor interaction is responsible for the strength of the observed hysteresis. Free polar molecules will align such that their dipole moment aligns with an external electric field. If the molecules are not free, but instead interact with neighboring molecules, they will remain misaligned to the external field until its magnitude is such that it overcomes the energy penalty associated with breaking the intermolecular interactions. This results in a hysteretic behavior in the alignment of the molecular dipoles with the applied field.

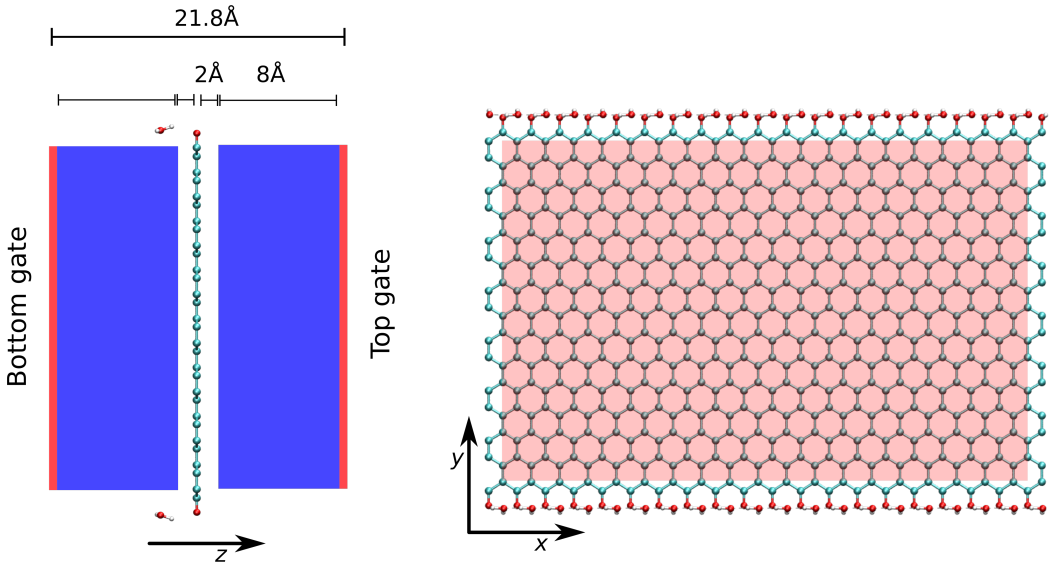

Figure 5.7: (left) Side-view and (right) top view of the gated device structure used in DFT simulations. The red layer indicates the gate constraint and the blue layer indicates the dielectric. The total distance between the gates d_g includes the dielectric smoothing width (0.2 Å), the gate smoothing width (0.2 Å) and the gate width (0.5 Å).

5.3.3 Coupling of the molecular dipoles to an external electric field

To study the interaction between the molecular dipoles and an external field, we apply external gates via Dirichlet boundary conditions in the unit cell. The gated device structure is shown in Fig. 5.7 where the side view is shown on the left and the top view is shown on the right. In the side view, the red layer indicates the gate constraint and the blue layer indicates the gate dielectric region. In the top view, the red box indicates the extent of the applied gate.

On applying a gate voltage, the energy differences between the configurations when the molecules are located above and below the plane of graphene are shown in Fig. 5.8. These configurations correspond to the molecular dipoles oriented parallel and anti-parallel to the external field. This energy difference, ΔE_μ, where μ indicates a molecular dipole moment dependence, shows a linear dependence on the applied voltage, with the slope of line dependent on the type of termination of the graphene edge.

In order to understand this dependence, we first consider how the total energy of a dipole system depends on the gate voltage. The total energy of a dipole, μ, in

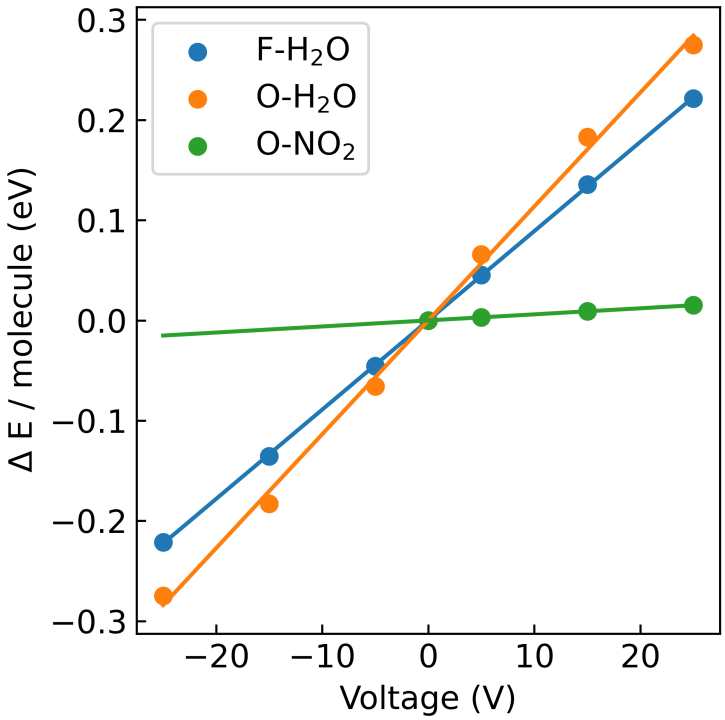

Figure 5.8: Energy differences between the configurations when the molecules are located above and below the plane of graphene as a function of voltage.

an electric field, $\mathcal{E}$, is given by $-\mu \cdot \mathcal{E}$. The electric field depends on the applied voltage, V, and the distance between the gates, d_g, as $\mathcal{E} = \frac{V}{d_g}$. Therefore the final expression for the change in energy of a dipole with the reversal of an applied electric field is given as:

$$\Delta E_\mu = 2\mu \frac{V}{d_g} = \left(2\frac{\mu}{d_g}\right) V \tag{5}$$

The quantity in the brackets can be extracted from the slope in Fig. 5.8 and can be interpreted as an effective charge that interacts with the electric field of the gate. For water adsorbed on the O-terminated device, this quantity is 0.011 e and for water adsorbed on the F-terminated device, this is 0.0089 e. The effective voltage coupling of water dipoles ($E_{\text{eff}} = \frac{\mu}{d_g}$) is therefore 0.0055 e and 0.00445 e for O- and F- terminated graphene, respectively. This quantity can also be calculated using the ideal value of the water dipole moment (1.85D), and the inter gate distance (d_g) of 2.18 nm for the simulated device. This idealized value of 0.017 e is higher than the values derived from a complete device simulation. This indicates a screening of the electric field by the device. This screening is higher in the case of an F-terminated device compared to an O-terminated device.

A higher coupling (E_{eff}) indicates a stronger tendency for the molecules to align to the external field due to the gate voltage. It also means there will be a higher energy penalty associated with any molecules mis-aligned to the electric field. From the calculated values of E_{eff} we can see that molecular dipoles adsorbed on O-terminated graphene edges will have a higher tendency than the molecular dipoles adsorbed on F-terminated graphene edge to flip so that they align to the external electric field.

5.4 Simulating hysteresis effect using an Ising-like model

To study the influence of the gate voltage on the orientation of molecular dipoles on the functionalised edges of graphene, a voltage term can be included in the model Hamiltonian. Using Eq. 4, Eq. 2 and Eq. 3, this Hamiltonian is written as:

$$\begin{aligned} H &= \frac{C_\theta \mu^2}{4\pi\epsilon_0 a^3} \sum_{i=0}^{N-2} \sum_{j=2}^{N} \frac{S_i \cdot S_j}{|j-i|^3} + \frac{J_H}{2} \sum_i abs(S_i + S_{i+1}) - \mu\epsilon \sum_{i=0}^{N-1} z \cdot S_i \\ &= E_b \sum_{i,j} \frac{S_i \cdot S_j}{|j-i|^3} + \frac{J_H}{2} \sum_i abs(S_i + S_{i+1}) - E_{\text{eff}} V \sum_{i=0}^{N-1} z \cdot S_i \end{aligned} \tag{6}$$

where C_θ is the prefactor calculated in Tab. 5.2 and E_{eff} is the effective coupling calculated from the slope of the line in Fig. 5.8. Note that the summation in the dipole term starts from the second nearest neighbor and all first nearest neighbor interactions are included in the additive term via the coefficient J_H. As was shown earlier, the effect of the type of edge termination on the intermolecular interaction is negligible, so, in this modified Hamiltonian the effect of the type of edge termination termination enters only via E_{eff}.

Monte-Carlo simulations can be used to determine the effect of the individual coefficients in the orientation of molecular dipoles. Using the model Hamiltonian also enables us to do a sensitivity analysis for the parameters and study the effect of small variations in the model parameters on the observed hysteresis. The sensitivity analysis will help in understanding the relative importance of each of the interaction terms, and in determining whether some effects can be ignored. The Monte-Carlo simulation is performed at T = 300 K (25 meV) for a molecular chain of size 100. The voltage is varied from -35 V to +35 V in increments

of 1 V. At each voltage, the entire chain is looped over 8000 times of which last 2000 iterations are used to calculate the average orientation of the dipoles in the molecular chain. The starting configuration for each voltage is the last configuration of the previous voltage, with the initialization at $V = -35$ V done randomly. As we are interested in the relative importance of the interaction terms, we fix the value of $C_\theta = -1$ to preserve the appropriate sign of the interaction, and give all energies in the units of E_b. This reduces the number of parameters to two, namely J_H and E_{eff}.

Note that if C_θ was positive, the adjacent dipole moments of molecules align anti-parallel to one another as shown in Fig. 5.6 (top panel). Due to this anti-parallel alignment the effect of the molecules on the graphene electron density cancels each other, so no hysteresis is observed. In contrast, if C_θ and J_H are both negative, the dipoles of the molecules in the molecular chains have a tendency to align such that their dipole moments are parallel to each other. In such cases the effect of the voltage is then to reorient these molecular dipoles to the external field. Ideally, for an isolated dipole present in an external field, the dipole reorients in the direction of external electric field for any non-zero value of that field. However, for multiple interacting dipoles the orientation is decided by a competition between the dipole–electric field interaction and dipole–dipole interactions. In such cases, if the energy gain due to a dipole reorientation is not sufficient to compensate for the reduction in inter-dipole interactions, the alignment of the dipole to the external field will be prohibited until a sufficiently high field is reached. This is the cause of the experimentally-observed hysteresis. To study this competition, we use Monte-Carlo simulations to determine the average orientation of the molecules with an externally applied voltage. Note that the model is agnostic to the starting alignment of the molecules to the external field, so simulations can be limited to only one direction where the molecules are initially aligned in an external field (V=-35 V). The voltage is then swept to V=35 V) in steps of 1 V. Hysteretic behavior will be evident if the molecular dipoles do not immediately align in the direction of the applied field (i.e., when the applied field changes from negative to positive values). The symmetry of the calculation means that it is not necessary to also consider sweeping the voltage from positive to negative (the result will differ only in sign).

The simulated hysteresis is shown in Fig. 5.9 as a function of the changing additive coefficient J_H and the effective field coupling E_{eff} in units of E_b. As expected, when the additive coefficient is small ($J_H = 0.5$) the molecular dipoles follow the external voltage very closely. This is because the interdipolar interaction is

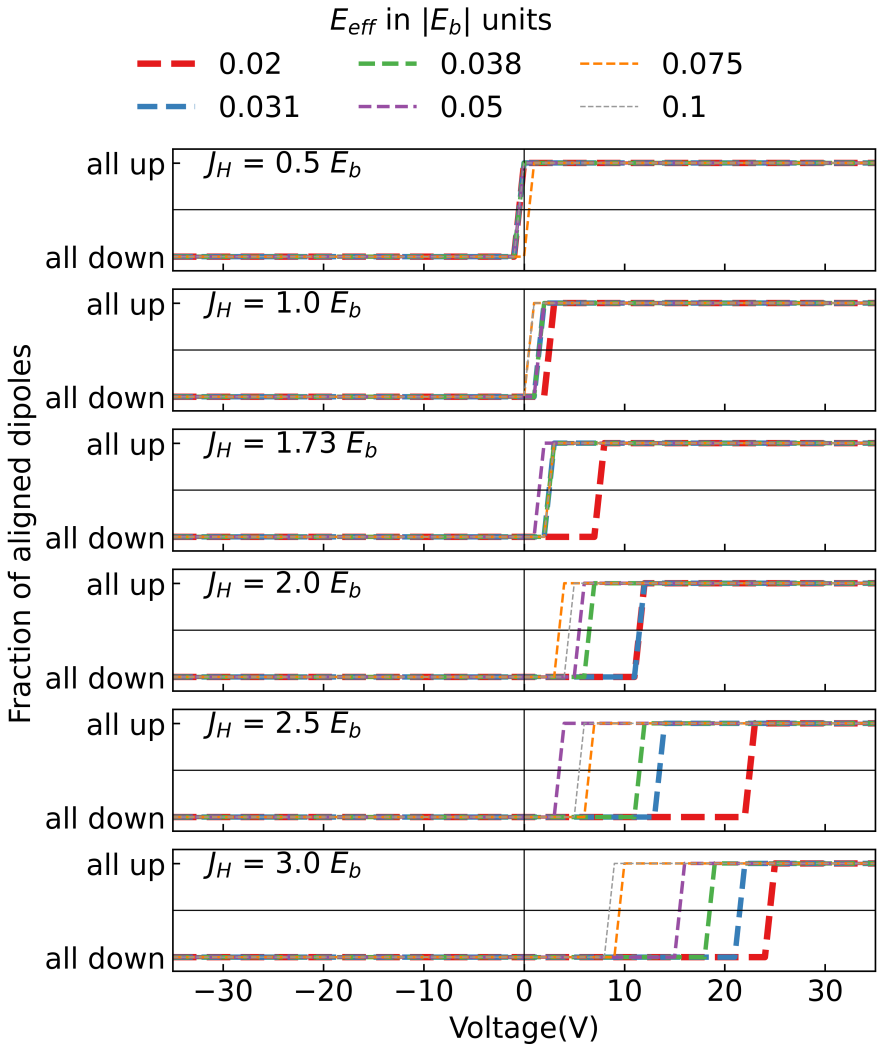

Figure 5.9: Result of Monte-Carlo simulation demonstrating a hysteresis with varying model parameters J_H and E_{eff}. Note that $E_b < 0$ and so is J_H.

small in comparison to the dipole–field interaction. For a given value of E_{eff}, on increasing the magnitude of J_H (moving down the panels) increasing hysteresis is observed. For example, when E_{eff} is fixed at 0.031, a voltage of 0 V is required to flip the molecular orientations when J_H is $0.5E_b$, but this increases to a voltage of 13 V when J_H is increased to $2E_b$. For a given J_H, there is not a monotonic relationship between E_{eff} and the voltage required to flip the chain orientation. For example, $J_H = 3.0E_b$, decreasing E_{eff} from $0.1|E_b|$ to $0.02|E_b|$, increases the voltage required to flip the molecular dipoles monotonically from 8 V to 24 V. This is not the case when J_H is $1.73E_b$ where the transition voltage first appears to decrease then increase slightly.

We can extract values of J_H and E_{eff} associated with water molecules adsorbed on O- and F- terminated graphene edges from our DFT calculations. These

Termination	$\|E_b\|$(eV)	J_H (eV)	E_{eff} (e)
F	0.1437	-0.27	0.0045
O	0.1437	-0.25	0.0055

Table 5.3: The values of the model parameters extracted from DFT for the concentration of one H_2O molecule per functional edge atom.

values are listed in Table 5.3. However, there is very little difference in the values extracted for these two cases, with $J_H \approx -1.73|E_b|$ and $\approx -1.84|E_b|$ for F- and O-terminated edges, respectively, and $E_{eff} = 0.03|E_b|$ and $0.038|E_b|$ for F- and O-terminated edges, respectively. For these extracted values, our Monte-Carlo simulations predict a very similar hysteresis effect for both O- and F- terminations. This is in contrast to the experimental result, which finds that H_2O adsorbed on an O-terminated graphene edge demonstrates a larger hysteresis compared to H_2O adsorbed on a F-terminated graphene edge. This may be due to the dependence of the calculated parameters on both the concentration and orientation of optimized molecules. Further calculations are required to determine the accuracy of the molecular concentrations enforced here, namely one molecule per terminating atom. Changing the adsorption concentration would change the hydrogen bonding and vdW interactions between neighboring molecules, i.e., it would modify J_H. If different concentrations of water adsorb on O- and F- terminations, this could explain the difference in the experimental hysteresis measurement.

5.5 Conclusion

DFT calculations show that H_2O molecules adsorbed on both O- and F-terminated graphene edges have a parallel ground state where all the molecules are located on the same side of the graphene plane. In contrast, NO_2 molecules adsorb on an O-terminated graphene edge in an anti-parallel configuration so that alternate molecules adsorb on the opposite sides of the graphene plane. The effect of the termination type on the inter-molecular interaction is negligible, with the role of edge limited to providing binding sites for adsorption. The intermolecular interaction then dictates the edge dependent orientation of the molecules. The coupling of the molecules to the external electric field due to the applied gate voltage is dependent on the edge termination, with F-terminations showing a higher screening of the electric field compared the O-terminated edge.

We performed Monte Carlo simulations on the 1-dimensional Ising-like model to study the relative importance of these interactions. We find that in order to observe a hysteresis effect, both an H-bonding additive first nearest neighbor interaction and a dipole - field interaction are required. The hysteresis transition voltage will depend on a fine balance between these two interactions. These interaction parameters are in turn sensitive to the molecular orientation and concentration. Determining the correct molecular concentration on the edge is therefore crucial. For the correct concentration, the orientation will then determine the correct values for the model parameters. We extracted the values of these interaction parameters using DFT calculations. However, for the fixed values of adsorption concentration considered here, these parameters are very similar for water adsorbed on O- and F-terminated graphene, and so could not be used to explain the experimental result. Further work will be required to determine a realistic adsorption water concentration on the edges of an O- and F-terminated graphene flake.

CHAPTER

6

CONCLUSIONS AND FUTURE WORK

6.1 Conclusion

Two dimensional materials are used in a variety of applications due to their wide ranging properties. Solvents play a very important role for the production of these materials. These production processes are complex multi-step processes with many steps occurring simultaneously. Liquid phase exfoliation (LPE) is one such solution-processing method capable of industrial scale production. Here, layers are separated by the application of an external force. The solvent molecules then prevent the resulting monolayers from reaggregation, stabilizing the layers in the solvent. It is generally assumed that these solvents do not interact strongly with the layer and so their effects can be neglected. Yet experimental evidence has suggested that explicit atomic-scale interactions between the solvent and layered material may play a crucial role in exfoliation and cause unintended electronic changes in the layer. An atomic level understanding of these processes is necessary in order to make predictions or optimizations. This atomic level understanding can be developed using modern computational tools.

Research in exfoliation of graphene and other two dimensional layers in solvents is mainly focused on determining the factors affecting the amount of exfoliated layers in the solution. One important ingredient that is known to affect the exfoliation procedure is the type of solvent that is used. Determining the type of solvent to use is an open question and a method for the screening of solvent molecules is desirable. Several attempts have been made in this regard based on solubility parameters and surface energies. However, these methods fail to provide definitive predictions. All these methods are based on effective parameters. It is clear that atomic-level understanding of the process is necessary for development of an effective screening procedure. In the case of graphene, the van der Waals interactions between the layer and the molecule are weak in nature. Therefore they are often neglected. However, their collective behavior near the surface is distinguishable, indicated via the diffusion coefficient and the free energy of formation of the solvation structure. This difference in the diffusion of molecules near the surface of the graphene layer indirectly affects the reaggregation process, and hence the graphene concentration in the dispersion. This atomic level understanding is also necessary for other systems involving molecules and graphene layers such as in determining the co-intercalation of metal ions and solvent molecules betwee the layers.

In Chapter 2, we introduced the electronic structure methods used in this thesis, namely-density functional theory (DFT) and classical molecular dynamics (MD), and discussed their practical implementation. We also defined several important properties, including the permittivity, free solvation energies and diffusion coefficients, and showed how they can be extracted from DFT and MD calculations.

In Chapter 3, we discussed the interaction of experimentally-relevant solvent molecules with graphene and MoS_2. Using DFT, we show that the interaction of these solvents is van der Waals in nature. The binding energies and binding heights of molecules adsorbed on both graphene and MoS_2 do not depend strongly on the type of molecule or nanosheet under consideration. The orientation of the molecules also show a preference towards Bernal stacking, where molecules with hexagonal rings prefer AB style stacking with respect to the graphene layer. We also show that a counter dipole moment is induced on the layers in response to the dipole moment of the molecules. We show that the solvent-dependence of liquid phase exfoliation cannot be attributed to any difference in the molecule–layer interaction. We then simulate the bulk liquid

solvent near monolayer graphene using classical MD. These simulations show the formation of distinct solvation shells in all cases, irrespective of the type of the solvent molecules. The molecules in the first solvation shell show a strong out-of-plane ordering, with two different preferential orientations. However, there is negligible in-plane ordering of the molecules, irrespective of the type of the solvent. The formation of these solvation shells is energetically favorable as indicated by the free energy of formation and its decomposition into the enthalpic and entropic contributions. These calculations indicate that the solvent dependence of the LPE process may not be due to thermodynamic considerations alone and instead the kinetic behavior of molecules may be important. To verify this, we calculated the diffusion coefficient of the molecules in the first solvation shell. We found that a higher diffusion coefficient is associated with a lower experimental concentration of graphene in the dispersion. This could be due to the higher reaggregation rate in these cases, as intercalated solvent molecules are easily ejected. However, this breaks down when the diffusion coefficient is very low. This could be due to the separation step of the exfoliation process. The role of the solvent in the initial separation step should be considered in more detail. This also provides a method to screen solvent molecules for which the exfoliation process can be optimized to achieve higher concentration of graphene in the dispersion.

In Chapter 4, we discussed the exfoliation process in the presence of Group-1 metal ions. We find that potassium intercalated bilayers spontaneously separate into monolayers in the presence of polar solvents. This can be attributed to the transfer of charge from the ions to the layers. This separation is spontaneous only when the separated layers retain a residual charge. In contrast, separation into neutral layers will not be spontaneous. Excess charge can induce structural and electronic phase transitions in some monolayers. This is case for Group-VI transition metal dichalcogenides. The extent to which this occurs depends on the chemical composition of the material. We explain this by calculating the forward transition barrier for charged layers and reverse transition barrier for neutral layers. Finally, we developed a computational workflow to determine whether it is energetically favorable for particular molecules to intercalate alone or to co-intercalate with a metal ion in bilayer graphene. The work-flow considers all the possible intercalation configurations while considering the symmetry of the molecules to eliminate duplicate structures, hence reducing the computational cost. Preferentially obtaining one of these outcomes is important for applications in exfoliation or battery electrodes.

In Chapter 5, we discussed the formation and manipulation of molecular chains on a functionalised graphene edge in order to understand an experimentally-observed ferroelectric-like hysteresis effect in the resistance of the graphene sheet. We find that in order for the hysteresis effect to occur, an additive interaction between first nearest neighbors is necessary in addition to the molecular dipole-dipole interaction. We find that H_2O molecules adsorbed on the either an O- or F-terminated graphene edge have a parallel ground state, where all the molecules are on the same side of the graphene plane. In the case of NO_2 adsorbed on an O-terminated graphene edge the ground state is anti-parallel, with alternate molecules present on opposite side of the graphene plane. The intermolecular interaction is not affected by the edge, with the role of edge limited to orienting the molecules into a chain. In contrast the edge has a significant effect on the interaction of the molecules with an external field, with fluorine terminations showing a higher screening as compared to oxygen. Monte-Carlo simulations for a 1D Ising-like model show that both the additive H-bonding and the dipole-field interactions are important. The hysteresis in this case depends on a fine balance between these two interactions. The model parameters derived using DFT are very similar for H_2O adsorbed on the either a O- or F-terminated graphene edge, so the Monte-Carlo results are inconclusive. As the model parameters will depend sensitively on both the concentration and the orientation of the molecules, further investigations are required to determine the correct adsorption concentration and associated molecule orientation.

6.2 Future Work

The work here can be extended in several ways:

In Chapter 3 we determined the potential energy surface (PES) for a molecule-layer interaction. Determining the PES for a molecule-layer interaction is computationally very expensive. The PES is a tool to study the adoption of molecules or ions on the basal plane of the layer or on the edge. This is important as the adsorbate position has a direct influence on properties such as transport, spintronic effects and optical behavior. The determination of the adsorption sites can be accelerated using tools such as ab-initio molecular dynamics (AIMD) and machine learning [281].

The hypothesis that solvents with high diffusion rates on the surface of graphene are better solvents for LPE can be further tested for other materials

and for a bigger set of molecules. Furthermore, classical MD simulations require accurate potentials to represent interactions within the system. For the calculations presented in this thesis, the potentials were chosen carefully to reproduce, for example, the van der Waals interactions between molecules and monolayers. This limits the generalization of this method due to absence of a universal potential type that can be used irrespective of the interaction-type. An interesting candidate for such a universal potential is one developed using machine learning [111, 282]. This potential can be trained using DFT calculations for a subset of representative interactions. Then used to simulate large simulations at the same level of accuracy as the DFT calculations. In addition it should also be seen if the diffusion coefficient calculated for an isolated or a thin slab of molecules on the graphene layer agrees with that calculated for the thicker solvent layer considered in this thesis. If so, the computational cost for screening of molecules will be much lower. Furthermore, if this behavior can be replicated in smaller systems, then ab-initio molecular dynamics can be directly used, removing the requirement for alternate methods or potentials. With this method we can also include the possibility that the edges and molecule chemically interact to form bonds. Then this can then be used to determine if the behavior of the molecules changes in the vicinity of the edge. To make these calculations computationally tractable we can use QM/MM [283] or subsystem DFT methods [284].

In Chapter 4, we calculated the transition barriers for the structural phase transition between two stable states of Group-6 TMD's. There we assumed that the phase transition occures simultaneously for the complete layer. In reality, this will not be the case. The transition will occur in cascading steps where a portion of the layer transitions at a time. This behavior can be simulated using a flake rather than a small periodic structure. These type of simulations have just become computationally possible using modern linear scaling DFT methods. For a non-periodic structure, dealing with a charged surface is also not a problem, and the role of lithium in the simulation can also be eliminated. Another possibility for the direct charging can be to use the non-periodic boundary conditions using real space Poisson solvers. Additionally, machine learning potentials can also be used. With appropriate training these can be used to correctly determine the transition state structure [111]. This would enable simulations of much larger flakes than those possible using DFT.

We have demonstrated a framework for testing molecules for cointercalation. This framework can be improved, and applied to other materials and concentrations.

In this thesis we have considered one molecule and ion interacting with bilayer graphene. The ability to deal with increasing concentrations is very important to study experimentally relevant systems. In addition to the framework discussed here, this can also be achieved using AIMD simulations. This will also enable us to include the rest of the solvent and study its effect on the process of co-intercalation. In reality the intercalated ions move from the solution to between the layers. This would allow us to study the effect of the initial ion concentration in solution on the intercalated concentration. Furthermore, AIMD calculations would enable us to include the effect of edges, which could play a very important role.

In Chapter 5, we have shown that, in the case of molecules adsorbed on functionalised graphene edges, the results depend on the molecular orientations. Here, we have considered only two distinct orientations of molecules. This was enforced via the periodicity of the unit cell. To determine a more realistic configuration of a chain of molecules near a graphene edge, we can perform molecular dynamics simulations which consider different coverages. These simulations can be done for different lengths of unit cell and with different coverages to get the correct orientations. Another interesting alternative is to use grand-canonical Monte-Carlo along with DFT to determine the concentration and orientation of molecules near the edge. Once the ground state orientations are determined we can do molecular dynamics simulations to determine how fast can the molecules be switched in between the two states with the external voltage.

BIBLIOGRAPHY

[1] I. Persson, N. Armakavicius, C. Bouhafs, V. Stanishev, P. Kühne, T. Hofmann, M. Schubert, J. Rosen, R. Yakimova, P. O. Persson, *et al.*, APL Materials **8**(1), 011104 (2020).

[2] K. S. Novoselov, A. K. Geim, S. V. Morozov, D. Jiang, Y. Zhang, S. V. Dubonos, I. V. Grigorieva, and A. A. Firsov, science **306**(5696), 666–669 (2004).

[3] C. Lee, X. Wei, J. W. Kysar, and J. Hone, science **321**(5887), 385–388 (2008).

[4] J.-H. Chen, C. Jang, S. Xiao, M. Ishigami, and M. S. Fuhrer, Nature nanotechnology **3**(4), 206–209 (2008).

[5] K. S. Novoselov, Rev. Mod. Phys. **83**, 837–849 August (2011).

[6] B. Radisavljevic, A. Radenovic, J. Brivio, V. Giacometti, and A. Kis, Nature nanotechnology **6**(3), 147–150 (2011).

[7] X. Wang, L. Zhi, and K. Müllen, Nano letters **8**(1), 323–327 (2008).

[8] F. Shahzad, M. Alhabeb, C. B. Hatter, B. Anasori, S. M. Hong, C. M. Koo, and Y. Gogotsi, Science **353**(6304), 1137–1140 (2016).

[9] W. Yang, L. Gan, H. Li, and T. Zhai, Inorg. Chem. Front. **3**(4), 433–451 (2016).

[10] P. V. Kamat, ACS Energy Letters **4**(11), 2757–2759 (2019).

[11] A. Ambrosi, Z. Sofer, and M. Pumera, Chemical Communications **51**(40), 8450–8453 (2015).

[12] N. Rohaizad, C. C. Mayorga-Martinez, Z. Sofer, and M. Pumera, ACS applied materials & interfaces **9**(46), 40697–40706 (2017).

[13] S. V. Boriskina, M. A. Green, K. Catchpole, E. Yablonovitch, M. C. Beard, Y. Okada, S. Lany, T. Gershon, A. Zakutayev, M. H. Tahersima, *et al.*, Journal of Optics **18**(7), 073004 (2016).

[14] E. G. da Silveira Firmiano, A. C. Rabelo, C. J. Dalmaschio, A. N. Pinheiro, E. C. Pereira, W. H. Schreiner, and E. R. Leite, Advanced Energy Materials **4**(6), 1301380–n/a (2014), 1301380.

[15] H. Hwang, H. Kim, and J. Cho, Nano Letters **11**(11), 4826–4830 (2011).

[16] X. Li, M. Zhu, M. Du, Z. Lv, L. Zhang, Y. Li, Y. Yang, T. Yang, X. Li, K. Wang, *et al.*, Small **12**(5), 595–601 (2016).

[17] Y. Cao, V. Fatemi, S. Fang, K. Watanabe, T. Taniguchi, E. Kaxiras, and P. Jarillo-Herrero, Nature **556**(7699), 43–50 (2018).

[18] Y. Liu, I. Yudhistira, M. Yang, E. Laksono, Y. Z. Luo, J. Chen, J. Lu, Y. P. Feng, S. Adam, and K. P. Loh, Nano letters **18**(6), 3377–3383 (2018).

[19] J. Wang, R. Jia, Q. Huang, C. Pan, J. Zhu, H. Wang, C. Chen, Y. Zhang, Y. Yang, H. Song, *et al.*, Scientific reports **8**(1), 1–9 (2018).

[20] C. Zhang, C.-P. Chuu, X. Ren, M.-Y. Li, L.-J. Li, C. Jin, M.-Y. Chou, and C.-K. Shih, Science advances **3**(1), e1601459 (2017).

[21] J. Cai, P. Ruffieux, R. Jaafar, M. Bieri, T. Braun, S. Blankenburg, M. Muoth, A. P. Seitsonen, M. Saleh, X. Feng, *et al.*, Nature **466**(7305), 470–473 (2010).

[22] B. Deng, Z. Liu, and H. Peng, Advanced Materials **31**(9), 1800996 (2019).

[23] W. Choi, N. Choudhary, G. H. Han, J. Park, D. Akinwande, and Y. H. Lee, Materials Today **20**(3), 116–130 (2017).

[24] J. Yu, J. Li, W. Zhang, and H. Chang, Chemical Science **6**(12), 6705–6716 (2015).

[25] M. Lenner, A. Kaplan, C. Huchon, and R. E. Palmer, Physical Review B **79**(18), 184105 (2009).

[26] F. Carbone, P. Baum, P. Rudolf, and A. H. Zewail, Physical review letters **100**(3), 035501 (2008).

[27] V. Nicolosi, M. Chhowalla, M. G. Kanatzidis, M. S. Strano, and J. N. Coleman, Science **340**(6139), 1226419 (2013).

[28] J. N. Coleman, Accounts of Chemical Research **46**(1), 14–22 (2013), PMID: 22433117.

[29] K. R. Paton, E. Varrla, C. Backes, R. J. Smith, U. Khan, A. O'Neill, C. Boland, M. Lotya, O. M. Istrate, P. King, T. Higgins, S. Barwich, P. May, P. Puczkarski, I. Ahmed, M. Moebius, H. Pettersson, E. Long, J. Coelho, S. E. O'Brien, E. K. McGuire, B. M. Sanchez, G. S. Duesberg, N. McEvoy, T. J. Pennycook, C. Downing, A. Crossley, V. Nicolosi, and J. N. Coleman, Nature Materials **13**(6), 624 (2014).

[30] U. Khan, A. O'Neill, H. Porwal, P. May, K. Nawaz, and J. N. Coleman, Carbon **50**(2), 470 (2012).

[31] A. O'Neill, U. Khan, and J. N. Coleman, Chemistry of Materials **24**(12), 2414 (2012).

[32] J. Coleman *et al.*, Science **331**(6017), 568–571 (2011).

[33] H. Tao, Y. Zhang, Y. Gao, Z. Sun, C. Yan, and J. Texter, Phys. Chem. Chem. Phys. **19**, 921 (2016).

[34] U. Khan, H. Porwal, A. O'Neill, K. Nawaz, P. May, and J. N. Coleman, Langmuir **27**(15), 9077–9082 (2011).

[35] P. L. Cullen, K. M. Cox, M. K. Bin Subhan, L. Picco, O. D. Payton, D. J. Buckley, T. S. Miller, S. A. Hodge, N. T. Skipper, V. Tileli, and C. A. Howard, Nature Chemistry **9**, 244 (2017).

[36] X. Fan, P. Xu, D. Zhou, Y. Sun, Y. C. Li, M. A. T. Nguyen, M. Terrones, and T. E. Mallouk, Nano letters **15**(9), 5956–5960 (2015).

[37] S. Ravula, S. N. Baker, G. Kamath, and G. A. Baker, Nanoscale **7**(10), 4338–4353 (2015).

[38] D. Voiry, A. Mohite, and M. Chhowalla, Chemical Society Reviews **44**(9), 2702 (2015).

[39] F. Gamble, Journal of Solid State Chemistry **9**(4), 358–367 (1974).

[40] M. Py and R. Haering, Canadian Journal of Physics **61**(1), 76–84 (1983).

[41] L. Wang, Z. Xu, W. Wang, and X. Bai, Journal of the American Chemical Society **136**(18), 6693–6697 (2014).

[42] B. Lei, Y. Pan, Z. Hu, J. Zhang, D. Xiang, Y. Zheng, R. Guo, C. Han, L. Wang, J. Lu, *et al.*, ACS nano **12**(2), 2070–2077 (2018).

[43] X. Zhang, A. C. Coleman, N. Katsonis, W. R. Browne, B. J. Van Wees, and B. L. Feringa, Chemical Communications **46**(40), 7539–7541 (2010).

[44] Y. T. Liang and M. C. Hersam, Journal of the American Chemical Society **132**(50), 17661–17663 (2010).

[45] J. Li, F. Ye, S. Vaziri, M. Muhammed, M. C. Lemme, and M. Östling, Carbon **50**(8), 3113–3116 (2012).

[46] N. Mounet, M. Gibertini, P. Schwaller, D. Campi, A. Merkys, A. Marrazzo, T. Sohier, I. E. Castelli, A. Cepellotti, G. Pizzi, *et al.*, Nature nanotechnology **13**(3), 246–252 (2018).

[47] S. Haastrup, M. Strange, M. Pandey, T. Deilmann, P. S. Schmidt, N. F. Hinsche, M. N. Gjerding, D. Torelli, P. M. Larsen, A. C. Riis-Jensen, *et al.*, 2D Materials **5**(4), 042002 (2018).

[48] J. Xu, D. K. Dang, V. T. Tran, X. Liu, J. S. Chung, S. H. Hur, W. M. Choi, E. J. Kim, and P. A. Kohl, Journal of Colloid and Interface Science **418**, 37 (2014).

[49] V. Sresht, A. A. Pádua, and D. Blankschtein, ACS nano **9**(8), 8255 (2015).

[50] J. M. Caridad, G. Calogero, P. Pedrinazzi, J. E. Santos, A. Impellizzeri, T. Gunst, T. J. Booth, R. Sordan, P. Bøggild, and M. Brandbyge, Nano letters **18**(8), 4675–4683 (2018).

[51] E. Schrödinger, *Collected papers on wave mechanics*, volume 302, American Mathematical Soc., (2003).

[52] R. M. Martin, *Electronic structure: basic theory and practical methods*, Cambridge university press, (2020).

[53] K. Burke, *The ABC of DFT*.

[54] M. Born and R. Oppenheimer, Annalen der physik **389**(20), 457–484 (1927).

[55] J. M. Ziman, *Principles of the Theory of Solids*, Cambridge university press, (1972).

[56] P. Hohenberg and W. Kohn, Phys. Rev. **136**, B864–B871 November (1964).

[57] M. Levy and J. P. Perdew, The constrained search formulation of density functional theory, In *Density functional methods in physics*, 11–30. Springer (1985).

[58] W. Kohn and L. J. Sham, Phys. Rev. **140**, A1133–A1138 November (1965).

[59] P. E. Blöchl, Physical review B **50**(24), 17953 (1994).

[60] R. Ditchfield, W. J. Hehre, and J. A. Pople, The Journal of Chemical Physics **54**(2), 724–728 (1971).

[61] G. Lippert, J. Hutter, and M. Parinello, Molecular Physics **92**(3), 477–488 (1997).

[62] V. Blum, R. Gehrke, F. Hanke, P. Havu, V. Havu, X. Ren, K. Reuter, and M. Scheffler, Computer Physics Communications **180**(11), 2175–2196 (2009).

[63] G. Kresse and D. Joubert, Phys. Rev. B **59**, 1758–1775 January (1999).

[64] C. Rostgaard, arXiv preprint arXiv:0910.1921 (2009).

[65] Vasp: Basics. `https://www.nersc.gov/assets/Uploads/VASP-lecture-Basics.pdf`.

[66] J. P. Perdew and K. Schmidt, Jacob's ladder of density functional approximations for the exchange-correlation energy, In *AIP Conference Proceedings*, volume 577, 1–20. American Institute of Physics, (2001).

[67] J. P. Perdew, K. Burke, and M. Ernzerhof, Physical review letters **77**(18), 3865 (1996).

[68] P. Borlido, T. Aull, A. W. Huran, F. Tran, M. A. Marques, and S. Botti, Journal of chemical theory and computation **15**(9), 5069–5079 (2019).

[69] K. Berland, V. R. Cooper, K. Lee, E. Schröder, T. Thonhauser, P. Hyldgaard, and B. I. Lundqvist, Reports on Progress in Physics **78**(6), 066501 (2015).

[70] G. Graziano, J. Klimeš, F. Fernandez-Alonso, and A. Michaelides, Journal of Physics: Condensed Matter **24**(42), 424216 (2012).

[71] S. Grimme, Journal of computational chemistry **27**(15), 1787–1799 (2006).

[72] S. Grimme, J. Antony, S. Ehrlich, and H. Krieg, The Journal of chemical physics **132**(15), 154104 (2010).

[73] S. Grimme, S. Ehrlich, and L. Goerigk, Journal of computational chemistry **32**(7), 1456–1465 (2011).

[74] A. Tkatchenko and M. Scheffler, Physical review letters **102**(7), 073005 (2009).

[75] A. Tkatchenko, R. A. DiStasio Jr, R. Car, and M. Scheffler, Physical review letters **108**(23), 236402 (2012).

[76] A. Ambrosetti, A. M. Reilly, R. A. DiStasio Jr, and A. Tkatchenko, The Journal of chemical physics **140**(18), 18A508 (2014).

[77] M. Dion, H. Rydberg, E. Schröder, D. C. Langreth, and B. I. Lundqvist, Phys. Rev. Lett. **92**, 246401 June (2004).

[78] J. Klimeš, D. R. Bowler, and A. Michaelides, Journal of Physics: Condensed Matter **22**(2), 022201 (2010).

[79] K. Lee, É. D. Murray, L. Kong, B. I. Lundqvist, and D. C. Langreth, Physical Review B **82**(8), 081101 (2010).

[80] I. Hamada, Physical Review B **89**(12), 121103 (2014).

[81] T. Björkman, The Journal of chemical physics **141**(7), 074708 (2014).

[82] J. c. v. Klimeš, D. R. Bowler, and A. Michaelides, Phys. Rev. B **83**, 195131 (2011).

[83] J. Neugebauer and M. Scheffler, Phys. Rev. B **46**, 16067–16080 December (1992).

[84] G. Makov and M. C. Payne, Phys. Rev. B **51**, 4014–4022 February (1995).

[85] M. Topsakal and S. Ciraci, Applied Physics Letters **98**(13), 131908 (2011).

[86] O. Andreussi and N. Marzari, Phys. Rev. B **90**, 245101 December (2014).

[87] O. Andreussi, I. Dabo, and N. Marzari, The Journal of Chemical Physics **136**(6), 64102 (2012).

[88] G. J. Martyna and M. E. Tuckerman, The Journal of chemical physics **110**(6), 2810–2821 (1999).

[89] L. Genovese, T. Deutsch, A. Neelov, S. Goedecker, and G. Beylkin, The Journal of chemical physics **125**(7), 074105 (2006).

[90] L. Genovese, T. Deutsch, and S. Goedecker, The Journal of Chemical Physics **127**(5), 054704 (2007).

[91] M. Otani and O. Sugino, Physical Review B **73**(11), 115407 (2006).

[92] T. Sohier, M. Calandra, and F. Mauri, Physical Review B **96**(7), 075448 (2017).

[93] F. Giustino and A. Pasquarello, Physical Review B **71**(14), 144104 (2005).

[94] P. Kumar, B. Bhadoria, S. Kumar, S. Bhowmick, Y. S. Chauhan, and A. Agarwal, Physical Review B **93**(19), 195428 (2016).

[95] H. Jónsson, G. Mills, and K. W. Jacobsen, Nudged elastic band method for finding minimum energy paths of transitions, In *CLassical and Quantum Dynamics in Condensed Phase Simulations*, 385–404, June (1998).

[96] G. Henkelman, B. P. Uberuaga, and H. Jónsson, The Journal of chemical physics **113**(22), 9901–9904 (2000).

[97] T. Gunst, K. Kaasbjerg, and M. Brandbyge, Physical Review Letters **118**(4), 046601 (2017).

[98] M. H. Bani-Hashemian, S. Brück, M. Luisier, and J. VandeVondele, The Journal of chemical physics **144**(4), 044113 (2016).

[99] J. Tomasi, B. Mennucci, and R. Cammi, Chemical Reviews **105**(8), 2999–3094 (2005).

[100] K. Mathew, R. Sundararaman, K. Letchworth-Weaver, T. A. Arias, and R. G. Hennig, The Journal of Chemical Physics **140**(8), 84106 (2014).

[101] M. Levy, Proceedings of the National Academy of Sciences **76**(12), 6062–6065 (1979).

[102] M. Cococcioni, F. Mauri, G. Ceder, and N. Marzari, Phys. Rev. Lett. **94**, 145501 April (2005).

[103] H. H. Uhlig, The Journal of Physical Chemistry **41**(9), 1215–1226 (1937).

[104] C. Dupont, O. Andreussi, and N. Marzari, Journal of Chemical Physics **139**(21), 1–9 (2013).

[105] D. Marx and J. Hutter, *Ab initio molecular dynamics: basic theory and advanced methods*, Cambridge University Press, (2009).

[106] L. Verlet, Physical review **159**(1), 98 (1967).

[107] W. C. Swope, H. C. Andersen, P. H. Berens, and K. R. Wilson, The Journal of chemical physics **76**(1), 637–649 (1982).

[108] W. L. Jorgensen, D. S. Maxwell, and J. Tirado-Rives, Journal of the American Chemical Society **118**(45), 11225–11236 (1996).

[109] W. L. Jorgensen, J. Chandrasekhar, J. D. Madura, R. W. Impey, and M. L. Klein, The Journal of chemical physics **79**(2), 926–935 (1983).

[110] K. Chenoweth, A. C. Van Duin, and W. A. Goddard, The Journal of Physical Chemistry A **112**(5), 1040–1053 (2008).

[111] A. P. Thompson, L. P. Swiler, C. R. Trott, S. M. Foiles, and G. J. Tucker, Journal of Computational Physics **285**, 316–330 (2015).

[112] H. Lorentz, Annalen der physik **248**(1), 127–136 (1881).

[113] G. Mie, Annalen der Physik **316**(8), 657–697 (1903).

[114] D. Berthelot, Compt. Rendus **126**, 1703–1706 (1898).

[115] R. W. Zwanzig, The Journal of Chemical Physics **22**(8), 1420–1426 (1954).

[116] M. Mezei, The Journal of chemical physics **86**(12), 7084–7088 (1987).

[117] J. G. Kirkwood, The Journal of chemical physics **3**(5), 300–313 (1935).

[118] W. L. Jorgensen and C. Ravimohan, The Journal of chemical physics **83**(6), 3050–3054 (1985).

[119] D. M. Eike and E. J. Maginn, The Journal of chemical physics **124**(16), 164503 (2006).

[120] G. Duarte Ramos Matos, D. Y. Kyu, H. H. Loeffler, J. D. Chodera, M. R. Shirts, and D. L. Mobley, Journal of Chemical & Engineering Data **62**(5), 1559–1569 (2017).

[121] K. Schulten and I. Kosztin, University of Illinois **117** (2000).

[122] V. M. v. Smoluchowski and I. D. im unbegrenzten Raum, Ann. d. Phys **21**, 756 (1906).

[123] A. Einstein, Annalen der physik **4** (1905).

[124] L. Agosta, E. G. Brandt, and A. P. Lyubartsev, The Journal of Chemical Physics **147**(2), 024704 (2017).

[125] P. Liu, E. Harder, and B. Berne, The Journal of Physical Chemistry B **108**(21), 6595–6602 (2004).

[126] L. Dong, Z. Chen, X. Zhao, J. Ma, S. Lin, M. Li, Y. Bao, L. Chu, K. Leng, H. Lu, *et al.*, Nature communications **9**(1), 1–8 (2018).

[127] Y. Wei and Z. Sun, Current opinion in colloid & interface science **20**(5-6), 311–321 (2015).

[128] M. Yi and Z. Shen, Carbon **78**, 622–626 (2014).

[129] J. T. Han, J. I. Jang, H. Kim, J. Y. Hwang, H. K. Yoo, J. S. Woo, S. Choi, H. Y. Kim, H. J. Jeong, S. Y. Jeong, *et al.*, Scientific reports **4**, 5133 (2014).

[130] W. Qiao, S. Yan, X. He, X. Song, Z. Li, X. Zhang, W. Zhong, and Y. Du, Rsc Advances **4**(92), 50981–50987 (2014).

[131] S. Biccai, S. Barwich, D. Boland, A. Harvey, D. Hanlon, N. McEvoy, and J. N. Coleman, 2D Materials **6**(1), 015008 (2018).

[132] E. Varrla, C. Backes, K. R. Paton, A. Harvey, Z. Gholamvand, J. McCauley, and J. N. Coleman, Chemistry of Materials **27**(3), 1129–1139 (2015).

[133] M. Yi and Z. Shen, Journal of Materials Chemistry A **3**(22), 11700–11715 (2015).

[134] P. Yasaei, B. Kumar, T. Foroozan, C. Wang, M. Asadi, D. Tuschel, J. E. Indacochea, R. F. Klie, and A. Salehi-Khojin, Advanced Materials **27**(11), 1887–1892 (2015).

[135] C. Gibaja, D. Rodriguez-San-Miguel, P. Ares, J. Gómez-Herrero, M. Varela, R. Gillen, J. Maultzsch, F. Hauke, A. Hirsch, G. Abellán, *et al.*, Angewandte Chemie **128**(46), 14557–14561 (2016).

[136] Y. Lin, T. V. Williams, and J. W. Connell, The Journal of Physical Chemistry Letters **1**(1), 277–283 (2010).

[137] E. B. Secor, B. Y. Ahn, T. Z. Gao, J. A. Lewis, and M. C. Hersam, Advanced Materials **27**(42), 6683–6688 (2015).

[138] F. Torrisi and J. N. Coleman, Nature nanotechnology **9**(10), 738–739 (2014).

[139] A.-L. Davesne, S. Lazar, S. Bellayer, S. Qin, J. C. Grunlan, S. Bourbigot, and M. Jimenez, ACS Applied Nano Materials **2**(9), 5450–5459 (2019).

[140] R. Worsley, L. Pimpolari, D. McManus, N. Ge, R. Ionescu, J. A. Wittkopf, A. Alieva, G. Basso, M. Macucci, G. Iannaccone, *et al.*, ACS nano **13**(1), 54–60 (2018).

[141] K. R. Paton and J. N. Coleman, Carbon **107**, 733–738 (2016).

[142] C. Damm, T. J. Nacken, and W. Peukert, Carbon **81**, 284–294 (2015).

[143] Candidate list of substances of very high concern for authorisation.

[144] H. J. Salavagione, J. Sherwood, V. Budarin, G. Ellis, J. Clark, P. Shuttleworth, *et al.*, Green Chemistry **19**(11), 2550–2560 (2017).

[145] Y. Hernandez, M. Lotya, D. Rickard, S. D. Bergin, and J. N. Coleman, Langmuir **26**(5), 3208–3213 (2010).

[146] C. Backes, B. M. Szydłowska, A. Harvey, S. Yuan, V. Vega-Mayoral, B. R. Davies, P.-l. Zhao, D. Hanlon, E. J. Santos, M. I. Katsnelson, *et al.*, Acs Nano **10**(1), 1589–1601 (2016).

[147] A. Griffin, K. Nisi, J. Pepper, A. Harvey, B. M. Szydłowska, J. N. Coleman, and C. Backes, Chemistry of Materials **32**(7), 2852–2862 (2020).

[148] S. Barwich, U. Khan, and J. N. Coleman, The Journal of Physical Chemistry C **117**(37), 19212–19218 (2013).

[149] Y. Hernandez, V. Nicolosi, M. Lotya, F. M. Blighe, Z. Sun, S. De, I. McGovern, B. Holland, M. Byrne, Y. K. Gun'Ko, *et al.*, Nature nanotechnology **3**(9), 563–568 (2008).

[150] J. M. Hughes, D. Aherne, and J. N. Coleman, Journal of applied polymer science **127**(6), 4483–4491 (2013).

[151] K.-Y. Liang and W.-D. Yang, AIP Advances **8**(1), 015018 (2018).

[152] J. Shen, Y. He, J. Wu, C. Gao, K. Keyshar, X. Zhang, Y. Yang, M. Ye, R. Vajtai, J. Lou, and P. M. Ajayan, Nano Letters **15**(8), 5449 (2015).

[153] V. Arunachalam and S. Vasudevan, The Journal of Physical Chemistry C **122**(3), 1881 (2018).

[154] C. Maciel, E. E. Fileti, and R. Rivelino, Chemical Physics Letters **507**, 244 (2011).

[155] A. Govind Rajan, V. Sresht, A. A. Padua, M. S. Strano, and D. Blankschtein, ACS nano **10**, 9145 (2016).

[156] C. A. Howard, H. Thompson, J. C. Wasse, and N. T. Skipper, Journal of the American Chemical Society **126**, 13228 (2004).

[157] T. K. Mukhopadhyay and A. Datta, The Journal of Physical Chemistry C **121**(1), 811 (2017).

[158] T. K. Mukhopadhyay and A. Datta, The Journal of Physical Chemistry C **121**(18), 10210 (2017).

[159] J. Choi, H. Y. Zhang, H. D. Du, and J. H. Choi, ACS Applied Materials & Interfaces **8**, 8864 (2016).

[160] G. Kresse and J. Hafner, Phys. Rev. B **47**, 558 (1993).

[161] G. Kresse and J. Hafner, Phys. Rev. B **49**, 14251 (1994).

[162] G. Kresse and J. Furthmüller, Computational Materials Science **6**(1), 15–50 (1996).

[163] G. Kresse and J. Furthmüller, Phys. Rev. B **54**, 11169–11186 (1996).

[164] T. Thonhauser, V. R. Cooper, S. Li, A. Puzder, P. Hyldgaard, and D. C. Langreth, Phys. Rev. B **76**, 125112 September (2007).

[165] G. Román-Pérez and J. M. Soler, Phys. Rev. Lett. **103**, 096102 August (2009).

[166] A. Becke, The Journal of chemical physics **85**(12), 7184 (1986).

[167] J. Carrasco, W. Liu, A. Michaelides, and A. Tkatchenko, The Journal of Chemical Physics **140**, 084704 (2014).

[168] H. J. Monkhorst and J. D. Pack, Phys. Rev. B **13**, 5188–5192 June (1976).

[169] T. A. Manz and D. S. Sholl, Journal of Chemical Theory and Computation **8**, 2844 (2012).

[170] M. Yu and D. R. Trinkle, The Journal of Chemical Physics **134**(6), 64111 (2011).

[171] W. Tang, E. Sanville, and G. Henkelman, Journal of Physics: Condensed Matter **21**(8), 84204 (2009).

[172] J. Åkesson, O. Sundborg, O. Wahlström, and E. Schröder, Journal of Chemical Physics **137**(17) (2012).

[173] S. Barja, M. Garnica, J. J. Hinarejos, A. L. de Parga, N. Martin, and R. Miranda, Chem. Commun. **46**(43), 8198 (2010).

[174] P. G. Moses, J. J. Mortensen, B. I. Lundqvist, and J. K. Nørskov, Journal of Chemical Physics **130**(10) (2009).

[175] S. P. Ong, W. D. Richards, A. Jain, G. Hautier, M. Kocher, S. Cholia, D. Gunter, V. L. Chevrier, K. A. Persson, and G. Ceder, Computational Materials Science **68**, 314–319 (2013).

[176] Ø. Borck and E. Schröder, Surface Science **664**, 162 (2017).

[177] K. Yoshizawa, T. Kato, and T. Yamabe, The Journal of Chemical Physics **105**(5), 2099–2105 (1996).

[178] S. D. Chakarova-Käck, A. Vojvodic, J. Kleis, P. Hyldgaard, and E. Schröder, New Journal of Physics **12**, 013017 (2010).

[179] S. Lukas, S. Vollmer, G. Witte, and C. Wöll, The Journal of Chemical Physics **114**, 10123 (2001).

[180] Z. Lin, B. R. Carvalho, E. Kahn, R. Lv, R. Rao, H. Terrones, M. A. Pimenta, and M. Terrones, 2D Materials **3**(2), 022002 (2016).

[181] S. M. Davis and J. C. Carver, Applications of Surface Science **20**(1), 193 (1984).

[182] G. Ye, Y. Gong, J. Lin, B. Li, Y. He, S. T. Pantelides, W. Zhou, R. Vajtai, and P. M. Ajayan, Nano Letters **16**(2), 1097 (2016).

[183] S. Roychoudhury, C. Motta, and S. Sanvito, Phys. Rev. B **93**, 045130 (2016).

[184] E. J. Santos, Electric field effects on graphene materials, In *Exotic Properties of Carbon Nanomatter*, 383. Springer (2015).

[185] S. Plimpton, Journal of computational physics **117**(1), 1–19 (1995).

[186] P. Lazar, F. Karlicky, P. Jurecka, M. Kocman, E. Otyepkova, K. Safarova, and M. Otyepka, Journal of the American Chemical Society **135**(16), 6372–6377 (2013).

[187] U. Patil and N. M. Caffrey, The Journal of Chemical Physics **149**(9), 094702 (2018).

[188] A. Cheng and W. Steele, The Journal of chemical physics **92**(6), 3858–3866 (1990).

[189] A. Hardy, J. Dix, C. D. Williams, F. R. Siperstein, P. Carbone, and H. Bock, ACS nano **12**(2), 1043–1049 (2018).

[190] S. Lin, C.-J. Shih, M. S. Strano, and D. Blankschtein, Journal of the American Chemical Society **133**(32), 12810–12823 (2011).

[191] C. Fu and X. Yang, Carbon **55**, 350–360 (2013).

[192] G. Kamath and G. A. Baker, Physical Chemistry Chemical Physics **14**(22), 7929–7933 (2012).

[193] W. L. Jorgensen and J. Tirado-Rives, Proceedings of the National Academy of Sciences **102**(19), 6665–6670 (2005).

[194] L. S. Dodda, J. Z. Vilseck, J. Tirado-Rives, and W. L. Jorgensen, The Journal of Physical Chemistry B **121**(15), 3864–3870 (2017).

[195] L. S. Dodda, I. Cabeza de Vaca, J. Tirado-Rives, and W. L. Jorgensen, Nucleic acids research **45**(W1), W331–W336 (2017).

[196] L. Martínez, R. Andrade, E. G. Birgin, and J. M. Martínez, Journal of computational chemistry **30**(13), 2157–2164 (2009).

[197] S. P. Ong, W. D. Richards, A. Jain, G. Hautier, M. Kocher, S. Cholia, D. Gunter, V. L. Chevrier, K. A. Persson, and G. Ceder, Computational Materials Science **68**, 314–319 (2013).

[198] Ddbst: `http://ddbonline.ddbst.de/DIPPR105DensityCalculation/DIPPR105CalculationCGI.exe?component=Acetone`.

[199] S. Kim, J. Chen, T. Cheng, A. Gindulyte, J. He, S. He, Q. Li, B. A. Shoemaker, P. A. Thiessen, B. Yu, *et al.*, Nucleic acids research **47**(D1), D1102–D1109 (2019).

[200] A. I. Frolov, R. N. Arif, M. Kolar, A. O. Romanova, M. V. Fedorov, and A. G. Rozhin, Chemical science **3**(2), 541–548 (2012).

[201] J. Terrones, P. J. Kiley, and J. A. Elliott, Scientific reports **6**(1), 1–11 (2016).

[202] L. Fumagalli, A. Esfandiar, R. Fabregas, S. Hu, P. Ares, A. Janardanan, Q. Yang, B. Radha, T. Taniguchi, K. Watanabe, *et al.*, Science **360**(6395), 1339–1342 (2018).

[203] A. Sugahara, Y. Ando, S. Kajiyama, K. Yazawa, K. Gotoh, M. Otani, M. Okubo, and A. Yamada, Nature communications **10**(1), 1–7 (2019).

[204] O. Madelung and C. Wohlfarth, *Static Dielectric Constants of Pure Liquids and Binary Liquid Mixtures / Statische Dielektrizitätskonstanten reiner Flüssigkeiten und binärer flüssiger Mischungen*, Landolt-Börnstein: Numerical Data and Functional Relationships in Science and Technology - New Series. Springer Berlin Heidelberg, (1991).

[205] A. Maryott and E. Smith, *Table of Dielectric Constants of Pure Liquids*, Circular of the National Bureau of Standards. U.S. Government Printing Office, (1951).

[206] Properties of solvents used in organic chemistry. `http://murov.info/orgsolvents.htm`.

[207] O. Hammerich and B. Speiser, *Organic Electrochemistry, Fifth Edition: Revised and Expanded*, CRC Press, (2015).

[208] A. J. Oyer, J.-M. Y. Carrillo, C. C. Hire, H. C. Schniepp, A. D. Asandei, A. V. Dobrynin, and D. H. Adamson, Journal of the American Chemical Society **134**(11), 5018–5021 (2012).

[209] C. Backes, K. R. Paton, D. Hanlon, S. Yuan, M. I. Katsnelson, J. Houston, R. J. Smith, D. McCloskey, J. F. Donegan, and J. N. Coleman, Nanoscale **8**(7), 4311–4323 (2016).

[210] S. Wang, C. Wang, and X. Ji, Rsc Advances **7**(82), 52252–52260 (2017).

[211] Z. Baig, O. Mamat, M. Mustapha, A. Mumtaz, K. S. Munir, and M. Sarfraz, Ultrasonics sonochemistry **45**, 133–149 (2018).

[212] T. Abe, Y. Mizutani, N. Kawabata, M. Inaba, and Z. Ogumi, Synthetic metals **125**(2), 249–253 (2001).

[213] M. Dresselhaus and G. Dresselhaus, Advances in Physics **30**(2), 139–326 (1981).

[214] V. Nalimova, M. El Gadi, D. Guerard, P. Lagrange, D. Sklovsky, and C. Hérold, Carbon **33**(2), 153–158 (1995).

[215] M.-C. Kim, E. Sim, and K. Burke, The Journal of Chemical Physics **134**(17), 171103 (2011).

[216] C. Backes, D. Campi, B. M. Szydlowska, K. Synnatschke, E. Ojala, F. Rashvand, A. Harvey, A. Griffin, Z. Sofer, N. Marzari, *et al.*, ACS nano **13**(6), 7050–7061 (2019).

[217] S. Manzeli, D. Ovchinnikov, D. Pasquier, O. V. Yazyev, and A. Kis, Nature Reviews Materials **2**(8), 17033 (2017).

[218] F. Ma, G. Gao, Y. Jiao, Y. Gu, A. Bilic, H. Zhang, Z. Chen, and A. Du, Nanoscale **8**(9), 4969–4975 (2016).

[219] M. Kertesz and R. Hoffmann, Journal of the American Chemical Society **106**(12), 3453–3460 (1984).

[220] X. Chia and M. Pumera, Chemical Society Reviews **47**(15), 5602 (2018).

[221] F. Raffone, C. Ataca, J. C. Grossman, and G. Cicero, The journal of physical chemistry letters **7**(13), 2304–2309 (2016).

[222] S. Kretschmer, H.-P. Komsa, P. Bøggild, and A. V. Krasheninnikov, The Journal of Physical Chemistry Letters **8**(13), 3061–3067 (2017).

[223] M. Pizzochero and O. V. Yazyev, Physical Review B **96**(24), 245402 (2017).

[224] Y.-C. Lin, D. O. Dumcenco, Y.-S. Huang, and K. Suenaga, Nature nanotechnology **9**(5), 391 (2014).

[225] S. Cho, S. Kim, J. H. Kim, J. Zhao, J. Seok, D. H. Keum, J. Baik, D.-H. Choe, K. J. Chang, K. Suenaga, *et al.*, Science **349**(6248), 625–628 (2015).

[226] Y. Kang, S. Najmaei, Z. Liu, Y. Bao, Y. Wang, X. Zhu, N. J. Halas, P. Nordlander, P. M. Ajayan, J. Lou, *et al.*, Advanced Materials **26**(37), 6467–6471 (2014).

[227] Y. Guo, D. Sun, B. Ouyang, A. Raja, J. Song, T. F. Heinz, and L. E. Brus, Nano letters **15**(8), 5081–5088 (2015).

[228] B. Radisavljevic and A. Kis, Nature materials **12**(9), 815 (2013).

[229] Y. Wang, J. Xiao, H. Zhu, Y. Li, Y. Alsaid, K. Y. Fong, Y. Zhou, S. Wang, W. Shi, Y. Wang, *et al.*, Nature **550**(7677), 487 (2017).

[230] M. Acerce, D. Voiry, and M. Chhowalla, Nature nanotechnology **10**(4), 313 (2015).

[231] A. Nourbakhsh, A. Zubair, R. N. Sajjad, A. Tavakkoli KG, W. Chen, S. Fang, X. Ling, J. Kong, M. S. Dresselhaus, E. Kaxiras, *et al.*, Nano letters **16**(12), 7798–7806 (2016).

[232] A. L. Friedman, F. K. Perkins, A. T. Hanbicki, J. C. Culbertson, and P. M. Campbell, Nanoscale **8**(22), 11445–11453 (2016).

[233] J. Luxa, P. Vosecký, V. Mazánek, D. Sedmidubský, M. Pumera, and Z. Sofer, ACS Catalysis **8**(4), 2774–2781 (2018).

[234] S. M. Tan, Z. Sofer, J. Luxa, and M. Pumera, ACS Catalysis **6**(7), 4594–4607 (2016).

[235] Y. Li, K.-A. N. Duerloo, K. Wauson, and E. J. Reed, Nature communications **7**, 10671 (2016).

[236] X. Sun, Z. Wang, Z. Li, and Y. Q. Fu, Scientific reports **6**, 26666 (2016).

[237] G. Gao, Y. Jiao, F. Ma, Y. Jiao, E. Waclawik, and A. Du, The Journal of Physical Chemistry C **119**(23), 13124–13128 (2015).

[238] G. Henkelman and H. Jónsson, The Journal of chemical physics **113**(22), 9978–9985 (2000).

[239] R. Gordon, D. Yang, E. Crozier, D. Jiang, and R. Frindt, Physical Review B **65**(12), 125407 (2002).

[240] J. Heising and M. G. Kanatzidis, Journal of the American Chemical Society **121**(4), 638–643 (1999).

[241] J. Wildervanck and F. Jellinek, Zeitschrift für anorganische und allgemeine Chemie **328**(5-6), 309–318 (1964).

[242] B. Schönfeld, J. Huang, and S. Moss, Acta Crystallographica Section B **39**(4), 404–407 (1983).

[243] K. Bronsema, J. De Boer, and F. Jellinek, Zeitschrift für anorganische und allgemeine Chemie **540**(9-10), 15–17 (1986).

[244] W. Schutte, J. De Boer, and F. Jellinek, Journal of Solid State Chemistry **70**(2), 207–209 (1987).

[245] R. G. Dickinson and L. Pauling, Journal of the American Chemical Society **45**(6), 1466–1471 (1923).

[246] R. E. Bell and R. E. Herfert, Journal of the American Chemical Society **79**(13), 3351–3354 (1957).

[247] N. Podberezskaya, S. Magarill, N. Pervukhina, and S. Borisov, Journal of Structural Chemistry **42**(4), 654–681 (2001).

[248] M. Samadi, N. Sarikhani, M. Zirak, H. Zhang, H.-L. Zhang, and A. Z. Moshfegh, Nanoscale Horizons **3**(2), 90–204 (2018).

[249] A. Kumar and P. Ahluwalia, The European Physical Journal B **85**(6), 186 (2012).

[250] J. Gusakova, X. Wang, L. L. Shiau, A. Krivosheeva, V. Shaposhnikov, V. Borisenko, V. Gusakov, and B. K. Tay, physica status solidi (a) **214**(12), 1700218 (2017).

[251] G.-B. Liu, W.-Y. Shan, Y. Yao, W. Yao, and D. Xiao, Physical Review B **88**(8), 085433 (2013).

[252] Á. M. García, E. del Corro, M. Kalbac, and O. Frank, Physical Chemistry Chemical Physics **19**(20), 13333–13340 (2017).

[253] I. S. Kwon, I. H. Kwak, H. G. Abbas, G. Jung, Y. Lee, J. Park, S. J. Yoo, J.-G. Kim, and H. S. Kang, Nanoscale (2018).

[254] D. Nasr Esfahani, O. Leenaerts, H. Sahin, B. Partoens, and F. Peeters, The Journal of Physical Chemistry C **119**(19), 10602–10609 (2015).

[255] M. Kan, J. Wang, X. Li, S. Zhang, Y. Li, Y. Kawazoe, Q. Sun, and P. Jena, The Journal of Physical Chemistry C **118**(3), 1515–1522 (2014).

[256] F. A. Rasmussen and K. S. Thygesen, The Journal of Physical Chemistry C **119**(23), 13169–13183 (2015).

[257] H. L. Zhuang and R. G. Hennig, The Journal of Physical Chemistry C **117**(40), 20440–20445 (2013).

[258] Y. Liu, V. Wang, M. Xia, and S. Zhang, Journal of Physics: Condensed Matter **29**(9), 095702 (2017).

[259] M. Topsakal and S. Ciraci, Physical Review B **85**(4), 045121 (2012).

[260] M. Topsakal and S. Ciraci, Applied Physics Letters **98**(13), 131908 (2011).

[261] K. M. Bal and E. C. Neyts, Physical Chemistry Chemical Physics **20**(13), 8456–8459 (2018).

[262] T. Brumme, M. Calandra, and F. Mauri, Physical Review B **91**(15), 155436 (2015).

[263] K. Leng, Z. Chen, X. Zhao, W. Tang, B. Tian, C. T. Nai, W. Zhou, and K. P. Loh, ACS nano **10**(10), 9208–9215 (2016).

[264] Q. Li, Z. Yao, J. Wu, S. Mitra, S. Hao, T. S. Sahu, Y. Li, C. Wolverton, and V. P. Dravid, Nano Energy **38**, 342–349 (2017).

[265] C. Papageorgopoulos and W. Jaegermann, Surface science **338**(1-3), 83–93 (1995).

[266] J. Hong, Y. Pan, Z. Hu, D. Lv, C. Jin, W. Ji, J. Yuan, and Z. Zhang, Nano letters **17**(6), 3383–3390 (2017).

[267] A. N. Enyashin and G. Seifert, Computational and Theoretical Chemistry **999**, 13–20 (2012).

[268] Q. Jin, N. Liu, B. Chen, and D. Mei, The Journal of Physical Chemistry C **122**(49), 28215–28224 (2018).

[269] S. R. Morrison, Sensors and actuators **12**(4), 425–440 (1987).

[270] G. Sberveglieri, *Gas sensors: principles, operation and developments*, Springer Science & Business Media, (2012).

[271] W. Yuan and G. Shi, Journal of Materials Chemistry A **1**(35), 10078–10091 (2013).

[272] E. Comini, G. Faglia, G. Sberveglieri, Z. Pan, and Z. L. Wang, Applied Physics Letters **81**(10), 1869–1871 (2002).

[273] G. Darlinski, U. Böttger, R. Waser, H. Klauk, M. Halik, U. Zschieschang, G. Schmid, and C. Dehm, Journal of applied physics **97**(9), 093708 (2005).

[274] V. K. Rai, Applied Physics B **88**(2), 297–303 (2007).

[275] Q. Zhang, Q. Zhou, Z. Lu, Z. Wei, L. Xu, and Y. Gui, Frontiers in chemistry **6**, 364 (2018).

[276] S. Gadipelli and Z. X. Guo, Progress in Materials Science **69**, 1–60 (2015).

[277] I. Shtepliuk, N. M. Caffrey, T. Iakimov, V. Khranovskyy, I. A. Abrikosov, and R. Yakimova, Scientific reports **7**(1), 1–17 (2017).

[278] T. D. Kühne, M. Iannuzzi, M. Del Ben, V. V. Rybkin, P. Seewald, F. Stein, T. Laino, R. Z. Khaliullin, O. Schütt, F. Schiffmann, *et al.*, The Journal of Chemical Physics **152**(19), 194103 (2020).

[279] J. VandeVondele and J. Hutter, The Journal of chemical physics **127**(11), 114105 (2007).

[280] J. Köfinger, G. Hummer, and C. Dellago, Physical Chemistry Chemical Physics **13**(34), 15403–15417 (2011).

[281] A. T. Egger, L. Hörmann, A. Jeindl, M. Scherbela, V. Obersteiner, M. Todorović, P. Rinke, and O. T. Hofmann, Advanced Science **7**(15), 2000992 (2020).

[282] Y. Zhang, A. Lunghi, and S. Sanvito, Acta Materialia **186**, 467–474 (2020).

[283] P. Restuccia, M. Ferrario, and M. C. Righi, Computational Materials Science **173**, 109400 (2020).

[284] A. Genova, D. Ceresoli, and M. Pavanello, The Journal of chemical physics **141**(17), 174101 (2014).